Evolution of intraplate magmatism atop a mantle plume: geochemical and chronological analysis of Shawahit Basalt, Harrat Rahat, Saudi Arabia

P.W. Ball[a,*], G.G. Roberts[b,*], D.F. Mark[c], D.N. Barfod[c], N.J. White[d], B.H. Lodhia[e], M.M. Nahdi[f], S. Garni[f]

[a]*Department of Geosciences, Colorado State University, Fort Collins, CO, USA*
[b]*Department of Earth Science & Engineering, Imperial College London, London, UK*
[c]*NERC Argon Isotope Facility, SUERC, East Kilbride, UK*
[d]*Bullard Laboratories, Department of Earth Science, University of Cambridge, Cambridge, UK*
[e]*School of Minerals and Energy Resources, UNSW Sydney, Australia*
[f]*Saudi Geological Survey, Jeddah, Saudi Arabia*

Abstract

Harrat Rahat is the largest volcanic field in Saudi Arabia and has been active from ~ 10 Ma to the present day. Due to its close proximity to important population centres, Harrat Rahat's recent eruptions, the Medinah lava flows (< 1.7 Ma), have been extensively studied to identify volcanic risk. However, the evolution of Harrat Rahat's most extensive and oldest lava flows, known collectively as the Shawahit Basalt (> 2.5 Ma), is poorly understood. In this study, we collected, dated and geochemically analyzed lava samples from Harrat Rahat, primarily targeting the under-sampled Shawahit unit. We $^{40}Ar/^{39}Ar$ dated 23 Shawahit samples that erupted between 9.4–2.7 Ma. Over the lifetime of Harrat Rahat, we observe a geochemical transition from predominantly tholeiitic to alkalic eruptions coupled with a counter-intuitive decrease in incompatible element concentrations. We attribute these changes to a decrease in melt productivity and a reduction in contamination by enriched lithospheric melts, respectively. Thermobarometric analysis of Harrat Rahat basalts indicates that these lavas were generated by melting of asthenospheric mantle with a potential temperature of $\sim 1456^{+50}_{-32}$ °C beneath lithosphere 50–60 km thick. These results indicate that volcanic activity at Harrat Rahat was initiated by the arrival of a mantle plume beneath lithosphere thinned by a combination of Red-Sea rifting and thermal erosion. Furthermore, we believe that this plume, either acting alone or in combination with a number of other plumes, is responsible for the formation of the Arabian swell, as well as much of the Neogene-recent intraplate volcanic activity observed across western Arabia. Our conclusions are consistent with a wide range of geochemical, seismologic, gravimetric, thermochronologic and geomorphologic observations.

Keywords: Intraplate volcanism, Arabia, Harrat Rahat, Geochemistry, $^{40}Ar/^{39}Ar$ dating

1. Introduction

The Arabian plate formed after the onset of rifting in the Gulf of Aden and Red Sea in Early- and Late-Oligocene times, respectively (see Bosworth, 2015, and references therein). This rifting was proceeded by wide-spread basaltic trap volcanism across Djibouti, Eritrea, northwestern Ethiopia, western Yemen and northeastern Sudan, which initiated at ~ 31 Ma (Hofmann et al., 1997; Rochette et al., 1998). Both rifting and basaltic trap volcanism are commonly attributed to the surfacing of the Afar mantle plume beneath the plate (Schilling, 1973; Marty et al., 1996). Additional pulses of Arabian intraplate volcanic activity occurred at 24–20 and 14–0 Ma (Figure 1a; Camp and Roobol, 1992; Chazot et al., 1998). These recent

*Corresponding author
Email addresses: patrick.ball@colostate.edu (P.W. Ball), gareth.roberts@imperial.ac.uk (G.G. Roberts)

phases manifest as multiple intraplate volcanic provinces that crop out in two main regions along the western edge of the Arabian plate: western Saudi Arabia and Levant. The cause of this volcanism is debated, and opinion falls into two broad camps. First, volcanism was generated by mantle plumes, either via the northwards channelization of Afar plume material parallel to the Red Sea (e.g., Camp and Roobol, 1992; Krienitz et al., 2009; Trifonov et al., 2011; Duncan et al., 2016; Lim et al., 2020), by the presence of smaller plumes or hot mantle blobs beneath western Saudi Arabia and Levant (e.g., Weinstein et al., 2006; Chang and Lee, 2011; Wilson et al., 2014), or by a sheet of upwelling mantle parallel to the Red Sea and connected to the Afar plume (M^{c}Kenzie, 2020). The second camp believes that decompression melting is driven by lithospheric thinning in response to Red-Sea-rift extension (e.g., Lustrino and Sharkov, 2006; Moufti et al., 2012; Sanfilippo et al., 2019). Primary melts may also be generated by melting of asthenospheric mantle (Murcia et al., 2017; M^{c}Kenzie, 2020), by remobilization of fertile material that was trapped within the lithosphere during previous volcanic events (Bertrand et al., 2003; Stein, 2003; Altherr et al., 2019), or by a combination of the two (Shaw et al., 2003; Moufti et al., 2012).

Arabia exhibits broad east-to-west variations in topography and geology. Moving from the Arabian Gulf to the Red Sea, elevation, sedimentary cover and long-wavelength gravity increase, while lithospheric thickness and upper-mantle shear-wave velocities decrease (Divins, 2008; Bruinsma et al., 2014; Lim et al., 2020; Richards et al., 2020). The high elevation region running parallel to the Red Sea is commonly known as the Arabian Swell. The transfer function between gravity and topography (admittance), positive residual-topographic anomalies in the Red Sea and Gulf of Aden, and an absence of internal deformation throughout Arabia suggest that this swell was formed in response to, and is maintained by, sub-crustal processes (Wilson et al., 2014; Hoggard et al., 2017). Calibrated inverse modeling of longitudinal river profiles indicates that much of this high topography formed during the last 20–30 million years (Wilson et al., 2014). The Arabian Swell can be subdivided into three broad domes, each capped by Neogene-to-Quaternary intraplate volcanism (Figure 1a). The affinity between Arabia's recent intraplate magmatism and high topography suggests that processes responsible for the initiation of intraplate volcanism also generated the Arabian Swell.

Harrat Rahat caps the central dome of the Arabian swell and is the most aerially extensive and voluminous volcanic province in Saudi Arabia ($\sim 20,000$ km^3; Camp and Roobol, 1989). It comprises > 900 volcanic vents that stretch for ~ 300 km in a N-S orientation, from the southeastern edge of Al Madinah al Munawwarah to the northeastern outskirts of Jeddah (Figure 1b; Runge et al., 2014). These vents are concentrated into four centers, but lava flows from these centers overlap to form one continuous volcanic province. Typically, lava flows extend for ~ 50 km away from the vents. However, in a few key locations they have exploited incised wadi channels to travel hundreds of kilometers westwards towards the Red Sea.

Harrat Rahat has been active for ~ 10 million years and is commonly subdivided into three stratigraphic units: Shawahit (2.5–10 Ma), Hammah (1.7–2.5 Ma), and Madinah lavas (0–1.7 Ma; Camp and Roobol, 1989). The majority of Madinah lavas, including three historic eruptions in 641, 1256 and 1293 C.E., crop out in the northern region of Harrat Rahat. Given their recent activity and close proximity to Madinah al Munawwarah, the Madinah lavas have been subject to several recent radiometric-dating and geochemical studies (e.g., Moufti et al., 2012, 2013; Murcia et al., 2017; Downs et al., 2018; Stelten et al., 2018; Downs, 2019; Stelten et al., 2020). In contrast, as far as we are aware the Shawahit and Hammah lavas have not been examined since the late 1980's, and have not been analyzed for trace element concentrations using ICP-MS techniques. Moreover, many of the existing geochemical analyses are not linked to accurate geographic locations (Camp and Roobol, 1989, V. Camp, *pers comm.*). The Shawahit and Hammah lavas cover a larger area and were active over a longer period of time than the Madinah lavas. An in-depth analysis of these older lavas is crucial to furthering our understanding of how Harrat Rahat has evolved through time, and therefore to illuminating the mantle and tectonic processes responsible for Arabian-swell formation and generation of intraplate volcanism in Arabia.

In this study, we aim to determine the temporal and geochemical evolution of Harrat Rahat. First, we describe the collection, radiometric dating and geochemical analysis of a suite of samples from the Shawahit

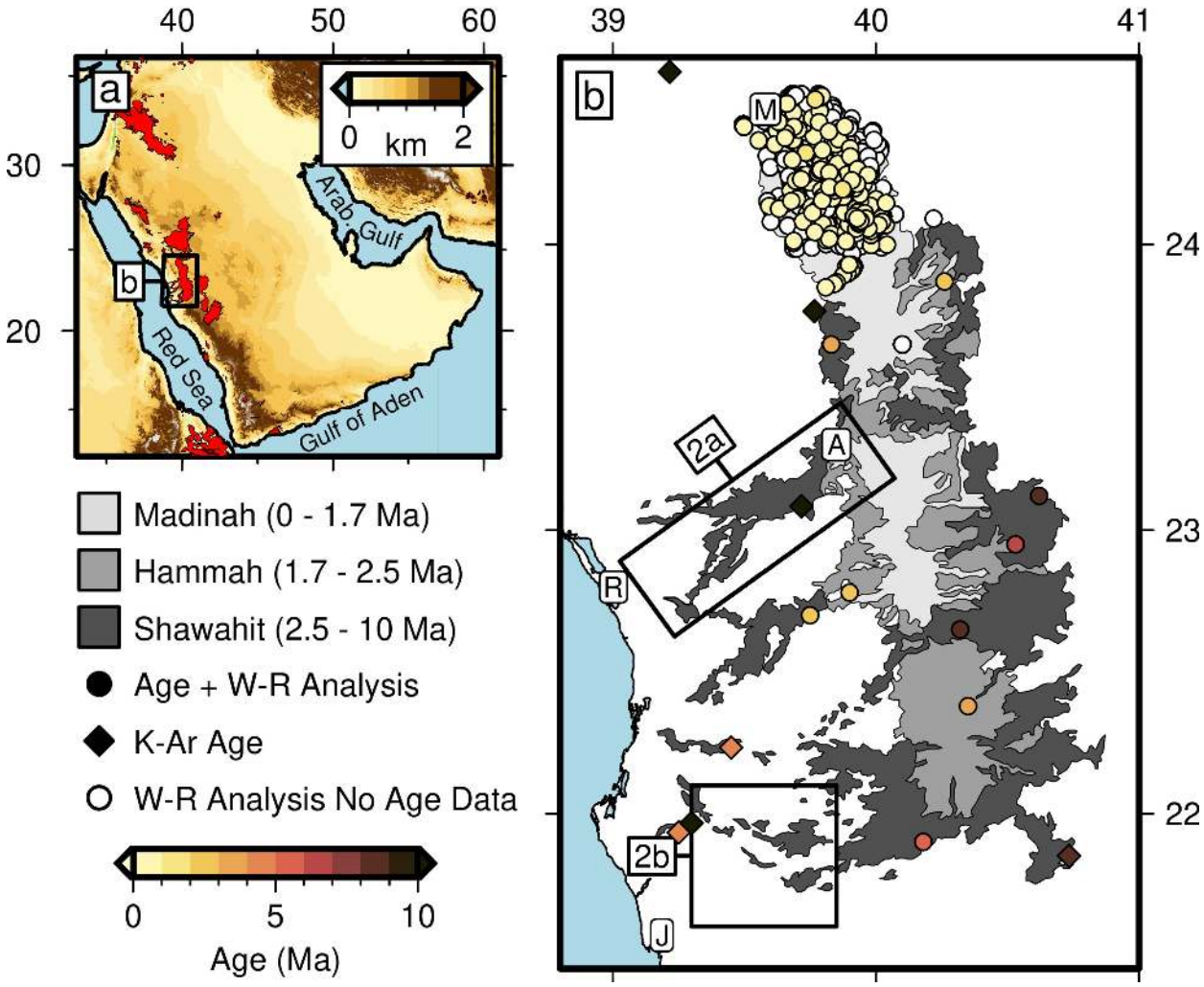

Figure 1: Location and geologic history of Harrat Rahat. (a) Map of Arabian peninsula colored by elevation with red polygons indicating outcrops of Late-Oligocene-to-present-day volcanic rocks. Black box indicates location of map in panel (b). (b) Geologic map of Harrat Rahat. Dark, medium and light gray polygons = outcrops of Shawahit, Hammah and Madinah stratigraphic units (Camp and Roobol, 1989). Symbols = previously published data with color indicating sample age - white samples have not been radiometrically dated. Circles = published whole-rock geochemical analyses (Camp and Roobol, 1989; Moufti et al., 2012; Murcia et al., 2015, 2017; Downs et al., 2018; Stelten et al., 2018; Downs, 2019). Diamonds = K-Ar radiometric dates without whole-rock data (Brown et al., 1989; Camp and Roobol, 1989). Black boxes indicate locations of Figure 2a and 2b. Capital letters show locations of key population centers: A = Al Akhal, J = Jeddah, M = Al Madinah al Munawwarah, R = Rabigh.

and Madinah lavas. Next, these data are combined with published analyses to establish similarities and differences between the whole-rock compositions and geochemical histories of these stratigraphic units. Finally, we use geochemical techniques to calculate the mantle potential temperature beneath Harrat Rahat before developing a conceptual model for its formation, and its relationship to the widespread volcanism and epeirogeny of western Arabia.

2. Sample Collection and Analytical Methods

The majority of samples were collected from Harrat Rahat in March 2015, supplemented by an additional sample collected in January 2015 (A1.1.6; see Table 1). The principal goal of this fieldwork was to obtain

basaltic samples from the Shawahit stratigraphic unit. Samples were primarily collected along the length of Wadi Rabigh between the towns of Rabigh and Al Akhal (Figures 1b and 2a). This wadi incised a series of inter-fingering Shawahit lavas that flowed westwards down the Red Sea escarpment (Figure 3a-b). Samples were taken from the top of this river valley and along one transverse section down to its base (Samples A3.4–A3.6a). For comparison, three Madinah lavas from the upper reaches of Wadi Rabigh and two additional Shawahit basalts from the southwestern edge of Harrat Rahat were also obtained (Figure 2b). Where possible samples were collected from dense sections of the flows, avoiding vesicular and obviously weathered rock (see e.g. Figure 3c-f). In total, 34 samples were collected of which 23 and 17 were $^{40}Ar/^{39}Ar$ dated and analysed for whole-rock composition, respectively. Sample locations are provided in Tables 1 and 2.

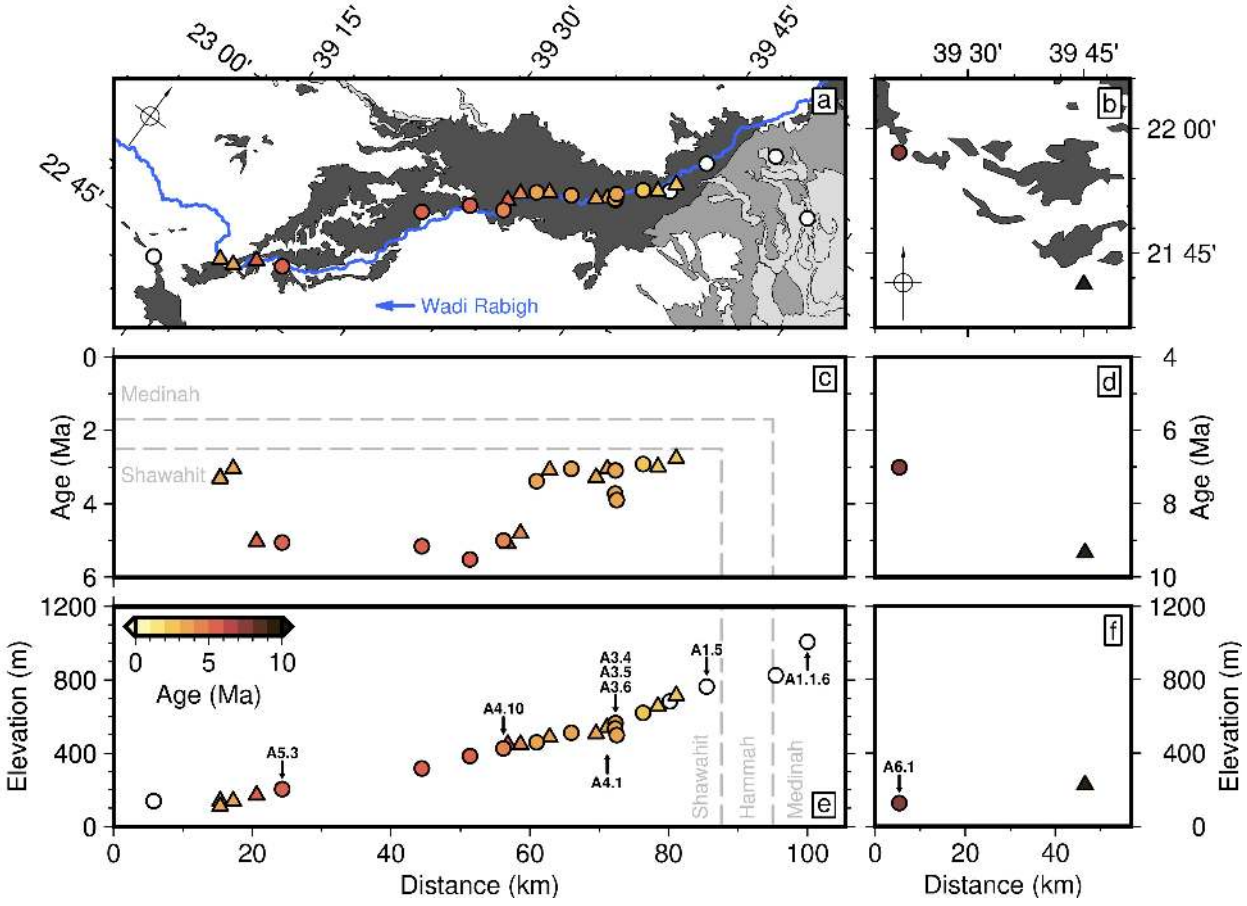

Figure 2: Locations of geochemical and $^{40}Ar/^{39}Ar$ samples. (a) Sample locations along Wadi Rabigh. Dark/light/lightest gray polygons show exposure of Shawahit/Hammah/Medinah stratigraphic units. Blue line = Wadi Rabigh flowing right to left. Colored/white symbols = $^{40}Ar/^{39}Ar$ basalt ages/no age data. Circles/triangles indicate samples with/without accompanying geochemical data. North arrow top left for orientation. Location shown in Figure 1b. (b) Same as Panel (a) for southwest field location. (c) $^{40}Ar/^{39}Ar$ basalt ages as a function of distance (SW–NE), in all cases 2σ uncertainty is within the size of the symbol. Dashed grey lines denote spatial and temporal divisions between stratigraphic units. (d) Same as Panel (c) for southwest field location. (e) Same as Panel (b) but with locality elevation as function of distance. Labels with arrows show samples referred to in main text. (f) Same as Panel (e) for southwest field location.

2.1. $^{40}Ar/^{39}Ar$ Dating

Samples for $^{40}Ar/^{39}Ar$ dating were prepared using the methodologies outlined in Preece et al. (2018). Briefly, samples were crushed, sieved and washed. Groundmass fragments harvested from the 125–250 μm

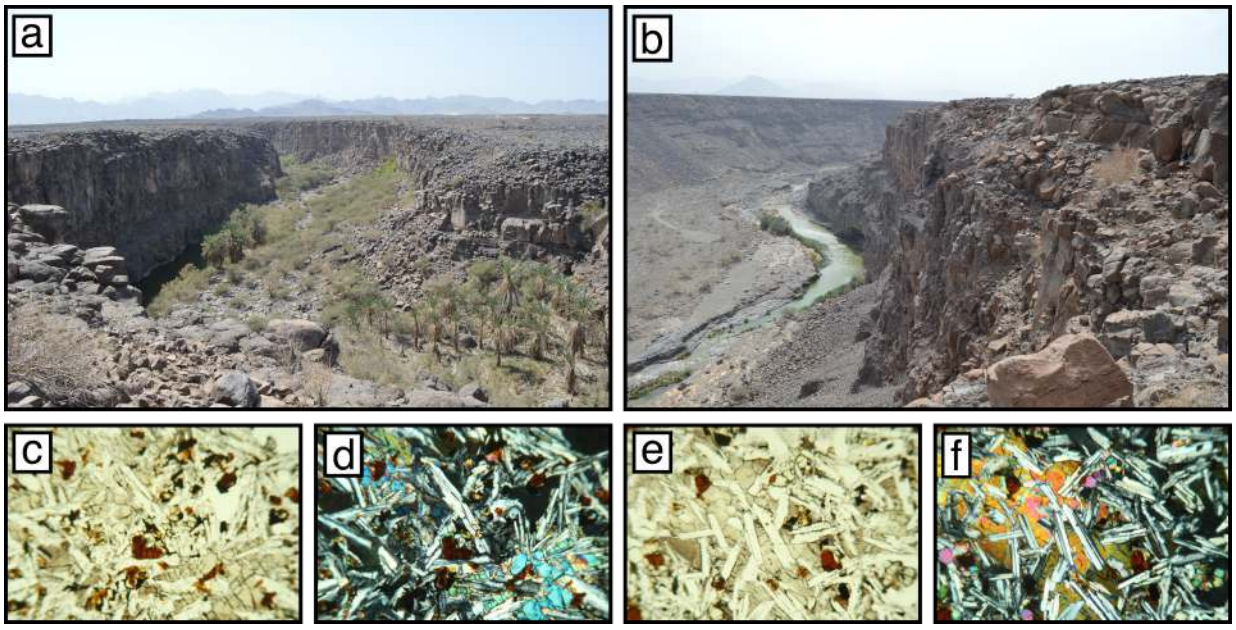

Figure 3: Photographs and thin sections from Harrat Rahat. (a) Photograph looking westward across incised Shawahit basalt flows at locality 1.4: 23.294°N, 39.796°E. Wadi width 400 − 500 m. Peaks in background are Precambrian outcrop. See Figures 1 & 2b. (b) Southeastward view across Shawahit flows from locality 4.1: 23.139°N, 39.691°E. River (water) width ∼ 20 m. (c-d) Plane polarised and crossed polar thin sections of flow at locality 4.10: 23.047°N, 39.582°E; $^{40}Ar/^{39}Ar$ age: 4.55 ± 0.067 Ma. (e-f) Locality 5.3: 22.819°N, 39.376°E; $^{40}Ar/^{39}$ age: 3.08 ± 0.08 Ma.

fraction were selected for dating. This size fraction is too coarse to suffer from recoil during neutron irradiation and was selected to maximise the surface area of the groundmass for acid leaching to promote removal of alteration materials. The samples were subjected to magnetic separation with the non-magnetic fraction leached multiple times in an ultrasonic bath for 300 seconds in 5–9% HNO_3. Each sample underwent multiple leaching steps (typically 4 steps, some samples were subjected to a maximum of 7 leaching steps). Leaching ceased once the samples stopped producing cloudy solutions during sonification. Samples were then cleaned extensively using de-ionised water in an ultrasonic bath. Clean, alteration-free, fragments of groundmass free of olivine, pyroxene, feldspar and other phenocryst/xenocryst phases were hand-picked under a binocular microscope. 150 mg of material was recovered for all samples. Finally, samples were rinsed one more time in ethanol and de-ionised water, prior to packaging for neutron irradiation.

Samples were parcelled in high purity Al-discs for irradiation with international age standard Fish Canyon sanidine (FCs-EK; Morgan et al., 2014) that has an age of 28.294 ± 0.036 Ma (Renne et al., 2011). Each sample was positioned in a single Al-disc. Age standard crystals were positioned adjacent to the samples to permit accurate characterisation of the neutron flux (J parameter) in both a vertical and horizontal orientation. Samples were irradiated for 20 hours in the Cd-lined facility of the CLOCIT Facility at the OSU TRIGA reactor Rutte et al. (2018).

Standards (single crystals) were fused using a CO_2 laser and the lava samples (ca. 50 mg aliquots) were step-heated using a CO_2 laser (Barfod et al., 2014). Extracted gases were subjected to 300 seconds of purification by exposure to two SAES GP50 getters (one maintained at room temperature, the other held at c. 450 °C). A cold finger was maintained at −95.5 °C using a mixture of dry ice ($CO_{2[S]}$) and acetone. Ion beam intensities (i.e., Ar isotope intensities and hence ratios) were measured using a GVI ARGUS V noble gas mass spectrometer in 'true' multicollection mode (Mark et al., 2009). The mass spectrometer system has a measured sensitivity of 7.40×10^{-14} moles/Volt. The extraction and clean-up process, as well as mass spec-

trometer inlet, measurement protocols and data acquisition were automated. Backgrounds (full extraction line and mass spectrometer) were made following every analysis of an unknown. The average background ± standard deviation from the entire run sequence was used to correct raw isotope measurements from unknowns and air pipettes. Mass discrimination was monitored by analysis of air pipette aliquots after every three to four analyses of unknowns.

All Ar isotope data were corrected for backgrounds, mass discrimination, and reactor-produced nuclides and processed using standard data reduction protocols (e.g., Mark et al., 2017) and reported according to the criteria of Schaen et al. (2020). The software Mass Spec was used for data regression and age calculations. The atmospheric argon isotope ratios of Lee et al. (2006), which have been independently verified by Mark et al. (2011), were employed. The ages were calculated using the optimisation model approach of Renne et al. (2010) using the parameters of Renne et al. (2011). $^{40}Ar/^{39}Ar$ ages are reported as X ± Y/Z, where Y is the analytical uncertainty and Z is the full external precision, including uncertainties from the decay constant. All ages are reported at the 2-sigma confidence interval. Owing to the robust uncertainty propagation offered by the optimisation approach (Renne et al., 2010), this is our favoured approach for presentation of data. All data are provided as a Supplementary Dataset to allow for calculation of ages relative to other Ar/Ar calibrations.

All raw Ar/Ar data and isotope correlation plots are presented in Supporting Information. The plateau criteria (Schaen et al., 2020) utilised were (1) consist of at least five or more consecutive steps that comprise at least 50—70% of the ^{39}Ar released; (2) not have a slope (i.e., the majority of consecutive plateau steps do not have ascending or descending ages); and (3) have an isochron regressed through all of the plateau steps with a $(^{40}Ar/^{36}Ar)_{initial}$ that is indistinguishable from the atmospheric $^{40}Ar/^{36}Ar$ (Lee et al., 2006; Mark et al., 2011) value at the 95% confidence level. A summary of results and age spectra for two localities are shown in Tables 1–2 and Figure 4, respectively.

2.2. Geochemical Analysis

Of the 34 samples collected, we selected 14 Shawahit and 3 Medinah lavas for geochemical analysis. We prioritised fresh samples with limited-to-no zeolite or xenoliths. Due to similar selection criteria to those used for radiometric dating, 13 of these Shawahit samples were also radiometrically dated. The whole-rock composition of each sample was calculated using a combination of X-ray Flourescence (XRF) and Laser Ablation – Inductively Coupled Plasma – Mass Spectrometer (LA-ICP-MS) techniques. XRF and ICP-MS analyses were conducted at the universities of Edinburgh and Cambridge, respectively. Our new whole-rock geochemical data is listed in Table 1 and a complete description of both analytical techniques can be found in the Supplementary Materials. Throughout this study, these samples are compared to a compilation of legacy analyses from across the Arabian Peninsula (selected from the global Neogene-Quaternary basaltic intraplate database of Ball et al., 2021). This geochemical database includes, or is augmented by, 1174 previously published samples from Harrat Rahat, of which > 1000 are from the northernmost expression of the Medinah lavas (Camp and Roobol, 1989; Moufti et al., 2012; Murcia et al., 2015, 2017; Downs et al., 2018; Stelten et al., 2018; Downs, 2019).

3. Results

3.1. $^{40}Ar/^{39}Ar$ Dating

Twenty one samples were collected from along a ~ 90 km stretch of Wadi Rabigh (Figure 2a). Two samples (A6.1 & A6.4) were collected from the Shawahit formation $\sim 90 - 150$ km south of Wadi Rabigh. The samples yielded high-quality step-heating spectra that generally satisfy plateau acceptance and statistical criteria. Most samples gave plateaus with 10 or more steps, greater than 80% of the ^{39}Ar release and age uncertainties of better than 2.5%. All samples yielded isochron and plateau ages that are concordant within 2σ.

Seven samples showed non-atmospheric trapped argon compositions, although most are very close to the composition of air. For two samples with low $^{40}Ar/^{36}Ar_{(i)}$ compositions, 4.1 and 4.5, the points on their isochrons are both clustered and distant from the $^{36}Ar/^{40}Ar$ axis making the trapped component intercept less well constrained. Despite this, their isochron and plateau ages are indistinguishable at 2σ. We take the plateau ages as the most robust estimate of emplacement age for the basalts.

The samples collected along Wadi Rabigh have $^{40}Ar/^{39}Ar$ ages between ~ 5.5 and 2.7 Ma, with associated $\pm 2\sigma$ errors of ≤ 0.154 Ma (Figure 2b & Table 2). The uppermost and lowermost reaches of exposed Shawahit lava flows cut by Wadi Rabigh have the youngest ages (< 4 Ma; Figure 4). Three samples within the upper section provide a stratigraphic traverse from the top to the bottom of a wadi canyon, revealing ~ 1 million years of activity contained within ~ 70 m of lava flows (A3.4 – A3.6a). In between the upper and lower reaches, the river incises the eastern fringes, rather than central section, of the Shawahit flows, which were deposited at 5.1 ± 0.4 Ma. The samples collected south of Wadi Rabigh have respective ages of 7.013 ± 0.094 and 9.338 ± 0.1456 Ma (Figure 2b, d).

3.2. Geochemical Analysis

There are demonstrable geochemical differences between the Shawahit, Hammah and Medinah lavas. Shawahit lavas are predominantly tholeiitic basalts that sit within a tight range of SiO_2 and total-alkali values (47–49 wt% and 2.7–3.7 wt%, respectively; Figure 5a). Two new analyses for the Shawahit lavas are alkaline and have $SiO_2 \leq 47$ wt%. These samples, A5.3 and A6.1, are from the southwestern tip of the Wadi Rabigh flows and the southwestern limit of Harrat Rahat, respectively. Their geographic isolation from the rest of the new samples hints at spatial variation in Shawahit composition. There is no discernible temporal variation within the Shawahit lavas, but a clear geochemical transition between these lavas and the younger stratigraphic units is observed. Due to the geochemical similarity between Hammah and Medinah lavas, and the lack of Hammah lava trace-element data, we have decided to discuss these stratigraphic units together. The vast majority of Hammah/Medinah lavas are alkalic and display a wide range of rock types including basalts, trachybasalts, basanites and basaltic trachydacites (Figure 5b,c; Camp and Roobol, 1989; Moufti et al., 2012; Murcia et al., 2017; Downs et al., 2018). Our two new samples from the southern expression of the Madinah lavas are alkali basalts and exhibit similar total-alkali and silica concentrations to those from the northern expression. The spread of rock types found in each of Harrat Rahat's stratigraphic units is a function of fractional crystallisation, extent of melting and source composition. Here, we will discuss each of these processes and their effects on lava composition in turn.

3.2.1. Fractional Crystallisation

The degree of fractional crystallisation within mafic igneous rocks is reflected by their MgO content. Two dominant phases that precipitate from mafic melts, olivine and clinopyroxene, are MgO rich, and so MgO concentrations decrease as crystallisation occurs. Elements partition into different minerals at different rates and plotting element concentrations as a function of MgO content can be instrumental in discerning the extent of fractional crystallisation within a magmatic system. In Figure 6, a suite of major-element concentrations are plotted as a function of MgO content for the Harrat Rahat lavas. Hammah/Medinah lava MgO concentrations vary between $\sim$ 2–11 wt% and, despite considerable scatter for some oxides, we see consistent dramatic changes to major-element trends as a function of MgO concentration (ages < 2.5 Ma; yellow-light orange circles in Figure 6). For instance, at MgO concentrations > 7.5 wt%, Al_2O_3 and Na_2O concentrations increase as MgO concentrations decrease. When MgO concentrations are between $\sim$ 7.5–5 wt%, FeO, Na_2O and TiO_2 concentrations increase, Al_2O and SiO_2 concentrations are approximately constant, and CaO concentrations sharply decrease as MgO concentrations decrease. When MgO concentrations drop below ~ 5 wt%, SiO_2 concentrations begin to rapidly increase, while FeO and TiO_2 concentrations rapidly decrease. In contrast, Shawahit lavas typically have MgO concentrations between $\sim$ 6.5–10.5 wt% and show similar trends in major-element concentrations as a function of MgO to Hammah/Medinah lavas (Figure 6: orange-red circles; $^{40}Ar/^{39}Ar$ ages > 2.5 Ma). For a given MgO content, Shawahit lavas exhibit higher

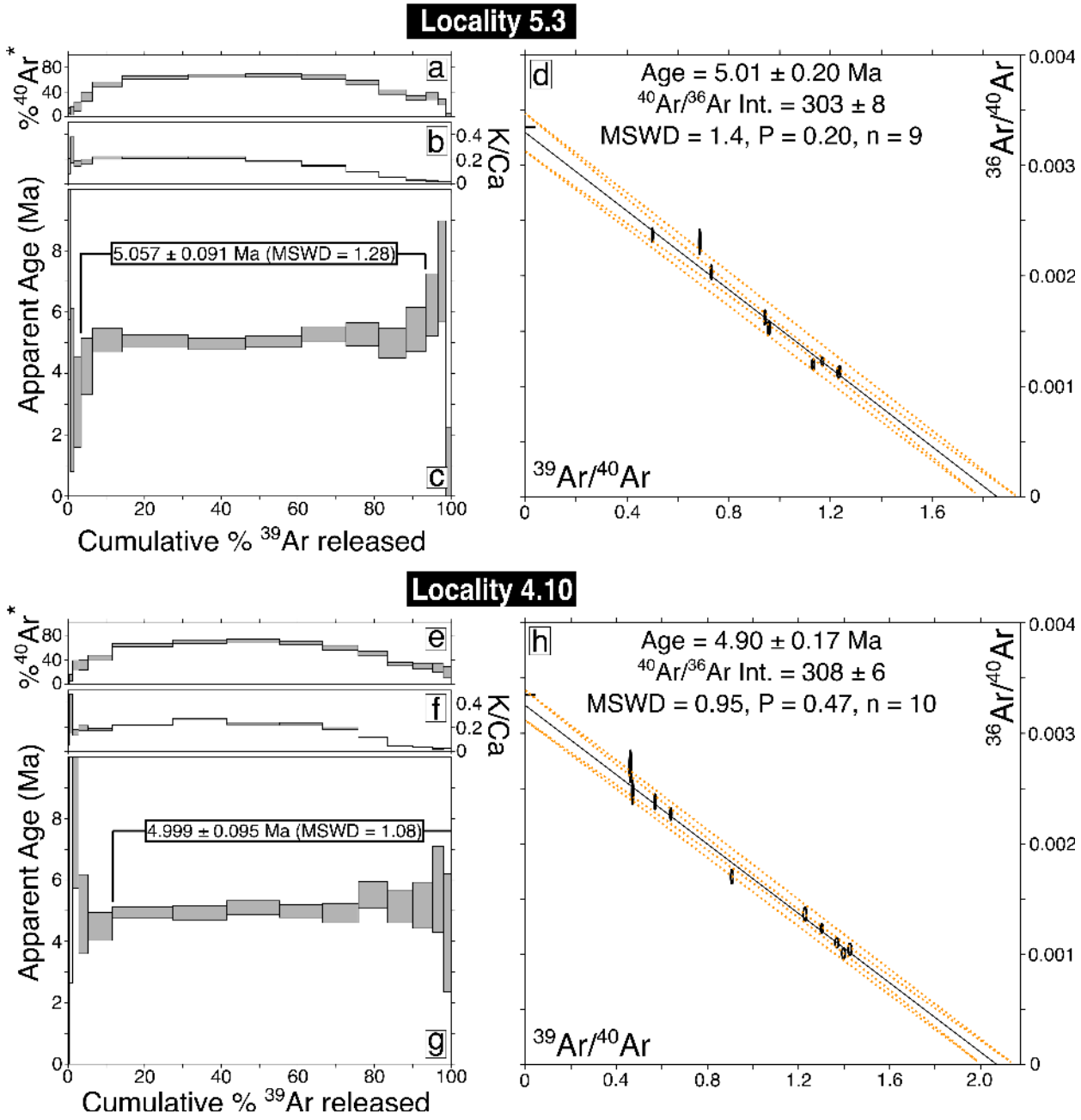

Figure 4: $^{40}Ar/^{39}Ar$ incremental heating analyses of select Harrat Rahat basalts. (a–c) Locality 5.3 (see Figure 2). (d) Isotope correlation plot for all data collected at locality 5.3. MSWD = mean square of weighted deviates. (e–h) Locality 4.10. Spectra and isochron plots for all localities are presented in Supporting Information.

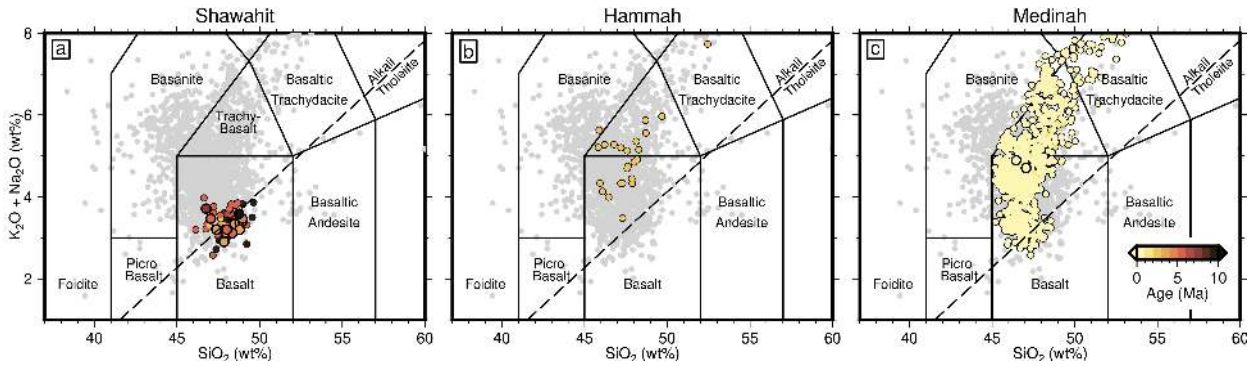

Figure 5: Total alkalis (i.e. K_2O + Na_2O) plotted as function of SiO_2. Sub-division and nomenclature follows standard categorization scheme of Le Maitre (2002). Dashed line = alkali-tholeiite divide redrawn from Irvine and Baragar (1971). Gray circles = data from Arabian peninsula (Ball et al., 2021), large/small circles colored by age = new/published data (Camp and Roobol, 1989; Moufti et al., 2012; Murcia et al., 2015, 2017; Downs et al., 2018; Stelten et al., 2018; Downs, 2019). (a) Shawahit lava samples. (b) Hammah lava samples. (c) Medinah lava samples.

SiO_2, but lower Na_2O and TiO_2, concentrations than Hammah/Medinah lavas. The rate of decrease in both Na_2O and TiO_2 as a function of MgO is also lower in the Shawahit sample suite.

To estimate the presence and proportion of precipitating mineral phases during fractional crystallization, we use rhyolite-Melts-v1.0.2 to calculate melt-evolution pathways for Medinah lavas (yellow circles in Figure 6; ages < 1.7 Ma; Gualda et al., 2012). We assume a starting composition that is an average of all samples with 9 ± 0.5 wt% MgO. These calculations are performed at 1.1 GPa, which corresponds to the base of the crust beneath Harrat Rahat ($\sim$ 35 km; Tang et al., 2016). Temperature is decreased from the initial liquidus to 1000 °C at 5 °C intervals to capture the full fractional-crystallization sequence. We assume that fractional crystallisation occurs in a quartz-fayalite-magnetite (QFM) buffered system. Relative proportions of FeO and Fe_2O_3 in the initial melts at the liquidus have been calculated from FeO^T assuming QFM + 0 (Kress and Carmichael, 1991; Iacovino, 2021). Initial water content of the melt was estimated assuming that $H_2O/Ce = 200$ (Michael, 1995).

Our modelling results indicate that at MgO concentrations > 7.5 wt%, olivine is the only crystallizing phase. The change in major-element trends as a function of MgO wt% that occurs at ~ 7.5 wt% corresponds to the initiation of plagioclase and clinopyroxene precipitation (see e.g., Figure 6b). As the melt evolves, the rate of olivine crystallisation decreases, and the sudden change in SiO_2, FeO and TiO_2 concentrations as a function of MgO wt% that occurs at ~ 5 wt% coincides with the onset of spinel precipitation and an increase in the rate of clinopyroxene crystallization.

Magmas that intrude into the crust can be tapped to fuel multiple eruptions. Successive lavas will be more evolved as the magma source cools, sheds mineral cargo, and assimilates silicious wall-rock material. We note that detailed chronostratigraphic mapping of Medinah lava flows reveals four eruptive sequences between $\sim$ 0.15–0.017 Ma (Stelten et al., 2018). Each sequence lasted $\sim$ 0.009–0.025 Ma and eruptions progressed from alkali basalts, to trachybasalts, and ended with trachytes. Sr-Nd-Pb isotopic data from Medinah-stage samples with a range of MgO concentrations display compositions close to Focal-Zone or Prevalent-Mantle values (Moufti et al., 2012). This consistent isotopic composition suggests that crustal assimilation is limited, and that these whole-rock geochemical trends are driven by fractional crystallisation (Moufti et al., 2012). Similar crystallisation sequences have not been observed within the Shawahit unit. We tentatively suggest that the absence of low-MgO lavas within the Shawahit unit indicates that the plumbing system beneath Harrat Rahat has developed over time. An alternative interpretation is that, because evolved lavas are more viscous and travel shorter distances from eruption centres, low-MgO Sawahit lavas may be buried by younger Hammah and Medinah flows. Shawahit lavas have been mapped at significantly lower

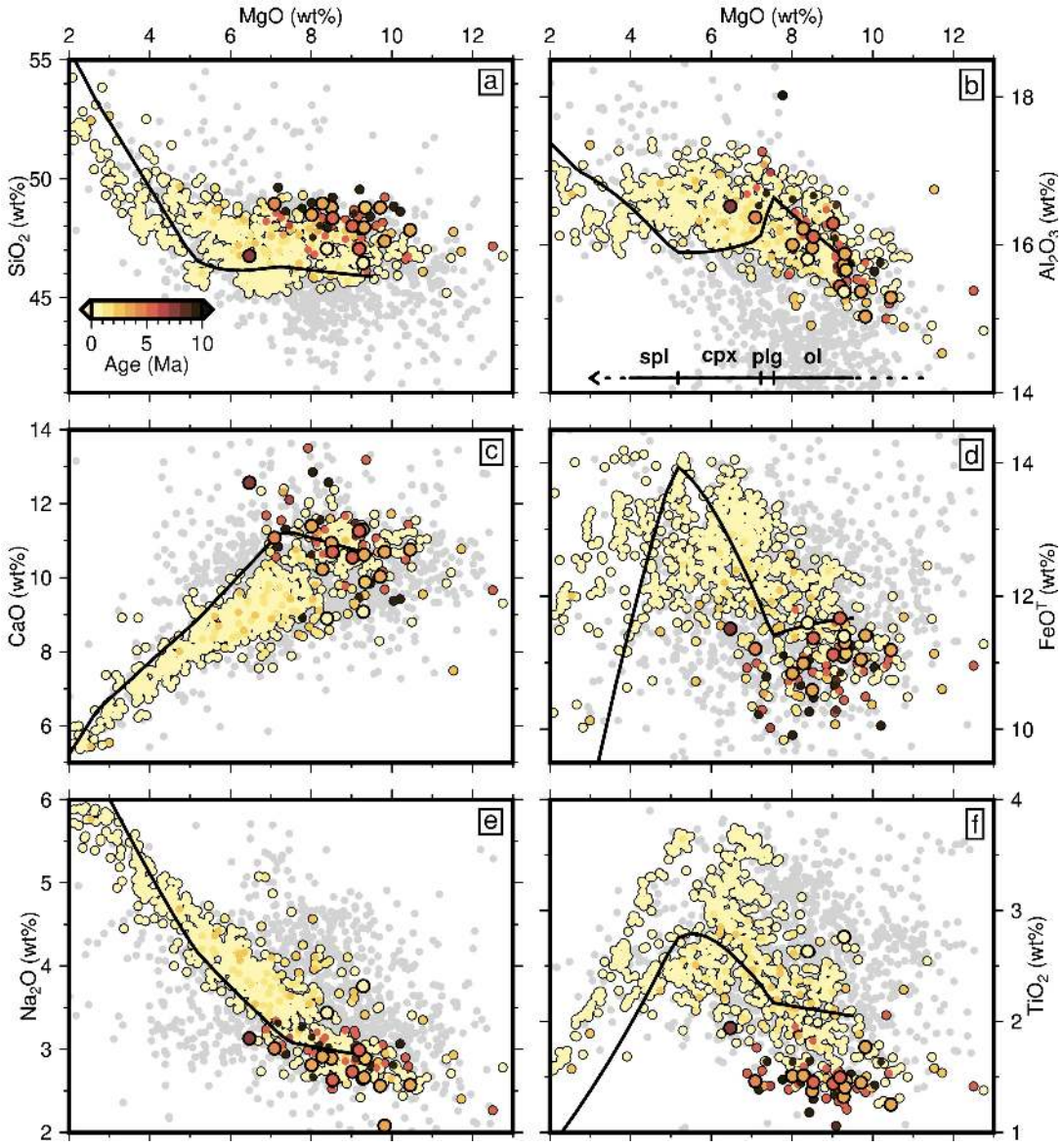

Figure 6: Major-element concentrations of Harrat Rahat lavas. (a) SiO_2 wt% plotted as function of MgO wt%. Large/small circles = new/published data colored by age (Camp and Roobol, 1989; Moufti et al., 2012; Murcia et al., 2015, 2017; Downs et al., 2018; Stelten et al., 2018; Downs, 2019). Grey circles = all-of-Arabia data. Pale yellow circles = Medinah lava samples (< 1.7 Ma); light orange = Hammah lava samples ($1.7 - 2.5$ Ma); orange-red = Shawahit lava samples (> 2.5 Ma). Black line shows fractional-crystallization pathway of melt from average composition of Medinah lavas with 9 ± 0.5 MgO wt%. Model assumes crystallization occurs at 1.1 GPa ($\sim$ 40 km) with QFM = 0. See body text for details. (b) Same for Al_2O_3 wt% as a function of MgO wt%. Line at bottom of panel shows the appearance of each fractionating phase: ol = olivine, plg = plagioclase, cpx = clinopyroxene, spl = spinel. (c)–(e) Same for CaO, FeO, Na_2O and TiO_2 as function of MgO, respectively.

resolution than the younger flows and so evolved Shawahit lavas may be found by future studies.

3.2.2. Melting Conditions

By comparing high-MgO lavas, i.e., lavas with > 8 wt% MgO that have only experienced olivine fractionation, we can nullify the effects of fractional crystallisation and focus on differences generated within the melting region. At MgO contents > 8 wt%, Shawahit lavas have higher SiO_2 and lower FeO^T, Na_2O and

TiO_2 concentrations than the younger Hammah/Medinah lavas (Figure 6). These differences are commonly attributed to depth and degree of melting. Melting at lower pressures generates melts with higher and lower SiO_2 and FeO concentrations, respectively (Kogiso et al., 1998). While the concentrations of TiO_2 and Na_2O in melts decrease as a function of melt fraction (Kogiso et al., 1998). Therefore, these major-element trends indicate that Shawahit lavas formed via asthenospheric decompression melting to shallower depths, producing larger melt fractions at lower pressures, than Hammah/Medinah lavas.

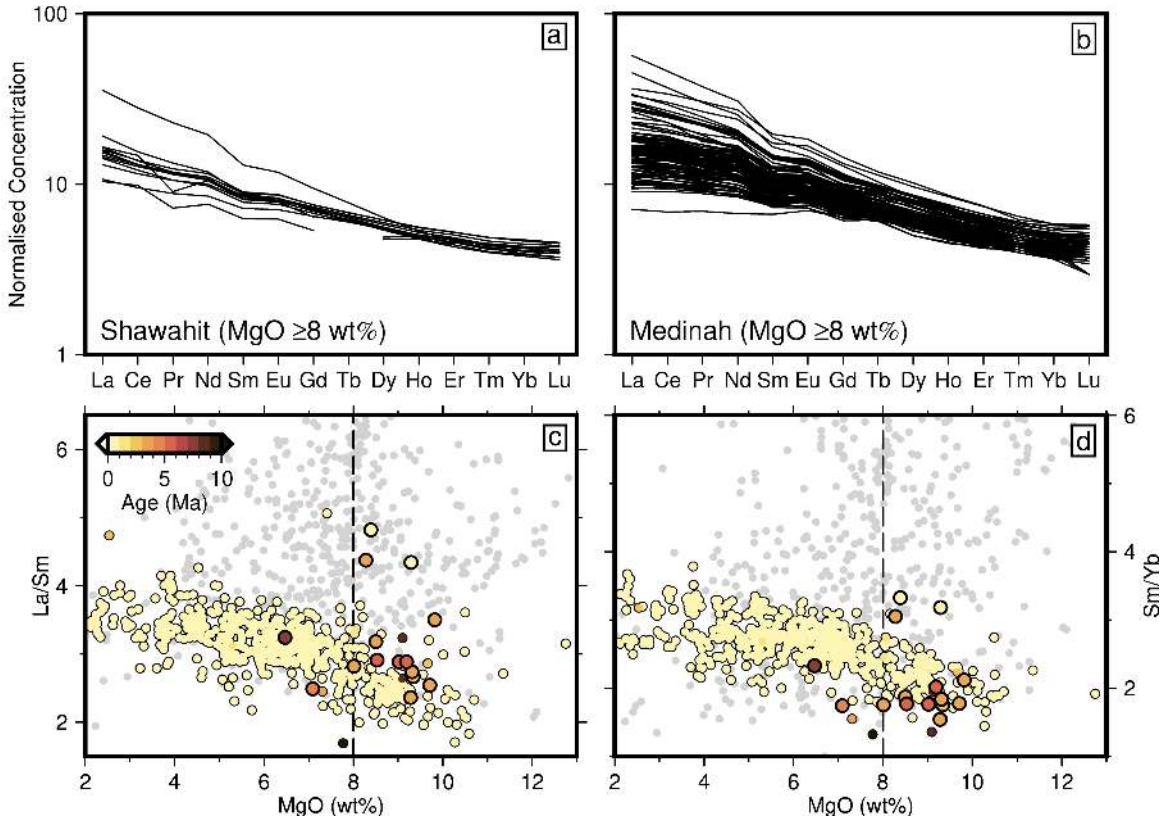

Figure 7: Rare-earth element distributions of Harrat Rahat samples. (a) Shawahit lava (> 2.5 Ma) rare earth elements with MgO ≥ 8 wt% (Camp and Roobol, 1989; Moufti et al., 2012; Murcia et al., 2015, 2017; Downs et al., 2018; Stelten et al., 2018; Downs, 2019). Element concentrations are normalized with respect to primitive mantle (McDonough and Sun, 1995). (b) Same as panel (a) for Medinah lavas (< 1.7 Ma). (c) La/Sm plotted as function of MgO wt%. Large/small circles coloured by age = new/published data from Harrat Rahat; grey circles = all-of-Arabia data. (d) Sm/Yb as a function of MgO wt%.

Light rare-earth element concentrations and La/Sm ratios in melts decrease as a function of melt fraction (Kay and Gast, 1973). Therefore, the melting story at Harrat Rahat implied by major-element trends can be tested and refined using rare-earth element data. Again, we restrict analysis to samples with MgO > 8 wt%. Medinah and Shawahit lavas have indistinguishable La concentrations (average values and standard-deviations of 11.03 ± 4.62 and 10.86 ± 3.74, respectively; Figure 7a-b). In addition, Medinah lavas have slightly lower La/Sm values than Shawahit lavas (2.55 ± 0.45 and 3.02 ± 0.47, respectively; Figure 7c). These trace-element observations imply that Medinah lavas are generated by similar, or perhaps greater, melt fractions than Shawahit lavas. This conclusion somewhat contradicts our major-element observations, since we expect alkalic Medinah lavas to experience lesser extents of melting than tholeiitic Shawahit lavas.

Rare-earth element ratios can also be used to estimate depth of melting. Heavier rare-earth elements, such as Yb, are more compatible within garnet than lighter rare-earth elements, such as Sm (Gast, 1968). As

a result, the Sm/Yb ratio of a melt is likely to increase when melting takes place in the presence of garnet. Since garnet-bearing peridotite is stable at the deepest depths within the melting region (i.e., > 60–70 km), we can use Sm/Yb as a proxy for depth of melting (Jennings and Holland, 2015). In Figure 7d, we show that the Sm/Yb values of Shawahit lavas are generally lower than Medinah lavas with similar MgO contents. Therefore, the proportion of melting at depths > 60–70 km was likely to be higher for the Medinah lavas than for the Shawahit lavas. This conclusion is in agreement with our major-element analysis.

3.2.3. Source Composition

Major-element compositions imply that Shawahit lavas are produced by greater extents of melting at shallower depths than Medinah lavas. In contrast, rare-earth-element concentrations suggest that these stratigraphic units are generated by similar melt fractions. Moreover, the lowest La concentrations and La/Sm ratios, which indicate the largest melt fractions, are found within the Medinah stratigraphic unit (Figure 7). These conflicting major- and trace-element observations can be reconciled if the source composition for Shawahit and Medinah lavas is different. A more enriched source, i.e., one with a higher concentration of a given incompatible element, must melt to a greater extent to generate a melt with the same incompatible-element composition as a depleted source. Here, we use two key ratios to investigate source enrichment: Nb_n/Zr_n and Nb_n/K_n. Subscript n indicates that these elements have been normalised against primitive mantle values and so ratios of 1 are equivalent to a primitive mantle source (McDonough and Sun, 1995).

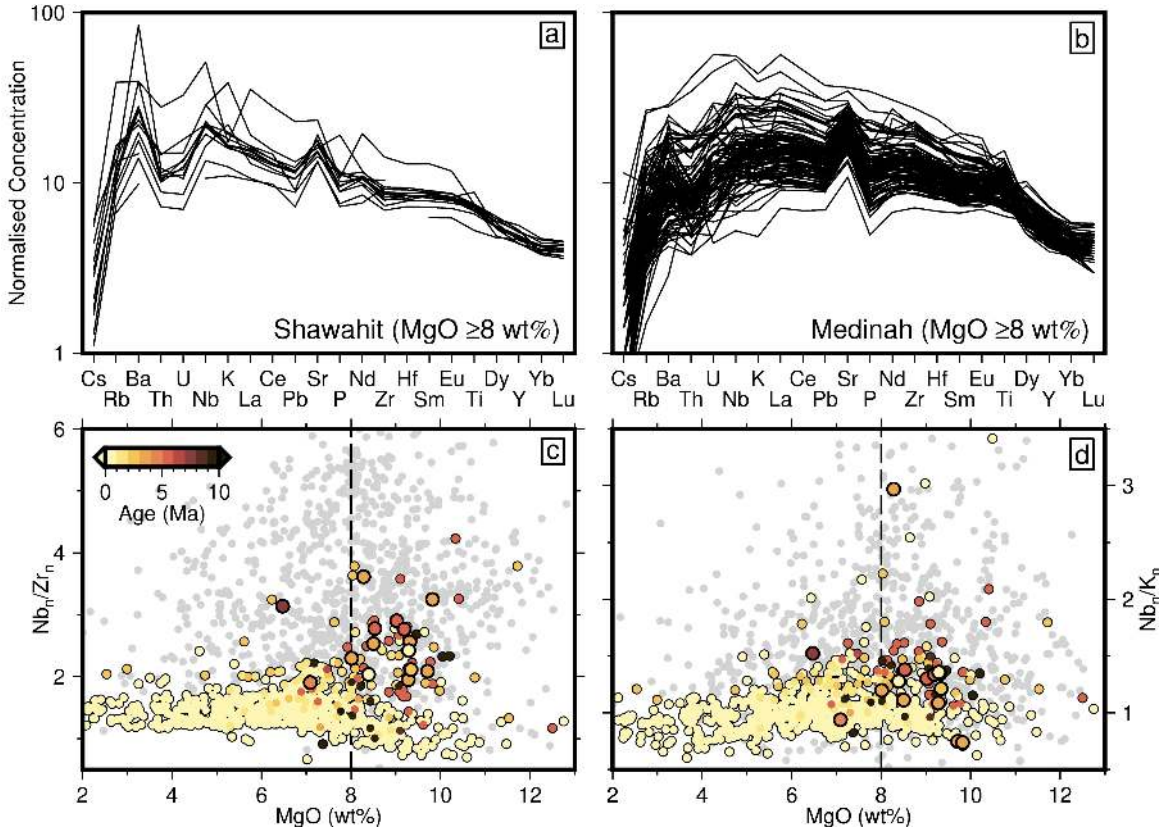

Figure 8: Trace element distributions of Harrat Rahat samples. (a) Shawahit lava trace elements with MgO ≥ 8 wt% (Camp and Roobol, 1989; Moufti et al., 2012; Murcia et al., 2015, 2017; Downs et al., 2018; Stelten et al., 2018; Downs, 2019). Element concentrations are normalized with respect to primitive mantle (McDonough and Sun, 1995). (b) Same as panel (a) for Medinah lavas. (c) Nb_n/Zr_n plotted as function of MgO wt%. Large/small circles coloured by age = new/published data; grey circles = all-of-Arabia data. (d) Nb_n/K_n as a function of MgO wt%.

Nb_n/Zr_n is not significantly affected by variations in melt fraction or fractional crystallization, and so its value in the melt reflects that of its source (Pearce and Norry, 1979). High Nb/Zr ratios can arise from re-entrainment of remnant subducting material with elevated Nb concentrations back into the asthenospheric mantle, or by the annealing of this material onto the base of the over-riding plate (Fitton et al., 1997; Stein et al., 1997). This material is fusible, and so alkali basalts typically have higher Nb_n/Zr_n ratios than tholeiitic basalts (Pearce, 1975). However, at Harrat Rahat we find the opposite relationship (Figure 8c). The predominantly-tholeiitic Shawahit unit has higher Nb_n/Zr_n ratios than the predominantly-alkalic Medinah unit (average values $\pm\sigma$ of 2.23 ± 0.77 and 1.26 ± 0.42, respectively for samples with MgO > 8 wt%).

Since Nb and K have similar partition coefficients during melting of un-metasomatised peridotite, resultant melts will have $Nb_n/K_n \approx 1$. $Nb_n/K_n > 1$ can be generated by fractional crystallization of magma or partial melting of mantle that includes K-rich phases such as amphibole or phlogopite (Varne, 1970; Bergman et al., 1981). These phases can be stabilized by the infiltration of hydrous fluids into the base of the lithosphere. Medinah samples have average Nb_n/K_n values $\pm\sigma$ of 1.05 ± 0.32 and so an un-metasomatised-peridotitic source seems likely. In contrast, Shawahit samples have moderately elevated Nb_n/K_n values of 1.39 ± 0.40 (Figure 8d). Plausible geochemical histories based on these observations are discussed in the following section.

4. Thermal History of Harrat Rahat

A key goal of this study is to determine whether the emplacement of mantle plumes, lithospheric thinning in response to Red Sea rifting, or a combination of the two, is responsible for recent intraplate volcanism in western Arabia. Mantle plumes and lithospheric thinning can generate melting from anomalously-hot and ambient-temperature mantle, respectively. Therefore, estimating mantle temperatures beneath western Arabia is essential to establish the viability of these competing theories. Here, we employ the Plank and Forsyth (2016) major-element thermobarometer to estimate melt-equilibration temperatures and depths beneath Harrat Rahat. We implement this scheme using meltPT, a Python library designed for whole-rock thermobarometric analysis (M^{c}Nab and Ball, 2022). To mitigate the effects of fractional crystallisation, we select samples with MgO > 8.5 wt% and incrementally add olivine that is in equilibrium with each sample until their primary-melt compositions are in equilibrium with the mantle source (Lee et al., 2009). To perform these calculations, we assume that the mantle has a Mg# of 0.9, that 18% of Fe in each sample has 3+ valency, and that the H_2O content of each sample is equal to 200× its Ce concentration (Michael, 1995; Lee et al., 2009; M^{c}Nab et al., 2018). Results from these calculations are shown in Figure 9.

Figure 9a shows that Harrat Rahat melts last equilibrated at 50–80 km depth and at temperatures between ∼ 1380–1460 °C (Figure 9a). Shawahit lavas (> 2.5 Ma) typically equilibrate at depths ≥ 10 km shallower than Medinah (< 1.7 Ma) lavas. Depth-of-equilibration estimates correlate with Sm/Yb, which is often used as a proxy for depth of melting (Figure 9b). The difference in melting depth of Madinah and Shawahit lavas agrees with our earlier major-element analysis (Section 3.2). Since samples that equilibrated at shallower depths also melted to shallower depths, it is likely that these equilibration estimates reflect the limits of decompression melting for each sample. We can therefore employ the methodology of M^{c}Nab et al. (2018) to estimate mantle potential temperature (T_p) beneath Harrat Rahat by fitting decompression-melting paths to our melt equilibration data using meltPT. We find that the data are best fit by melting of anhydrous mantle with a potential temperature of 1456^{+50}_{-32} °C (Figure 9a Katz et al., 2003).

5. Discussion

Harrat Rahat has been active for ∼ 10 Ma and can be subdivided into three stages: Shawahit (∼ 10–2.5 Ma), Hammah (∼ 2.5–1.7) and Medinah (∼ 1.7–0 Ma; Camp and Roobol, 1989). In this study, we collected, radiometrically dated and geochemically analysed a suite of samples from the Shawahit and Medinah stratigraphic units (Figures 1-3). These samples, combined with re-examination of published data, has revealed

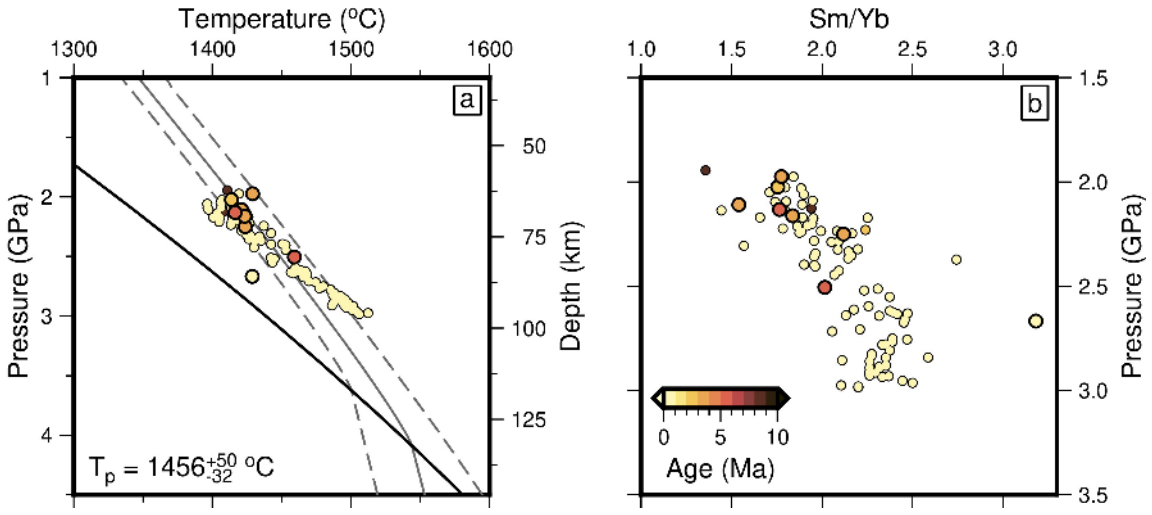

Figure 9: Thermobarometric calculations performed using Plank and Forsyth (2016) thermobarometer within meltPT (M^{c}Nab and Ball, 2022). (a) Temperature plotted as function of pressure or depth. Circles = equilibration pressure and temperature estimates determined for mafic samples from Harrat Rahat using formulation of Plank and Forsyth (2016) where SiO_2 >40 wt%, MgO> 8.5 wt%, $Fe^{3+}/\Sigma Fe = 0.18$ and $H_2O/Ce = 200$. Large/small circles are colored by age and indicate calculations for new/published samples. Black line = anhydrous solidus; gray line = best-fitting melt pathway; dashed gray lines = minimum and maximum melt pathways for which misfit value at global minimum is double (Katz et al., 2003). Best-fitting melt pathway determined using method of M^{c}Nab et al. (2018); optimal value of potential temperature = 1456^{+50}_{-32} °C. (b) Sm/Yb ratios plotted as function of calculated pressures.

three key geochemical differences between lavas erupted before and after ~ 2.5 Ma. First, tholeiitic basaltic eruptions during the Shawahit stage are replaced by alkalic basaltic eruptions in the Hammah and Medinah stages (Figure 5). Second, the younger Hammah/Medinah lavas include multiple low-MgO eruptions, which are not observed in older Shawahit flows (Figure 6). Third, the Shawahit lavas are generated from a source with elevated Nb_n/Zr_n and Nb_n/K_n ratios, and light rare-earth element concentrations (Figure 7). Thermobarometric analysis of Harrat Rahat lavas reveals that they were generated by a mantle plume with excess temperatures of $\sim 125 \pm 75$ °C beneath lithosphere ~ 50 km thick (Figure 9). It is clear that mantle conditions and the magmatic plumbing system beneath Harrat Rahat have evolved through time. Here, we discuss the chemical transitions observed at Harrat Rahat, possible mechanisms to explain its formation, and place its evolution into a pan-Arabian context.

5.1. Geochemical Evolution of Harrat Rahat

It has long been recognised that alkali basalts are generated by less-extensive melting at deeper depths than tholeiitic basalts (Green and Ringwood, 1966; Gast, 1968). This relationship with depth is confirmed by our thermobarometric-modeling results and trace-element observations. The majority of Shawahit and Medinah basalts equilibrate at depths < 60 km and > 60 km, respectively (Figure 9a). Moreover, our calculated equilibration depths negatively correlate with Sm/Yb values, which are sensitive to depth of melting (Figure 9b). These results imply that the lithosphere beneath Harrat Rahat may be rethickening, which is tending to prevent decompression melting at depths < 60 km in younger samples.

Incompatible-element concentrations (e.g., La and La/Sm) are expected to decrease as a function of melt fraction (Kay and Gast, 1973). An unusual characteristic of Harrat Rahat lavas is that some alkalic (low melt fraction) Medinah basalts have lower incompatible-element concentrations than tholeiitic (high melt fraction) Shawahit basalts (Figure 7). To account for this discrepancy, we believe that Shawahit and Medinah lavas are generated from different sources. This inference is supported by observed differences in Nb_n/Zr_n and Nb_n/K_n, which are unaffected by melting or fractional crystallization processes (Figure 8).

Melts from previous magmatic events can become frozen within, or metasomatize surrounding, lithospheric mantle (Figure 10b; Foley, 1992). Metasomatized veins often contain high concentrations of incompatible elements, including enough water to stabilize hydrous phases such as amphibole (Foley, 1992). Amphiboles in intraplate lithosphere can have high Nb/Zr ratios and partial melting of metasomatic veins containing amphibole can generate fluids with high Nb/K ratios (Späth et al., 2001; Coltorti et al., 2007). These veins are fusible and are easily mobilized by subsequent magmatic events (Foley, 1992). Asthenospheric melts can be contaminated by these lithospheric melts during ascent, increasing their incompatible-element concentrations, Nb_n/Zr_n ratios and Nb_n/K_n ratios. Multiple subduction and melting events have metasomatized parts of Arabia's lithospheric mantle (Henjes-Kunst et al., 1990; Stein et al., 1997; Kaliwoda et al., 2007; Shaw et al., 2007; Nasir and Rollinson, 2009; Buikin et al., 2010). We believe that the initiation of magmatism at Harrat Rahat may have remobilized metasomatic veins within the Arabian lithosphere. We suggest that observed compositions of Shawahit lavas, including anomalously high incompatible-element concentrations, were generated by mixing of primary asthenospheric melts with small proportions of enriched lithospheric melts (Figure 10b). Overtime, these veins became depleted and could no longer contribute to the composition of melts during the Hammah and Medinah volcanic phases (Figure 10c). Similar lithospheric components have been identified at multiple intraplate volcanic provinces in western Arabia (e.g., Bertrand et al., 2003; Stein, 2003; Shaw et al., 2003; Moufti et al., 2012; Altherr et al., 2019).

Volcanic eruptions of material more-evolved than basalt only occur at Harrat Rahat during and after the Hammah phase (< 2.5 Ma; Figure 6). The absence of evolved eruptions during the Shawahit phase indicates consistent rapid ascent from the melting region to the surface (Figure 10b). This simple system appears to have been replaced at ~ 2.5 Ma by a complex magmatic plumbing system, resulting in eruptions with a wide variety of compositions (Camp and Roobol, 1989).

5.2. Causes of Volcanism at Harrat Rahat

Our potential-temperature estimate for the upper mantle beneath Harrat Rahat of 1456^{+50}_{-32} °C is within error of numerous previous estimates. As part of a global study, Ball et al. (2021) applied rare-earth-element inverse modeling and tomographic techniques to estimate mantle potential temperatures (T_p) beneath Harrat Rahat of 1409^{+30}_{-24} °C and 1550 °C, respectively. These results agree with temperatures estimated beneath Harrat Khaybar using a similar rare-earth-element modeling approach (1391 °C; Figure 10a; M^{c}Kenzie, 2020).

When these major-element, rare-earth-element and tomographic techniques are applied to global databases of mid-oceanic-ridge segments, they yield average T_p of 1404 °C, 1312 °C and 1333 °C, respectively (Richards et al., 2020; Ball et al., 2021; M^{c}Nab and Ball, in review). Assuming that the global mid-oceanic-ridge network represents average mantle potential temperatures, the mantle beneath Harrat Rahat is predicted to be $\sim$ 50–200 °C hotter than ambient mantle, with our new estimate representing the lower bound. Furthermore, rare-earth-element and tomographic modeling studies predict that the lithosphere beneath Harrat Rahat is ~ 50 km thick, in agreement with the shallowest equilibration depths presented here (Figure 9a; M^{c}Kenzie, 2020; Ball et al., 2021). These mantle-temperature and lithospheric-thickness estimates are corroborated by numerous receiver-function and seismic tomographic studies which conclude that western Arabia consists of asthenosphere with excess temperatures of $\sim$ 200–330 °C capped by lithosphere < 100 km thick (Hansen et al., 2007; Park et al., 2008; Yao et al., 2017; Tang et al., 2019; Lim et al., 2020; M^{c}Kenzie, 2020). Therefore, it is likely that Harrat Rahat lavas were generated by decompression melting of anomalously hot mantle beneath lithosphere ~ 50 km thick.

Several observations suggest that elevated temperatures beneath Harrat Rahat are derived from mantle plumes. Since ^{3}He is incompatible during melting and cannot be generated within the mantle, the ^{3}He/^{4}He ratio of a melt is low if the mantle source has a history of partial melting (Craig and Lupton, 1981). Therefore, high ^{3}He/^{4}He$\times 10^4$ ratios in eastern Africa, i.e., $> 8 \pm 1$, are though to represent melting of deep undepleted primordial mantle material that has been entrained within a mantle plume (Pik et al., 2006; Halldõrsson et al., 2014). A recent study observed plume-like ^{3}He/^{4}He$\times 10^4$ ratios within Harrat Rahat

olivines (9.3–11.8; Murcia et al., 2013, 2017). These values match those generated along the Red Sea rift at the same latitude (9.5–11; Moreira et al., 1996). Although multiple volcanic provinces close to Harrat Rahat, including Harrats Hutaymah and Al Kishb, record low $^3He/^4He\times10^4$ values that do not require the involvement of primordial material (5.8–8.3; Konrad et al., 2016). Overall, $^3He/^4He\times10^4$ values decrease northwards as a function of distance away from Afar, and are indistinguishable from background upper mantle beneath the northern Red Sea and Harrat As Shaam (Moreira et al., 1996; Marty and Zimmermann, 1999). This trend, and the N-S orientation of Harrats Rahat, Khaybar and Ithnayan, has led some authors to suggest that western-Arabian volcanism is fuelled by the northwards channelization of hot mantle spreading out from a mantle plume centred beneath Afar (Figure 10b,c Camp and Roobol, 1992; Krienitz et al., 2009; Trifonov et al., 2011; Duncan et al., 2016; Lim et al., 2020).

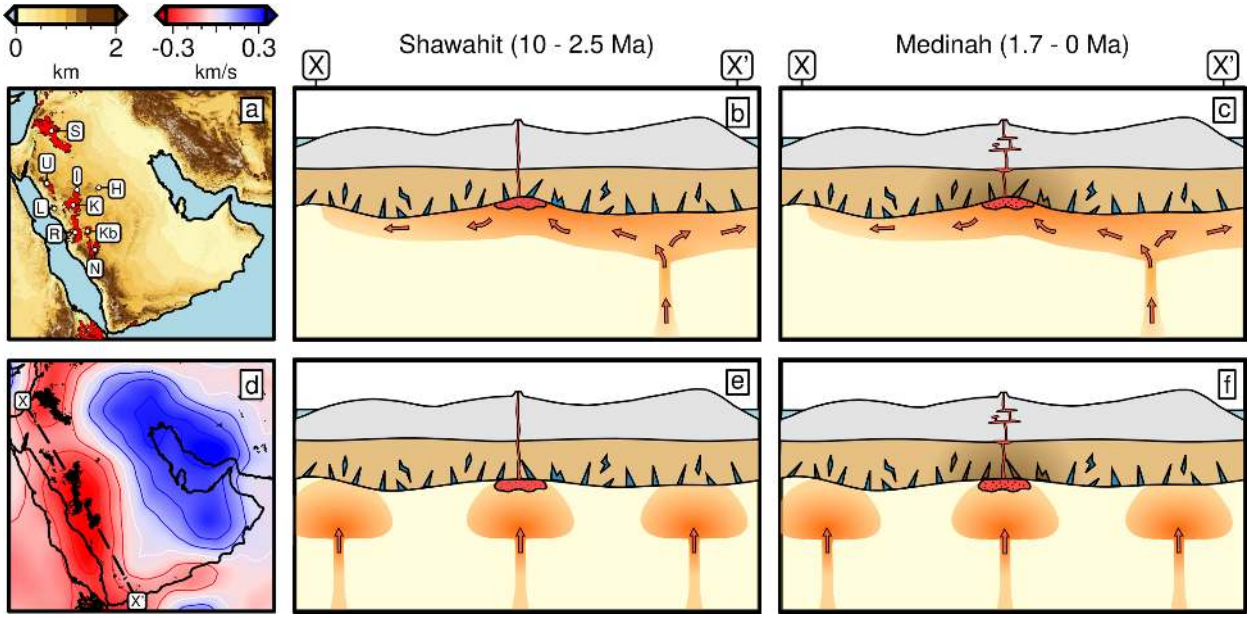

Figure 10: Crust and upper mantle evolution beneath Harrat Rahat and its surroundings. (a) Elevation map of Arabia. Red polygons = Neogene-Recent volcanic provinces: H = Hutaymah, I = Ithnayan, K = Khaybar, Kb = Al Kishb, L = Lunayyir, N = Nawasif, R = Rahat, S = As Shaam, U = Uwayrid. (b) Cartoon showing generation of Shawahit lavas; grey/brown polygons = crust/lithosphere; blue areas = metasomatized lithosphere; orange/yellow polygons = hot/ambient mantle; red polygon = melt; arrows show mantle flow (e.g. from Afar). (c) Same as panel (b) but for the younger Medinah lavas; dark brown area of lithosphere has been depleted in metasomatized material. (d) Map of Arabia colored by ΔV_s at 150 km depth, red/white/blue contours = +0.15/0/−0.15 km/s (Schaeffer and Lebedev, 2013). Dashed line indicates transect depicted in panels (b–c) and (e–f). Black = Neogene-Recent volcanic provinces. (e–f) Sample as panels (b–c) but showing possibility of multiple plumes beneath Arabia.

Evidence for the northwards channelization of the Afar mantle plume is also evident in seismic-tomographic models. Shear-wave velocities decrease as a function of temperature. Global shear-wave velocity models show a plume conduit rising from the deep mantle, anomalously slow velocities in the upper mantle beneath Afar, and extending northwards beneath Harrat Rahat (Figure 10d; Schaeffer and Lebedev, 2013; French and Romanowicz, 2015). These findings are corroborated by local studies that show a narrow N-S trending low-velocity zone in the upper mantle and shear-wave splitting measurements with N-S-trending fast axes (Hansen et al., 2006; Lim et al., 2020).

As plume material spreads out beneath the plate it will cool as a function of distance away from the centre (see e.g. Rudge et al., 2008). Moreover, each time melting occurs, the plume channel will cool down, become more refractory, less dense, and its $^3He/^4He\times10^4$ value will decrease. To generate large melt fractions via decompression melting beneath western Arabia, the lithosphere here must be thinner than other

areas that this material previously passed through, such as the East-African rift and the Red Sea (Figure 10b, c; Lim et al., 2020). Alternatively, small-scale convective processes associated with eastern Arabia's thick lithosphere may lift undepleted material, that has travelled towards the base of the channel to the top, so that it decompresses and melts as it passes beneath western Arabia.

Harrats Rahat (∼ 23°N, 40°E), Khaybar (∼ 25.5°N, 40°E) and Ithnayan (∼ 26.5°N, 40.2°E) collectively exhibit south-to-north age-progressive volcanic activity, initiating at 10, 5 and 3 Ma, respectively (Figure 10a; Camp and Roobol, 1992). A lack of age progressive volcanism elsewhere on the peninsula challenges the notion of magmatism generated as a consequence of flow along an asthenospheric channel away from Afar. An alternative hypothesis is that intraplate volcanism in Afar/Yemen, western Arabia, and the Levant are fuelled by separate mantle plumes (Figure 10e–f; Weinstein et al., 2006; Chang and Lee, 2011; Wilson et al., 2014). This scenario does not require any age progression and can generate the three topographic domes that these volcanic regions cap (Wilson et al., 2014). It may also adequately explain $^{3}He/^{4}He$ variations if each plume contains a different proportion of primordial material. However, it is difficult to reconcile this three-plume set-up with N-S orientated shear-wave splitting measurements, unless these measurements are generated by plate motion rather than asthenospheric flow (Hansen et al., 2006). It is beyond the scope of this paper to determine whether these volcanic provinces are generated by one plume or three. Nonetheless, thermobarometric estimates, rare-earth-element inverse modeling, $^{3}He/^{4}He$ data and seismic tomographic images indicate the presence of a mantle plume beneath Harrat Rahat, and that Arabian volcanism and the Arabian swell cannot be generated by lithospheric thinning alone, as some authors have suggested (Lustrino and Sharkov, 2006; Moufti et al., 2012; Sanfilippo et al., 2019).

Although we do not believe melting at Harrat Rahat is generated by lithospheric thinning alone, it is clear that it has occurred and does contribute to melting. The presence of thin lithosphere beneath western Arabia is revealed by seismic imaging and ratified by our whole-rock thermobarometric analysis (Figure 9; Hansen et al., 2007; Park et al., 2008; Yao et al., 2017; Tang et al., 2019; Lim et al., 2020; M^{c}Kenzie, 2020). Furthermore, xenoliths found within Neogene-recent lava flows across Arabia equilibrated at temperatures of 877–1227 °C and at pressures of 0.9–2.0 GPa (McGuire, 1988; Medaris and Syada, 1999; Kaliwoda et al., 2007; Ahmed et al., 2016). Crucially, these high temperatures at shallow depths have not yet translated into high surface heat flow (Gettings et al., 1986; McGuire, 1988). Since the lithosphere has not yet thermally re-equilibrated, lithospheric thinning must have occurred $<$ 40–60 Ma (Wilson et al., 2014). Much of this lithospheric thinning is probably generated by rifting and the formation of the Red Sea (Bosworth, 2015). However, the arrival of a mantle plume or plumes beneath the plate may have further thinned the lithosphere, particularly in volcanic regions located far from the Red Sea (Davies, 1994).

5.3. Epeirogeny of western Arabia

Harrat Rahat caps the central dome of the Arabian swell (Figure 1a). Admittance analysis and the arguments presented above demonstrate that both the swell and this accompanying intraplate volcanism are generated by a combination of lithospheric thinning and the presence of a mantle plume (Wilson et al., 2014). In three locations, including our primary field area along the length of Wadi Rabigh, Shawahit lavas have breached the Red Sea escarpment and flowed downhill towards the Red Sea. This morphology indicates that a significant proportion of swell formation occurred prior to the earliest eruptions at Harrat Rahat (∼ 10 Ma; Camp and Roobol, 1989). This conclusion is corroborated by thermochronometric data from across the swell, which require rapid cooling after ∼ 25 Ma, which can be linked to the onset of uplift and exhumation (Bohannon et al., 1989; Menzies et al., 1997; Pik et al., 2013). In addition, inverse modeling of river profiles reveals that uplift rate in the area surrounding Wadi Rabigh rapidly increased at ∼ 20 Ma, and this rate slowly decreased towards the present day (Wilson et al., 2014). These constraints indicate that the swell began to form in conjunction with the opening of the Red Sea, ∼ 10 Ma before the first eruptions at Harrat Rahat. Uplift, without significant crustal thickening, requires either surface denudation, additional lithospheric thinning or increased asthenospheric temperatures to occur. Therefore, a gradual decay of uplift rates from a maximum at ∼ 20 Ma is in agreement with our geochemical modelling results,

as we predict constant asthenospheric temperatures and $\sim$ 10 km of lithospheric thickening since the onset of Harrat Rahat volcanism.

6. Conclusion

Harrat Rahat is the largest Neogene-to-Quaternary volcanic province in Saudi Arabia and is responsible for numerous historic eruptions near Al Madinah al Munawwarah. Harrat Rahat can be subdivided into three stratigraphic units: Shawahit, Hammah and Medinah that were active between 10–2.5, 2.5–1.7, and 1.7–0 Ma, respectively. In this study, we collected, radiometrically dated, and geochemically analysed a suite of Shawahit basalts from along the length of Wadi Rabigh. These samples were augmented by data from 3 newly-collected Medinah lavas and a comprehensive database of legacy samples. Shawahit tholeiitic basalts were generated by a mantle plume with excess temperatures of 125 ± 75 °C beneath lithosphere thinned by Red Sea rifting and/or thermal erosion. During their ascent to the surface, Shawahit melts were contaminated by incompatible-element-rich lithospheric melts. These lithospheric metasomatic veins were gradually depleted and did not contribute to later eruptive phases. Moreover, the predominantly-alkalic younger Hammah and Medinah lavas may have formed at deeper depths beneath a gradually re-thickening lithosphere, and a complex magmatic pluming system developed so that Hammah and Medinah melts were often subject to greater degrees of fractional crystallisation during ascent.

7. Data Availability Statement

All new $^{40}Ar/^{39}Ar$ and whole-rock geochemical analyses are presented in Tables within the main text of this article. Analysis of associated standards, additional information, figures showing $^{40}Ar/^{39}Ar$ results and csv files of our sample data can be found in the Supplementary Information.

8. Acknowledgements

We thank V. Camp, J. Day, S. Gupta, F. M^{c}Nab, M. Mai, N. Odling, J. Roobol and J. Ruch for their help. PB acknowledges support by Shell Global and National Science Foundation Award (EAR-5329212). GR thanks the Royal Society (RG160020), NERC (IP-1635-0516; NE/T012501/1), Leverhulme Trust (RPG-2019-073), King Abdullah University of Science and Technology and the Saudi Geological Survey for their support.

9. Data Tables

Sample	A1.1	A1.5	A1.1.6	A2.3	A3.1b	A3.3a	A3.4	A3.5
Strat. Unit	Medinah	Medinah	Medinah	Shawahit	Shawahit	Shawahit	Shawahit	Shawahit
Latitude	23.311	23.251	23.27	22.731	23.194	23.175	23.143	23.144
Longitude	39.85	39.776	39.937	39.222	39.757	39.726	39.702	39.701
Elevation (m)	825	763	1007	139	682	620	564	534
Age (Ma)						2.919	3.091	3.723
Uncertainty (Ma)						0.049	0.061	0.048
Rock Type	Alk	Th	Alk	Th	Alk	Th	Th	Th
SiO_2 (wt%)	45.66	46.76	45.78	47.90	47.08	48.05	48.11	45.54
Al_2O_3	15.34	15.35	15.15	15.66	15.53	15.42	15.16	14.45
Fe_2O_3	12.51	12.03	12.49	11.55	11.70	12.19	12.11	12.19
MgO	8.14	9.06	9.15	8.34	7.78	9.20	9.57	9.44
CaO	8.64	11.03	8.95	10.74	11.07	9.73	9.89	10.28
Na_2O	3.34	2.59	3.71	2.84	2.73	2.85	2.52	2.00
K_2O	1.227	0.351	1.118	0.564	0.510	0.455	0.629	1.079
TiO_2	2.555	1.290	2.723	1.348	1.464	1.445	1.429	1.702
MnO	0.183	0.172	0.185	0.168	0.173	0.172	0.164	0.271
P_2O_5	0.689	0.153	0.536	0.196	0.224	0.193	0.230	0.379
LOI	1.14	0.90	0.02	0.53	1.55	0.05	-0.21	2.14
Total	99.42	99.68	99.81	99.84	99.81	99.76	99.61	99.47
Li (ppm)	8.544	5.968	6.999	7.003	6.159	5.916	5.757	5.681
Sc	25.065	34.247	28.341	34.295	33.634	35.260	30.499	33.075
V	207	189.7	217.7	188.4	208.2	196	185.1	193.6
Cr	262.6	358.6	327.3	334.4	335	319.4	371.4	313.9
Co	44.348	51.996	47.141	50.033	49.114	48.538	49.524	48.015
Ni	130.3	214	153.5	158.3	180.1	160.5	179.2	200.4
Cu	78.017	109.413	75.839	105.848	92.738	88.990	89.946	98.086
Zn	93.061	81.038	86.317	80.086	88.890	81.931	83.405	80.507
Ga	19.085	17.835	17.775	18.187	17.052	17.602	16.672	16.243
Rb	15.388	4.383	16.081	9.906	6.533	5.826	5.276	9.421
Sr	723.254	264.123	690.415	333.127	352.596	305.837	284.270	318.888
Y	28.891	20.570	27.249	20.605	24.212	22.031	19.773	19.007
Zr	288.157	72.711	231.021	91.458	99.262	96.219	83.017	92.738
Nb	36.762	8.897	35.074	14.525	14.300	12.753	10.865	18.869
Sn	2.132	0.801	1.964	0.920	0.987	1.000	0.972	0.895
Cs	0.099	0.023	0.159	0.093	0.035	0.044	0.027	0.073
Ba	190.730	92.307	185.345	145.188	175.241	130.406	116.994	154.620
La	36.706	6.921	29.137	10.600	10.302	9.569	8.424	12.409
Ce	76.932	15.962	61.596	22.982	23.146	21.749	19.280	25.969
Pr	9.480	2.240	7.655	2.979	3.126	2.986	2.678	3.382
Nd	38.364	10.627	31.919	13.331	14.415	13.764	12.477	14.745
Sm	7.613	2.929	6.709	3.332	3.651	3.585	3.315	3.543
Eu	2.445	1.091	2.244	1.218	1.337	1.328	1.239	1.274
Gd	6.957	3.524	6.265	3.770	4.104	4.113	3.905	3.885
Tb	1.021	0.594	0.943	0.611	0.672	0.675	0.639	0.606
Dy	5.657	3.692	5.286	3.724	4.145	4.146	3.911	3.628
Ho	1.044	0.752	0.978	0.736	0.834	0.827	0.776	0.710
Er	2.694	2.081	2.542	1.997	2.292	2.282	2.123	1.877
Tm	0.377	0.305	0.351	0.281	0.331	0.330	0.301	0.270
Yb	2.289	1.902	2.108	1.781	2.082	2.043	1.867	1.672
Lu	0.332	0.278	0.304	0.264	0.307	0.303	0.271	0.243
Hf	6.680	2.052	5.212	2.408	2.644	2.577	2.392	2.460
Ta	2.460	0.559	2.250	0.882	0.914	0.828	0.722	1.199
Tl	0.034	0.005	0.037	0.007	0.006	0.005	0.005	0.005
Pb	2.983	0.793	2.360	1.471	1.009	0.924	0.916	1.215
Th	3.290	0.577	2.739	1.166	0.879	0.804	0.703	1.188
U	1.150	0.142	0.918	0.366	0.244	0.253	0.174	0.305

Sample	A3.6a	A4.5	A4.7	A4.10	A5.1	A5.2	A5.3	A6.1
Strat. Unit	Shawahit	Shawahit	Shawahit	Shawahit	Shawahit	Shawahit	Shawahit	Shawahit
Latitude	23.151	23.114	23.091	23.047	23.026	22.983	22.819	21.952
Longitude	39.699	39.648	39.605	39.582	39.54	39.49	39.376	39.352
Elevation (m)	499	511	459	426	384	317	204	127
Age (Ma)	3.902	3.050	3.383	4.999	5.516	3.156	5.057	7.013
Uncertainty (Ma)	0.022	0.073	0.048	0.095	0.105	0.094	0.091	0.094
Rock Type	Th	Th	Th	Th	Th	Th	Alk	Alk
SiO_2 (wt%)	46.70	46.94	47.27	47.82	47.26	47.22	45.73	45.23
Al_2O_3	15.47	15.00	15.65	15.99	15.75	16.02	15.01	15.98
Fe_2O_3	11.65	12.20	12.38	12.17	12.35	12.16	12.61	12.37
MgO	7.90	10.26	9.17	6.92	8.34	8.87	8.93	6.26
CaO	9.76	10.56	10.46	10.82	10.46	10.38	10.95	12.16
Na_2O	2.77	2.52	2.62	2.94	2.57	2.68	2.91	3.03
K_2O	0.477	0.325	0.464	0.447	0.472	0.467	0.467	0.566
TiO_2	1.441	1.228	1.386	1.428	1.420	1.416	1.453	1.877
MnO	0.169	0.175	0.172	0.171	0.175	0.172	0.172	0.172
P_2O_5	0.210	0.142	0.226	0.192	0.180	0.180	0.233	0.313
LOI	3.01	0.38	0.02	1.06	0.82	0.27	1.02	1.73
Total	99.55	99.73	99.82	99.96	99.80	99.85	99.49	99.69
Li (ppm)	7.176		6.876	5.362	6.746	6.185	5.925	6.717
Sc	35.239	24.5	34.291	32.120	38.914	26.633	32.074	34.008
V	205.6	187.8	174.7	193.2	190.5	196.4	177.7	199.8
Cr	331.8	407	369.7	317.3	330.2	329.4	335	140.4
Co	48.924		52.748	45.683	55.666	52.053	56.584	48.788
Ni	165.7	254.7	208.5	159	181.2	181.7	218.4	101.4
Cu	88.576	87.2	94.403	80.411	97.322	95.512	96.658	102.131
Zn	86.807		86.706	76.629	90.718	80.629	88.072	79.588
Ga	16.330		17.737	16.052	19.027	16.938	17.203	17.259
Rb	23.380	4.1	5.984	4.690	7.380	7.041	8.149	7.934
Sr	465.068	281.3	334.381	308.578	356.932	301.736	335.946	528.503
Y	22.683	18.7	21.122	20.746	22.521	18.843	20.250	23.067
Zr	149.118	76.8	89.614	81.832	87.154	77.223	84.398	103.129
Nb	33.788		14.386	9.770	15.165	14.054	14.624	20.278
Sn	1.201		0.917	0.864	0.947	0.856	0.943	1.045
Cs	0.117		0.039	0.014	0.060	0.065	0.126	0.070
Ba	260.107	111.1	261.003	143.891	555.731	184.815	185.423	265.565
La	23.009		9.324	7.752	10.118	9.177	9.905	15.191
Ce	46.992		21.266	17.994	21.801	20.220	21.851	33.736
Pr	5.823		2.914	2.502	2.898	2.679	2.943	4.488
Nd	24.343		13.470	11.755	13.207	12.190	13.298	19.788
Sm	5.257		3.405	3.115	3.477	3.180	3.433	4.683
Eu	1.806		1.240	1.156	1.268	1.176	1.270	1.688
Gd	5.142		3.940	3.629	3.996	3.665	3.834	4.935
Tb	0.769		0.626	0.591	0.652	0.596	0.603	0.777
Dy	4.283		3.772	3.633	4.018	3.659	3.648	4.522
Ho	0.791		0.749	0.734	0.800	0.724	0.710	0.877
Er	2.031		2.055	1.967	2.211	2.001	1.931	2.304
Tm	0.285		0.296	0.289	0.315	0.290	0.273	0.318
Yb	1.723		1.853	1.787	1.965	1.802	1.703	2.011
Lu	0.252		0.270	0.262	0.295	0.272	0.251	0.291
Hf	3.653		2.382	2.179	2.315	2.217	2.245	2.837
Ta	2.070		0.942	0.647	0.960	0.909	0.923	1.309
Tl	0.038		0.006	0.005	0.006	0.005	0.012	0.012
Pb	1.857		0.912	0.901	0.999	0.876	0.958	0.997
Th	2.210		0.858	0.620	0.969	0.821	0.911	1.101
U	0.666		0.226	0.190	0.215	0.278	0.272	0.356

Table 1: Locations, Ar^{40}/Ar^{39} dates, major and trace element concentrations of Harrat Rahat lavas. Major elements, V, Cr and Ni calculated using XRF, all other elements calculated using LA-ICP-MS. All elements for sample A4.5 calculated using XRF. Alk = alkalic basalt; Th = tholeiitic basalt. Accompanying analytical standards and methodology are shown in Supplementary Database 1. Note that sample 1.1.6 was collected in January 2015, all other samples were collected in March 2015.

Sample	1.6	2.6a	2.6b	2.7	3.2	4.1	4.2	4.6
Strat. Unit	Shawahit	Shawahit	Shawahit	Shawahit	Shawahit	Shawahit	Shawahit	Shawahit
Latitude	23.206	22.779	22.780	22.784	23.185	23.139	23.130	23.101
Longitude	39.759	39.300	39.299	39.319	39.743	39.691	39.679	39.621
Elevation (m)	714	139	110	139	655	541	506	488
Age (Ma)	2.765	3.285	3.313	3.042	2.994	3.05	3.281	3.085
Uncertainty (Ma)	0.063	0.058	0.049	0.056	0.068	0.057	0.044	0.068

Sample	4.8	4.9	5.4	6.4
Strat. Unit	Shawahit	Shawahit	Shawahit	Shawahit
Latitude	23.078	23.061	22.806	21.687
Longitude	39.588	39.579	39.342	39.750
Elevation (m)	448	448	171	226
Age (Ma)	4.808	5.085	5.028	9.338
Uncertainty (Ma)	0.154	0.140	0.109	0.145

Table 2: Locations and $^{40}Ar/^{39}Ar$ dates for samples that were not geochemically analysed.

References

Ahmed, A.H., Moghazi, A.K.M., Moufti, M.R., Dawood, Y.H., Ali, K.A., 2016. Nature of the lithospheric mantle beneath the Arabian Shield and genesis of Al-spinel micropods: Evidence from the mantle xenoliths of Harrat Kishb, Western Saudi Arabia. Lithos 240, 119–139.

Altherr, R., Mertz-Kraus, R., Volker, F., Kreuzer, H., Henjes-Kunst, F., Lange, U., 2019. Geodynamic setting of Upper Miocene to Quaternary alkaline basalts from Harrat al 'Uwayrid (NW Saudi Arabia): Constraints from KAr dating, chemical and Sr-Nd-Pb isotope compositions, and petrological modeling. Lithos 330, 120–138.

Ball, P.W., White, N.J., Maclennan, J., Stevenson, S.N., 2021. Global influence of mantle temperature and plate thickness on intraplate volcanism. Nature Communications 12, 1–13.

Barfod, D., Mark, D.F., Tait, A., Dymock, R.C., Imlach, R., 2014. Argon extraction from geological samples by CO2 scanning laser step-heating. Geological Society, London, Special Publication 378, 79–90.

Bergman, S.C., Foland, K.A., Spera, F.J., 1981. On the origin of an amphibole-rich vein in a peridotite inclusion from the Lunar Crater Volcanic Field, Nevada, U.S.A. Earth and Planetary Science Letters 56, 343–361.

Bertrand, H., Chazot, G., Blichert-Toft, J., Thoral, S., 2003. Implications of widespread high-μ volcanism on the Arabian Plate for Afar mantle plume and lithosphere composition. Chemical Geology 198, 47–61.

Bohannon, R.G., Naeser, C.W., Schmidt, D.L., Zimmermann, R.A., 1989. The timing of uplift, volcanism, and rifting peripheral to the Red Sea: a case for passive rifting? Journal of Geophysical Research: Solid Earth 94, 1683–1701.

Bosworth, W., 2015. Geological evolution of the Red Sea: historical background, review, and synthesis, in: The Red Sea. Springer, pp. 45–78.

Brown, G.E., Schmidt, D.L., Huffman Jr, A.C., 1989. Geology of the Arabian Peninsula; shield area of western Saudi Arabia. U.S – Geological Survey Professional Paper No. 560-A. United States Government Printing Office, Washington, U.S.A.

Bruinsma, S.L., Förste, C., Abrikosov, O., Lemoine, J.M., Marty, J.C., Mulet, S., Rio, M.H., Bonvalot, S., 2014. ESA's satellite-only gravity field model via the direct approach based on all GOCE data. Geophysical Research Letters 41, 7508–7514.

Buikin, A., Trieloff, M., Korochantseva, E., Hopp, J., Kaliwoda, M., Meyer, H.P., Altherr, R., 2010. Distribution of mantle and atmospheric argon in mantle xenoliths from the Western Arabian Peninsula: constraints on timing and composition of metasomatizing agents in the lithospheric mantle. Journal of Petrology 51, 2547–2570.

Camp, V.E., Roobol, M.J., 1989. The Arabian continental alkali basalt province: Part I. Evolution of Harrat Rahat, Kingdom of Saudi Arabia. Geological Society of America Bulletin 101, 71–95.

Camp, V.E., Roobol, M.J., 1992. Upwelling asthenosphere beneath Western Arabia and its regional implications. Journal of Geophysical Research 97, 15255–15271.

Chang, S.j., Lee, S.V.D., 2011. Mantle plumes and associated fl ow beneath Arabia and East Africa. Earth and Planetary Science Letters 302, 448–454. URL: http://dx.doi.org/10.1016/j.epsl.2010.12.050, doi:10.1016/j.epsl.2010.12.050.

Chazot, G., Menzies, M., Baker, J., 1998. Pre-, syn-and post-rift volcanism on the south-western margin of the Arabian plate, in: Sedimentation and Tectonics in Rift Basins Red Sea:-Gulf of Aden. Springer, pp. 50–55.

Coltorti, M., Bonadiman, C., Faccini, B., Grégoire, M., O'Reilly, S.Y., Powell, W., 2007. Amphiboles from suprasubduction and intraplate lithospheric mantle. Lithos 99, 68–84.

Craig, H., Lupton, J., 1981. Helium-3 and mantle volatiles in the ocean and oceanic crust. The oceanic lithosphere 7, 391.

Davies, G.F., 1994. Thermochemical erosion of the lithosphere by mantle plumes. Journal of Geophysical Research 99, 15,709–15,722.

Divins, D., 2008. NGDC total sediment thickness of the world's oceans and marginal seas. Boulder, CO: National Oceanic and Atmospheric Administration .

Downs, D., 2019. Major-and trace-element chemical analyses of rocks from the northern Harrat Rahat volcanic field and surrounding area, Kingdom of Saudi Arabia. US Geological Survey data release .

Downs, D.T., Stelten, M.E., Champion, D.E., Dietterich, H.R., Nawab, Z., Zahran, H., Hassan, K., Shawali, J., 2018. Volcanic history of the northernmost part of the Harrat Rahat volcanic field, Saudi Arabia. Geosphere 14, 1253–1282. doi:10.1130/GES01625.1.

Duncan, R.A., Kent, A.J., Thornber, C.R., Schlieder, T.D., Al-Amri, A.M., 2016. Timing and composition of continental volcanism at Harrat Hutaymah, western Saudi Arabia. Journal of Volcanology and Geothermal Research 313, 1–14. URL: http://dx.doi.org/10.1016/j.jvolgeores.2016.01.010, doi:10.1016/j.jvolgeores.2016.01.010.

Fitton, J., Saunders, A., Norry, M., Hardarson, B., Taylor, R., 1997. Thermal and chemical structure of the Iceland plume. Earth and Planetary Science Letters 153, 197–208.

Foley, S., 1992. Vein-plus-wall-rock melting mechanisms in the lithosphere and the origin of potassic alkaline magmas. Lithos 28, 435–453.

French, S.W., Romanowicz, B., 2015. Broad plumes rooted at the base of the Earth's mantle beneath major hotspots. Nature 525, 95–99.

Gast, P.W., 1968. Trace element fractionation and the origin of tholeiitic and alkaline magma types. Geochimica et Cosmochimica Acta 32, 1057–1086.

Gettings, M.E., Blank Jr, H., Mooney, W., Healey, J., 1986. Crustal structure of southwestern Saudi Arabia. Journal of Geophysical Research: Solid Earth 91, 6491–6512.

Green, T.H., Ringwood, A., 1966. Origin of the calc-alkaline igneous rock suite. Earth and Planetary Science Letters 1, 307–316.

Gualda, G.A., Ghiorso, M.S., Lemons, R.V., Carley, T.L., 2012. Rhyolite-MELTS: a modified calibration of MELTS optimized for silica-rich, fluid-bearing magmatic systems. Journal of Petrology 53, 875–890.

Halldõrsson, S.A., Hilton, D.R., Scarsi, P., Abebe, T., Hopp, J., 2014. A common mantle plume source beneath the entire East

African Rift System revealed by coupled helium-neon systematics. Geophysical Research Letters 41, 2304–2311. doi:10.1002/2014GL059424.

Hansen, S., Schwartz, S., Al-Amri, A., Rodgers, A., 2006. Combined plate motion and density-driven flow in the asthenosphere beneath Saudi Arabia: Evidence from shear-wave splitting and seismic anisotropy. Geology 34, 869–872.

Hansen, S.E., Rodgers, A.J., Schwartz, S.Y., Al-Amri, A.M., 2007. Imaging ruptured lithosphere beneath the Red Sea and Arabian Peninsula. Earth and Planetary Science Letters 259, 256–265.

Henjes-Kunst, F., Altherr, R., Baumann, A., 1990. Evolution and composition of the lithospheric mantle underneath the western Arabian peninsula: constraints from Sr- Nd isotope systematics of mantle xenoliths. Contributions to Mineralogy and Petrology 105, 460–472.

Hofmann, C., Courtillot, V., Feraud, G., Rochette, P., Yirgu, G., Ketefo, E., Pik, R., 1997. Timing of the Ethiopian flood basalt event and implications for plume birth and global change. Nature 389, 838.

Hoggard, M.J., Winterbourne, J., Czarnota, K., White, N., 2017. Oceanic residual depth measurements, the plate cooling model and global dynamic topography. Journal of Geophysical Research: Solid Earth 122, 2328–2372. doi:10.1002/2016JB013457.

Iacovino, K., 2021. Ferric/ferrous, fe^{3+}/fe^{T}, f_{O2} converter (kress and carmichael, 1991) (3.2). Zenodo https://doi.org/10.5281/zenodo.5907844.

Irvine, T.N., Baragar, W.R.A., 1971. A Guide to the Chemical Classification of the Common Volcanic Rocks. Canadian Journal of Earth Sciences 8, 523–548.

Jennings, E.S., Holland, T.J.B., 2015. A simple thermodynamic model for melting of peridotite in the system NCFMASOCr. Journal of Petrology 56, 869–892. doi:10.1093/petrology/egv020.

Kaliwoda, M., Altherr, R., Meyer, H.p., 2007. Composition and thermal evolution of the lithospheric mantle beneath the Harrat Uwayrid , eastern flank of the Red Sea rift (Saudi Arabia). Lithos 99, 105–120. doi:10.1016/j.lithos.2007.06.013.

Katz, R.F., Spiegelmann, M., Langmuir, C.H., 2003. A new parameterization of hydrous mantle melting. Geochemistry, Geophysics, Geosystems 4. doi:10.1029/2002GC000433.

Kay, R.W., Gast, P.W., 1973. The rare earth content and origin of alkali-rich basalts. The Journal of Geology 81, 653–682.

Kogiso, T., Hirose, K., Takahashi, E., 1998. Melting experiments on homogeneous mixtures of peridotite and basalt: application to the genesis of ocean island basalts. Earth and Planetary Science Letters 162, 45–61.

Konrad, K., Graham, D.W., Thornber, C.R., Duncan, R.A., Kent, A.J., Al-Amri, A.M., 2016. Asthenosphere–lithosphere interactions in Western Saudi Arabia: Inferences from $^{3}He/^{4}He$ in xenoliths and lava flows from Harrat Hutaymah. Lithos 248, 339–352.

Kress, V.C., Carmichael, I.S., 1991. The compressibility of silicate liquids containing Fe_2O_3 and the effect of composition, temperature, oxygen fugacity and pressure on their redox states. Contributions to Mineralogy and Petrology 108, 82–92.

Krienitz, M.S., Haase, K., Mezger, K., van den Bogaard, P., Thiemann, V., Shaikh-Mashail, M., 2009. Tectonic events, continental intraplate volcanism, and mantle plume activity in northern Arabia: Constraints from geochemistry and Ar-Ar dating of Syrian lavas. Geochemistry, Geophysics, Geosystems 10.

Le Maitre, R.W., 2002. Igneous Rocks. A Classification and Glossary of Terms. Recommendations of the International Union of Geological Sciences Subcommission on the Systematics of Igneous Rocks. 2nd ed., Cambridge University Press, Cambridge.

Lee, C.T.A., Luffi, P., Plank, T., Dalton, H., Leeman, W.P., 2009. Constraints on the depths and temperatures of basaltic magma generation on Earth and other terrestrial planets using new thermobarometers for mafic magmas. Earth and Planetary Science Letters 279, 20–33. doi:10.1016/j.epsl.2008.12.020.

Lee, J.Y., Marti, K., Severinghaus, J.P., Kawamura, K., Yoo, H.S., Lee, J.B., Kim, J.S., 2006. A redetermination of the isotopic abundances of atmospheric Ar. Geochimica et Cosmochimica Acta 70, 4507–4512. doi:10.1016/j.gca.2006.06.1563.

Lim, J.A., Chang, S.J., Mai, P.M., Zahran, H., 2020. Asthenospheric Flow of Plume Material Beneath Arabia Inferred From S Wave Traveltime Tomography. Journal of Geophysical Research: Solid Earth 125, e2020JB019668.

Lustrino, M., Sharkov, E., 2006. Neogene volcanic activity of western Syria and its relationship with Arabian plate kinematics. Journal of Geodynamics 42, 115–139. doi:10.1016/j.jog.2006.06.003.

Mark, D., Stuart, F., de Podesta, M., 2011. New high-precision measurements of the isotopic composition of atmospheric argon. Geochimica et Cosmochimica Acta 75, 7494–7501. doi:10.1016/j.gca.2011.09.042.

Mark, D.F., Barfod, D., Stuart, F., Imlach, J., 2009. The ARGUS multicollector noble gas mass spectrometer: Performance for $^{40}Ar/^{39}Ar$ geochronology. Geochemistry, Geophysics, Geosystems 10, 1–9.

Mark, D.F., Renne, P.R., Dymock, R., Smith, V.C., Simon, J.I., Morgan, L.E., Staff, R.A., 2017. High-precision $^{40}Ar/^{39}Ar$ dating of Pleistocene Tuffs and temporal anchoring of the Matuyama-Brunhes Boundary. Quaternary Geochronology 39, 1–23.

Marty, B., Gezahegn, Y., et al., 1996. Helium isotopic variations in Ethiopian plume lavas: nature of magmatic sources and limit on lower mantle contribution. Earth and Planetary Science Letters 144, 223–237.

Marty, B., Zimmermann, L., 1999. Volatiles (He, C, N, Ar) in mid-ocean ridge basalts: Assessment of shallow-level fractionation and characterization of source composition. Geochimica et Cosmochimica Acta 63, 3619–3633.

McDonough, W.F., Sun, S.S., 1995. The composition of the Earth. Chemical Geology 120, 223–253. doi:10.1016/0009-2541(94)00140-4.

McGuire, A.V., 1988. Petrology of mantle xenoliths from Harrat al Kishb: the mantle beneath western Saudi Arabia. Journal of petrology 29, 73–92.

M^{c}Kenzie, D., 2020. The structure of the lithosphere and upper mantle beneath the Eastern Mediterranean and Middle East. Mediterranean Geoscience Reviews 2, 311–326.

M^{c}Nab, F., Ball, P.W., 2022. meltPT: Preliminary release (v0.0.2-alpha). Zenodo https://doi.org/10.5281/zenodo.6948031.

Medaris, L., Syada, G., 1999. Pyroxenite xenoliths from Al Ashaer Volcano, Syria: constraints on the thermal state of the subcontinental Arabian lithosphere. International Geology Review 41, 895–905.

Menzies, M., Gallagher, K., Yelland, A., Hurford, A.J., 1997. Volcanic and nonvolcanic rifted margins of the Red Sea and Gulf of Aden: crustal cooling and margin evolution in Yemen. Geochimica et Cosmochimica Acta 61, 2511–2527.

Michael, P., 1995. Regionally distinctive sources of depleted MORB: Evidence from trace elements and H_2O. Earth and Planetary Science Letters 131, 301–320. doi:10.1016/0012-821X(95)00023-6.

Moreira, M., Valbracht, P., Staudacher, T., Allègre, C., 1996. Rare gas systematics in Red Sea ridge basalts. Geophysical research letters 23, 2453–2456.

Morgan, L.E., Mark, D.F., Imlach, J., Barfod, D., Dymock, R., 2014. FCs–EK: a new sampling of the Fish Canyon Tuff $^{40}Ar/^{39}Ar$ neutron flux monitor. Geological Society, London, Special Publication 378, 63–67.

Moufti, M.R., Moghazi, A.M., Ali, K.A., 2012. Geochemistry and Sr–Nd–Pb isotopic composition of the Harrat Al-Madinah Volcanic Field , Saudi Arabia. Gondwana Research 21, 670–689. URL: http://dx.doi.org/10.1016/j.gr.2011.06.003, doi:10.1016/j.gr.2011.06.003.

Moufti, M.R., Moghazi, A.M., Ali, K.A., 2013. $^{40}Ar/^{39}Ar$ geochronology of the Neogene-Quaternary Harrat Al-Madinah intercontinental volcanic field, Saudi Arabia: Implications for duration and migration of volcanic activity. Journal of Asian Earth Sciences 62, 253–268. URL: http://dx.doi.org/10.1016/j.jseaes.2012.09.027, doi:10.1016/j.jseaes.2012.09.027.

M^{c}Nab, F., Ball, P.W., in review. meltPT: A Python package for basaltic whole-rock thermobarometric analysis with application to Hawai'i. Volcanica .

M^{c}Nab, F., Ball, P.W., Hoggard, M.J., White, N.J., 2018. Neogene uplift and magmatism of Anatolia: Insights from drainage analysis and basaltic geochemistry. Geochemistry, Geophysics, Geosystems 19, 175–213.

Murcia, H., Lindsay, J.M., Niedermann, S., Cronin, S.J., Smith, I., El-Masry, N.N., Moufti, M.R.H., Németh, K., 2013. The potential use of cosmogenic nuclides for dating in Harrat Rahat, in: VORISA Scientific Meeting extended abstract, pp. 24–28.

Murcia, H., Lindsay, J.M., Németh, K., Smith, I.E.M., Cronin, S.J., Moufti, M.R.H., El-Masry, N.N., Niedermann, S., 2017. Geology and geochemistry of Late Quaternary volcanism in northern Harrat Rahat, Kingdom of Saudi Arabia: implications for eruption dynamics, regional stratigraphy and magma evolution, in: Monogenetic Volcanism. The Geological Society of London, pp. 173–204. URL: https://doi.org/10.1144/SP446.2, doi:10.1144/SP446.2.

Murcia, H., Németh, K., El-Masry, N., Lindsay, J., Moufti, M., Wameyo, P., Cronin, S., Smith, I., Kereszturi, G., 2015. The Al-Du'aythah volcanic cones, Al-Madinah City: implications for volcanic hazards in northern Harrat Rahat, Kingdom of Saudi Arabia. Bulletin of Volcanology 77, 54.

Nasir, S., Rollinson, H., 2009. The nature of the subcontinental lithospheric mantle beneath the Arabian Shield: Mantle xenoliths from southern Syria. Precambrian Research 172, 323–333.

Park, Y., Nyblade, A.A., Rodgers, A.J., Al-Amri, A., 2008. S wave velocity structure of the Arabian Shield upper mantle from Rayleigh wave tomography. Geochemistry, Geophysics, Geosystems 9.

Pearce, J.A., 1975. Basalt geochemistry used to investigate past tectonic environments on Cyprus. Tectonophysics 25, 41–67.

Pearce, J.A., Norry, M.J., 1979. Petrogenetic implications of Ti, Zr, Y, and Nb variations in volcanic rocks. Contributions to mineralogy and petrology 69, 33–47.

Pik, R., Bellahsen, N., Leroy, S., Denèle, Y., Razin, P., Ahmed, A., Khanbari, K., 2013. Structural control of basement denudation during rifting revealed by low-temperature (U–Th–Sm)/He thermochronology of the Socotra Island basement—Southern Gulf of Aden margin. Tectonophysics 607, 17–31.

Pik, R., Marty, B., Hilton, D.R., 2006. How many mantle plumes in Africa? The geochemical point of view. Chemical Geology 226, 100–114.

Plank, T., Forsyth, D., 2016. Thermal structure and melting conditions in the mantle beneath the Basin and Range province from seismology and petrology. Geochemistry, Geophysics, Geosystems 17, 1312–1338. doi:10.1002/2015GC006205.

Preece, K., Mark, D.F., Barclay, J., Cohen, B.E., Chamberlain, K.J., Jowitt, C., Vye-Brown, C., Brown, R.J., Hamilton, S., 2018. Bridging the gap: $^{40}Ar/^{39}Ar$ dating of volcanic eruptions from the 'Age of Discovery'. Geology 46, 1035–1038. doi:10.1130/G45415.1.

Renne, P.R., Balco, G., Ludwig, K.R., Mundil, R., Min, K., 2011. Response to the comment by WH Schwarz et al. on "Joint determination of ^{40}K decay constants and $^{40}Ar*/^{40}K$ for the Fish Canyon sanidine standard, and improved accuracy for $^{40}Ar/^{39}Ar$ geochronology" by PR Renne et al. (2010). Geochimica et Cosmochimica Acta 75, 5097–5100.

Renne, P.R., Mundil, R., Balco, G., Min, K., Ludwig, K.R., 2010. Joint determination of ^{40}K decay constants and $^{40}Ar*/^{40}K$ for the Fish Canyon sanidine standard, and improved accuracy for $^{40}Ar/^{39}Ar$ geochronology. Geochimica et Cosmochimica Acta 74, 5349–5367. doi:10.1016/j.gca.2010.06.017.

Richards, F.D., Hoggard, M.J., White, N., Ghelichkhan, S., 2020. Quantifying the relationship between short-wavelength dynamic topography and thermomechanical structure of the upper mantle using calibrated parameterization of anelasticity. Journal of Geophysical Research: Solid Earth , e2019JB019062.

Rochette, P., Tamrat, E., Féraud, G., Pik, R., Courtillot, V., Ketefo, E., Coulon, C., Hoffmann, C., Vandamme, D., Yirgu, G., 1998. Magnetostratigraphy and timing of the Oligocene Ethiopian traps. Earth and Planetary Science Letters 164, 497–510.

Rudge, J.F., Shaw Champion, M.E., White, N.J., McKenzie, D., Lovell, B., 2008. A plume model of transient diachronous uplift at the Earth's surface. Earth and Planetary Science Letters 267, 146–160. doi:10.1002/2014JF003297.

Runge, M.G., Bebbington, M.S., Cronin, S.J., Lindsay, J.M., Kenedi, C.L., Moufti, M.R.H., 2014. Vents to events: determining an eruption event record from volcanic vent structures for the Harrat Rahat, Saudi Arabia. Bulletin of Volcanology 76, 1–16.

Rutte, D., Becker, T.A., Deino, A.L., Reese, S.R., Renne, P.R., Schickler, R.A., 2018. The New CLOCIT Irradiation Facility for $^{40}Ar/^{39}Ar$ Geochronology: Characterisation, Comparison with CLICIT and Implications for High-Precision Geochronology. Geostandards and Geoanalytical Research 42, 301–307. doi:10.1111/ggr.12217.

Sanfilippo, A., Jácome, A.P.G., Ligi, M., et al., 2019. Geochemistry of the lunayyir and khaybar volcanic fields (Saudi Arabia):

insights into the origin of cenozoic Arabian Volcanism, in: Geological Setting, Palaeoenvironment and Archaeology of the Red Sea. Springer, pp. 389–415.

Schaeffer, A.J., Lebedev, S., 2013. Global shear speed structure of the upper mantle and transition zone. Geophysical Journal International 194, 417–449. doi:10.1093/gji/ggt095.

Schaen, A.J., Jicha, B.R., Hodges, K.V., Vermeesch, P., Stelten, M.E., Mercer, C.M., Phillips, D., Rivera, T.A., Jourdan, F., Matchan, E.L., Hemming, S.R., Morgan, L.E., Kelley, S.P., Cassata, W.S., Heizler, M.T., Vasconcelos, P.M., Benowitz, J.A., Koppers, A.A., Mark, D.F., Niespolo, E.M., Sprain, C.J., Hames, W.E., Kuiper, K.F., Turrin, B.D., Renne, P.R., Ross, J., Nomade, S., Guillou, H., Webb, L.E., Cohen, B.A., Calvert, A.T., Joyce, N., Ganerød, M., Wijbrans, J., Ishizuka, O., He, H., Ramirez, A., Pfänder, J.A., Lopez-Martínez, M., Qiu, H., Singer, B.S., 2020. Interpreting and reporting $^{40}Ar/^{39}Ar$ geochronologic data. GSA Bulletin 133, 461–487. doi:10.1130/B35560.1.

Schilling, J., 1973. Afar mantle plume: rare earth evidence. Nature Physical Science 242, 2–5.

Shaw, J., Baker, J., Kent, A., Ibrahim, K., Menzies, M., 2007. The geochemistry of the Arabian lithospheric mantle—a source for intraplate volcanism? Journal of petrology 48, 1495–1512.

Shaw, J.E., Baker, J.A., Menzies, M.A., Thirlwall, M.F., Ibrahim, K.M., 2003. Petrogenesis of the Largest Intraplate Volcanic Field on the Arabian Plate (Jordan): a Mixed Lithosphere-Asthenosphere Source Activated by Lithospheric Extension. Journal of Petrology 44, 1657–1679. doi:10.1093/petrology/egg052.

Späth, A., Le Roex, A.P., Opiyo-akech, N., 2001. Plume-Lithosphere Interaction and the Origin of Continental Rift-related Alkaline Volcanism – the Chyulu Hills Volcanic Province, Southern Kenya. Journal of Petrology 42, 765–787.

Stein, M., 2003. Tracing the plume material in the Arabian-Nubian Shield. Precambrian Research 123, 223–234.

Stein, M., Navon, O., Kessel, R., 1997. Chromatographic metasomatism of the Arabian—Nubian lithosphere. Earth and Planetary Science Letters 152, 75–91.

Stelten, M.E., Downs, D.T., Champion, D.E., Dietterich, H.R., Calvert, A.T., Sisson, T.W., Mahood, G.A., Zahran, H., 2020. The timing and compositional evolution of volcanism within northern Harrat Rahat, Kingdom of Saudi Arabia. Bulletin 132, 1381–1403.

Stelten, M.E., Downs, D.T., Dietterich, H.R., Mahood, G.A., Calvert, A.T., Sisson, T.W., Zahran, H., Shawali, J., 2018. Timescales of magmatic differentiation from alkali basalt to trachyte within the Harrat Rahat volcanic field, Kingdom of Saudi Arabia. Contributions to Mineralogy and Petrology 173, 1–17.

Tang, Z., Julià, J., Zahran, H., Mai, P.M., 2016. The lithospheric shear-wave velocity structure of Saudi Arabia: young volcanism in an old shield. Tectonophysics 680, 8–27.

Tang, Z., Mai, P.M., Julià, J., Zahran, H., 2019. Shear velocity structure beneath Saudi Arabia from the joint inversion of P and S wave receiver functions, and Rayleigh wave group velocity dispersion data. Journal of Geophysical Research: Solid Earth 124, 4767–4787.

Trifonov, V.G., Dodonov, A.E., Sharkov, E.V., Golovin, D.I., Chernyshev, I.V., Lebedev, V.A., Ivanova, T.P., Bachmanov, D.M., Rukieh, M., Ammar, O., Minini, H., Al Kafri, A.M., Ali, O., 2011. New data on the Late Cenozoic basaltic volcanism in Syria, applied to its origin. Journal of Volcanology and Geothermal Research 199, 177–192. URL: http://dx.doi.org/10.1016/j.jvolgeores.2010.01.013, doi:10.1016/j.jvolgeores.2010.01.013.

Varne, R., 1970. Hornblende lherzolite and the upper mantle. Contributions to Mineralogy and Petrology 27, 45–51.

Weinstein, Y., Navon, O., Altherr, R., Stein, M., 2006. The role of lithospheric mantle heterogeneity in the generation of Plio-Pleistocene alkali basaltic suites from NW Harrat Ash Shaam (Israel). Journal of Petrology 47, 1017–1050.

Wilson, J.W., Roberts, G.G., Hoggard, M.J., White, N.J., 2014. Cenozoic epeirogeny of the Arabian Peninsula from drainage modeling. Geochemistry, Geophysics, Geosystems 15, 3723–3761. doi:10.1002/2014GC005283.Received.

Yao, Z., Mooney, W.D., Zahran, H.M., Youssef, S.E.H., 2017. Upper mantle velocity structure beneath the Arabian shield from Rayleigh surface wave tomography and its implications. Journal of Geophysical Research: Solid Earth 122, 6552–6568.

Supplementary Materials for Evolution of intraplate magmatism atop a mantle plume: Geochemical and chronological analysis of Shawahit Basalt, Harrat Rahat, Saudi Arabia

P.W. Ball[a,], G.G. Roberts[b,], D.F. Mark[c], D.N. Barfod[c], N.J. White[d], B.H. Lodhia[e], M.M. Nahdi[f], S. Garni[f]

[a]*Department of Geosciences, Colorado State University, Fort Collins, CO, USA*
[b]*Department of Earth Science & Engineering, Imperial College London, London, UK*
[c]*NERC Argon Isotope Facility, SUERC, East Kilbride, UK*
[d]*Bullard Laboratories, Department of Earth Science, University of Cambridge, Cambridge, UK*
[e]*School of Minerals and Energy Resources, UNSW Sydney, Australia*
[f]*Saudi Geological Survey, Jeddah, Saudi Arabia*

Abstract

This supporting information document has four sections. The first section summarises supplementary datasets for $^{40}Ar/^{39}Ar$ dating and for geochemical data presented in the main manuscript. The second section presents Ar/Ar spectra and isochron plots for all dated samples. Section 3 describes the methodologies used to determine major and trace element compositions. Finally, Section 4 presents extended data tables for measured oxides, major and trace elements.

1. Supplementary Datasets

1.1. Dataset S1: New $^{40}Ar/^{39}Ar$ Data

Dataset S1 is a spreadsheet containing three sheets summarising the dating results. The first sheet summarises ages and includes estimates of uncertainty, step counts and number of plateau steps. The second sheet summarises experimental parameters including atmospheric argon ratios, production rates, decay constants and standards. The final sheet presents the raw data including measured Ar/Ar ratios and J scores.

1.2. Dataset S2: New and Published Geochemical Data

Dataset S2 presents the new radiometric ages, major-element and trace-element concentrations for all samples presented in Table 1 of the main text. In addition, all published data used in the generation of main-text figures and mantle potential temperature estimates are presented (Brown et al., 1989; Camp and Roobol, 1989; Altherr et al., 1990; Bertrand et al., 2003; Moufti et al., 2012, 2013; Murcia et al., 2015, 2017; Stelten et al., 2018; Downs et al., 2018; Downs, 2019). Estimates of pressure and temperature of melt equilibration are also presented.

2. $^{40}Ar/^{39}Ar$ Dating: Spectra and Isochron plots for all samples

Figures 1 to 23 show spectra and isochron plots for samples dated in this study. See Figures 1–2 and Tables 1–2 of the main manuscript for their locations. A subset of these results are shown in Figure 4 of the main manuscript. The dating methodology is described in the main manuscript.

Email addresses: patrick.ball@colostate.edu (P.W. Ball), gareth.roberts@imperial.ac.uk (G.G. Roberts)

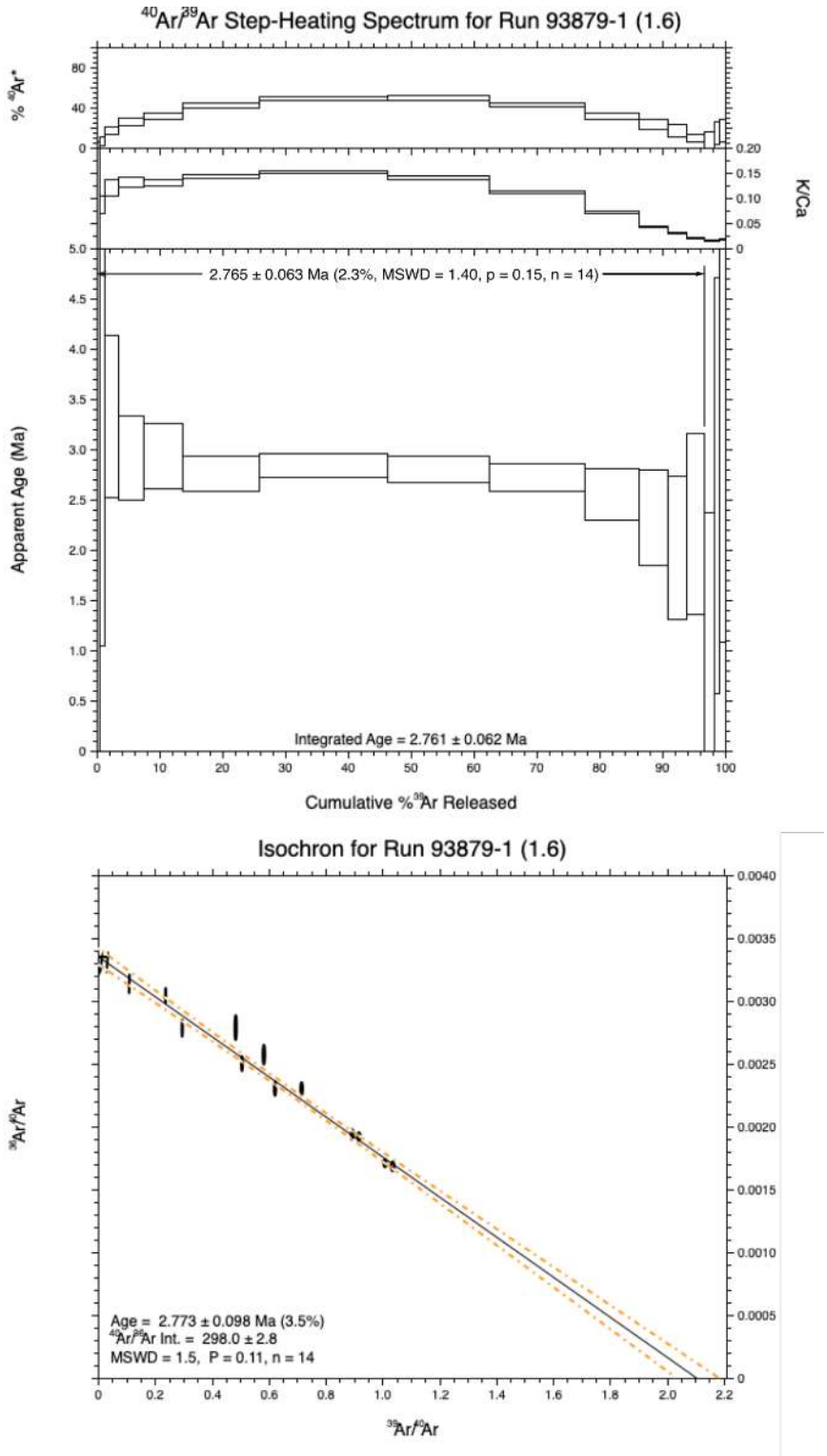

Figure 1: $^{40}Ar/^{39}Ar$ incremental heating analyses of Harrat Rahat sample 1.6.

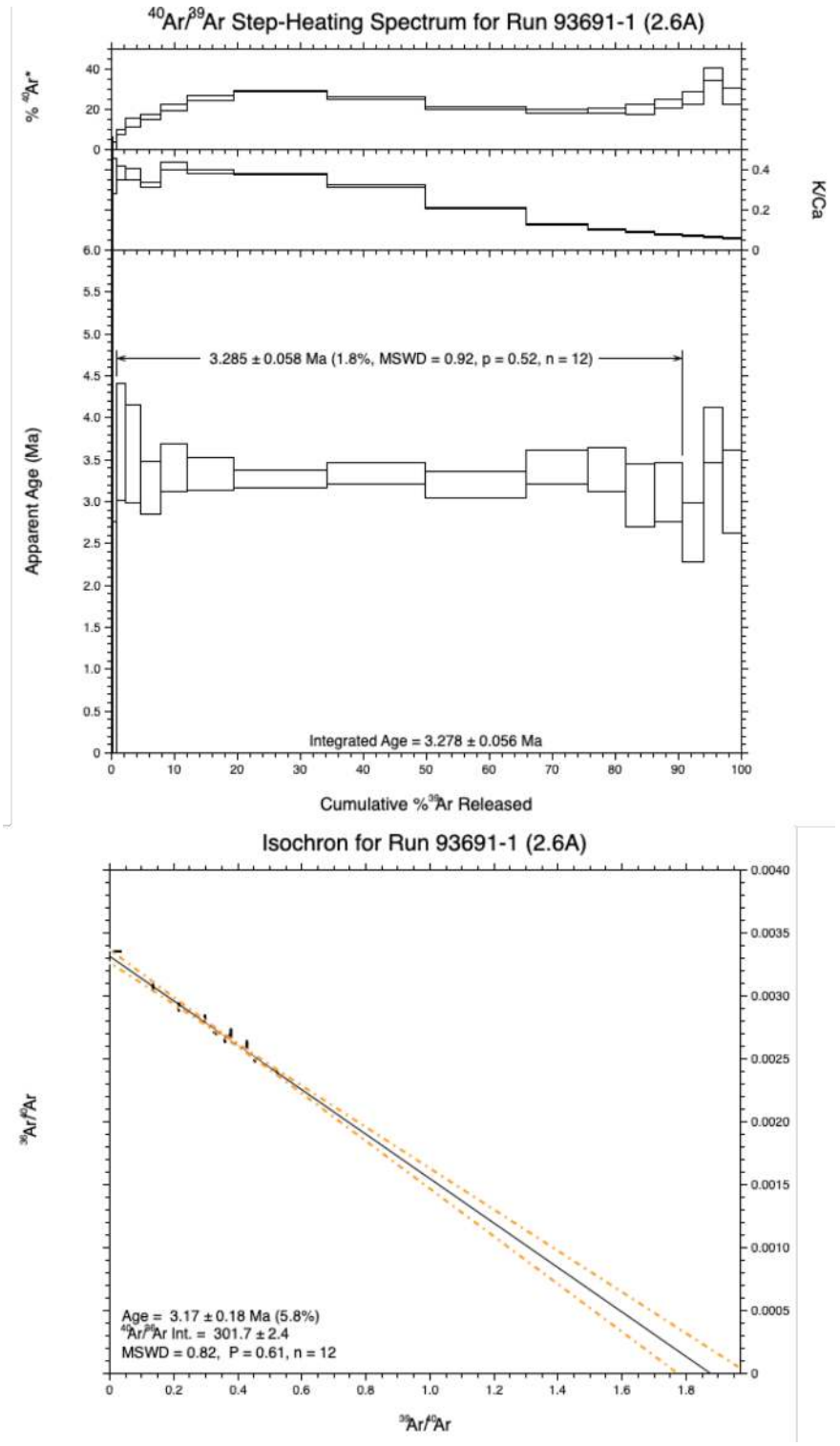

Figure 2: $^{40}Ar/^{39}Ar$ incremental heating analyses of Harrat Rahat sample 2.6A.

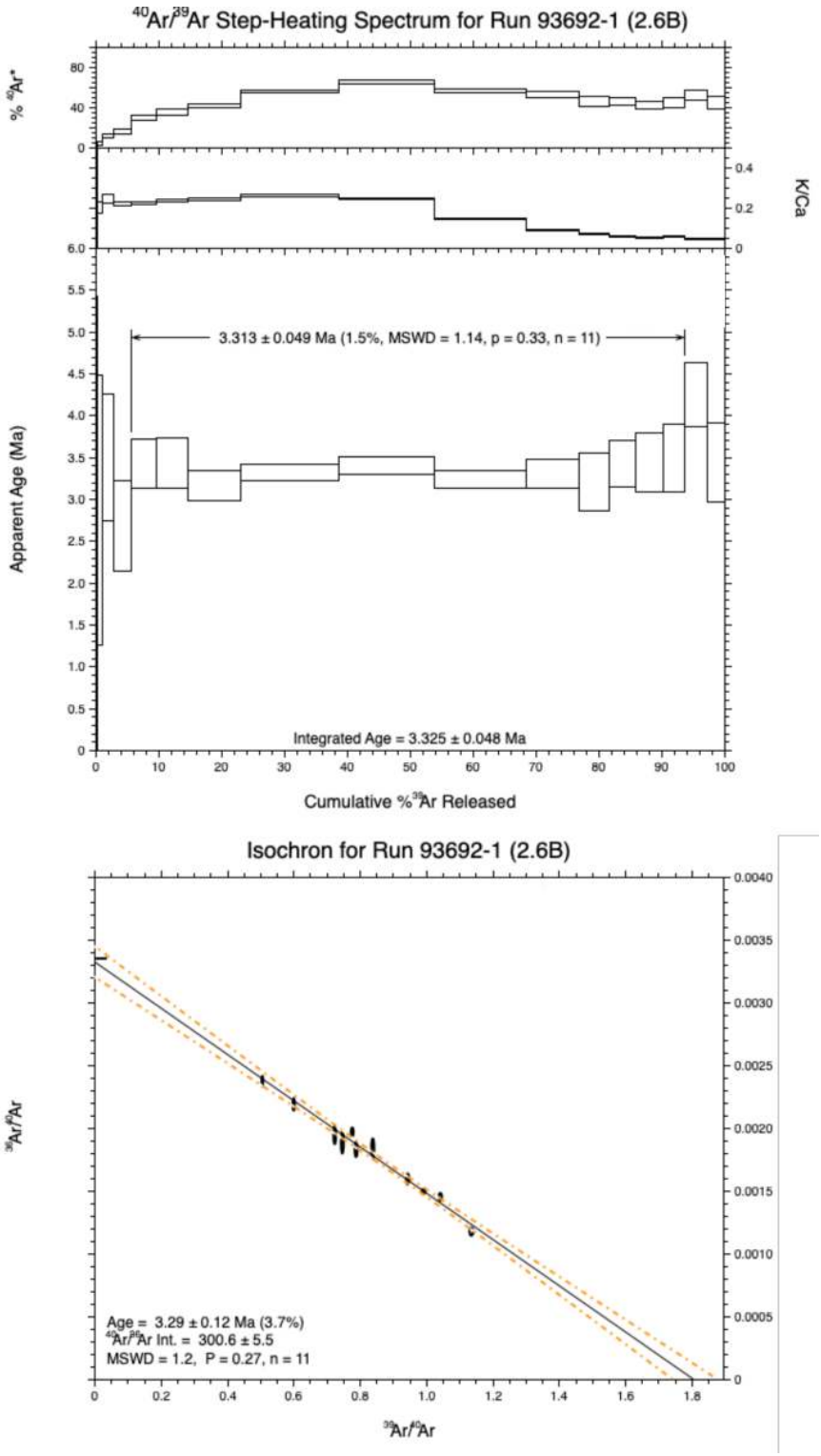

Figure 3: $^{40}Ar/^{39}Ar$ incremental heating analyses of Harrat Rahat sample 2.6B.

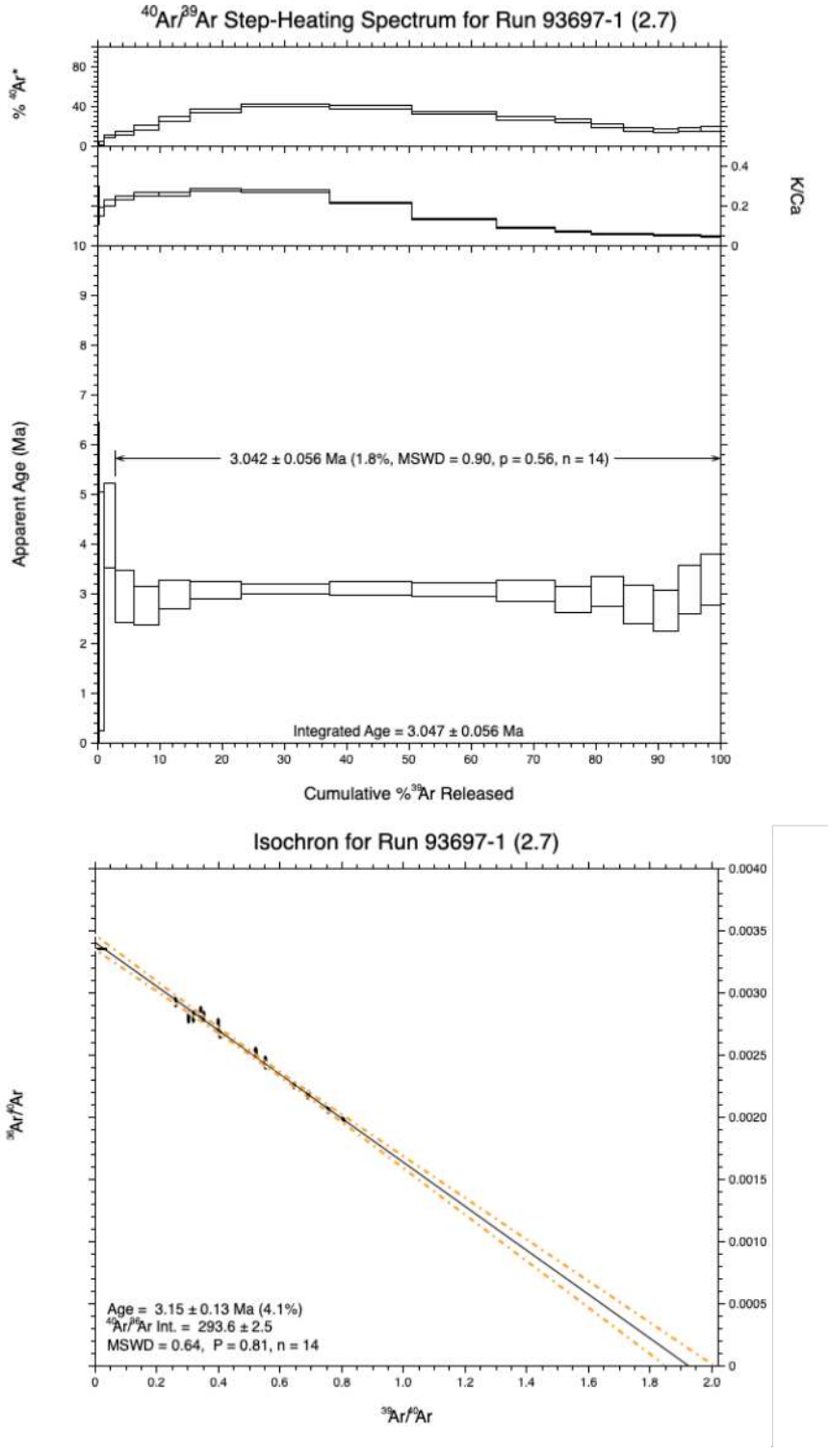

Figure 4: $^{40}Ar/^{39}Ar$ incremental heating analyses of Harrat Rahat sample 2.7.

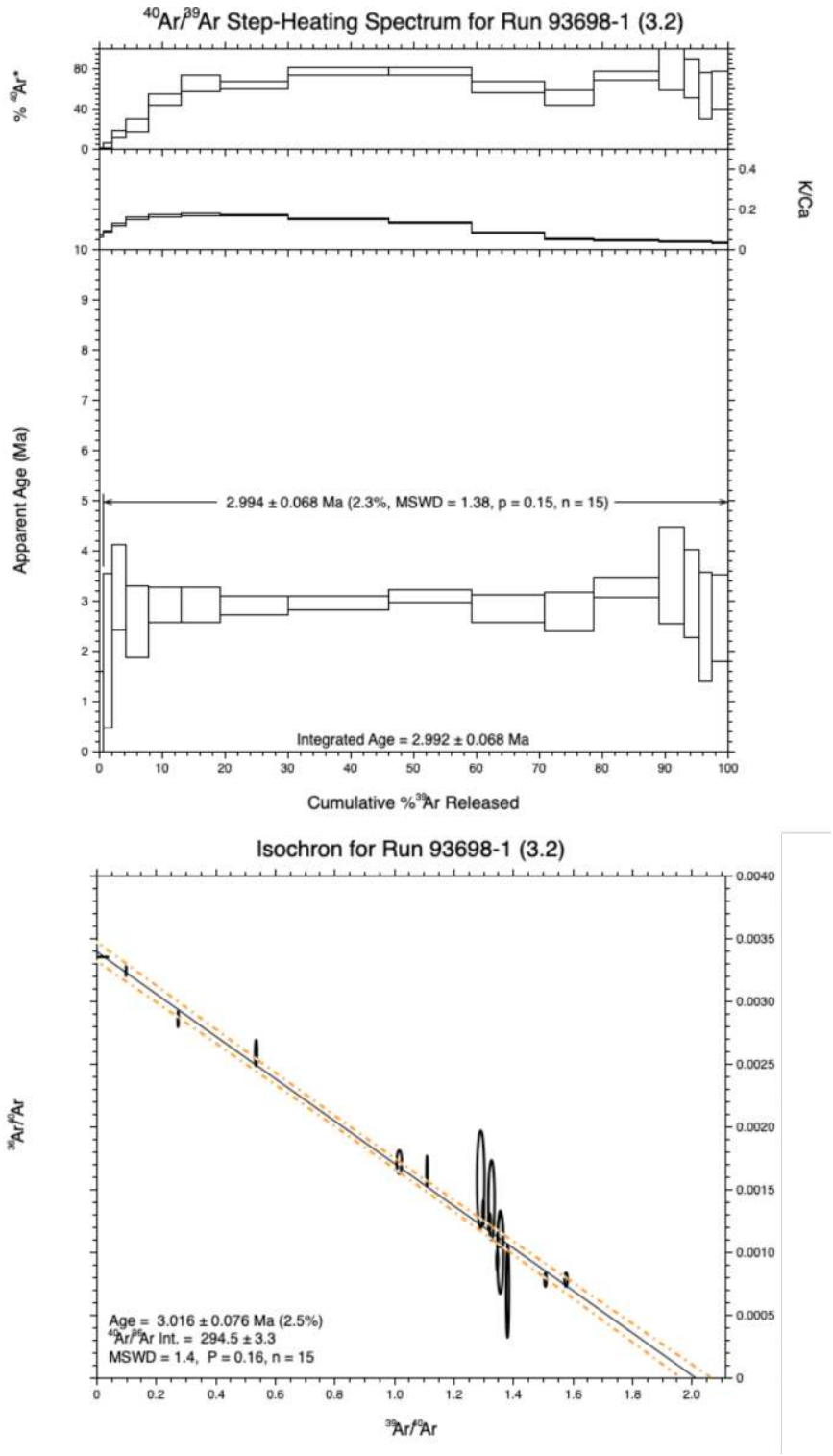

Figure 5: $^{40}Ar/^{39}Ar$ incremental heating analyses of Harrat Rahat sample 3.2.

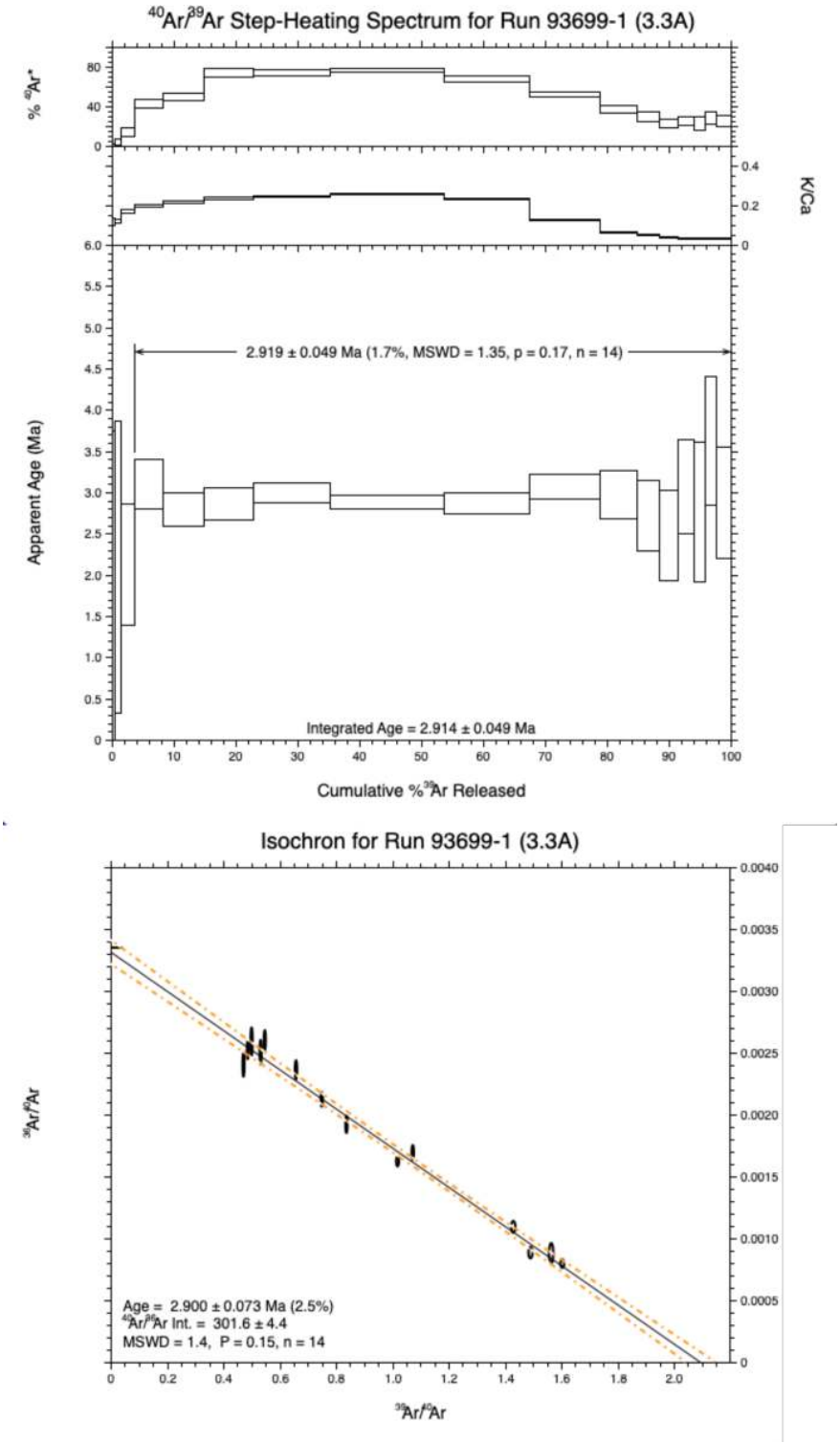

Figure 6: $^{40}Ar/^{39}Ar$ incremental heating analyses of Harrat Rahat sample 3.3A.

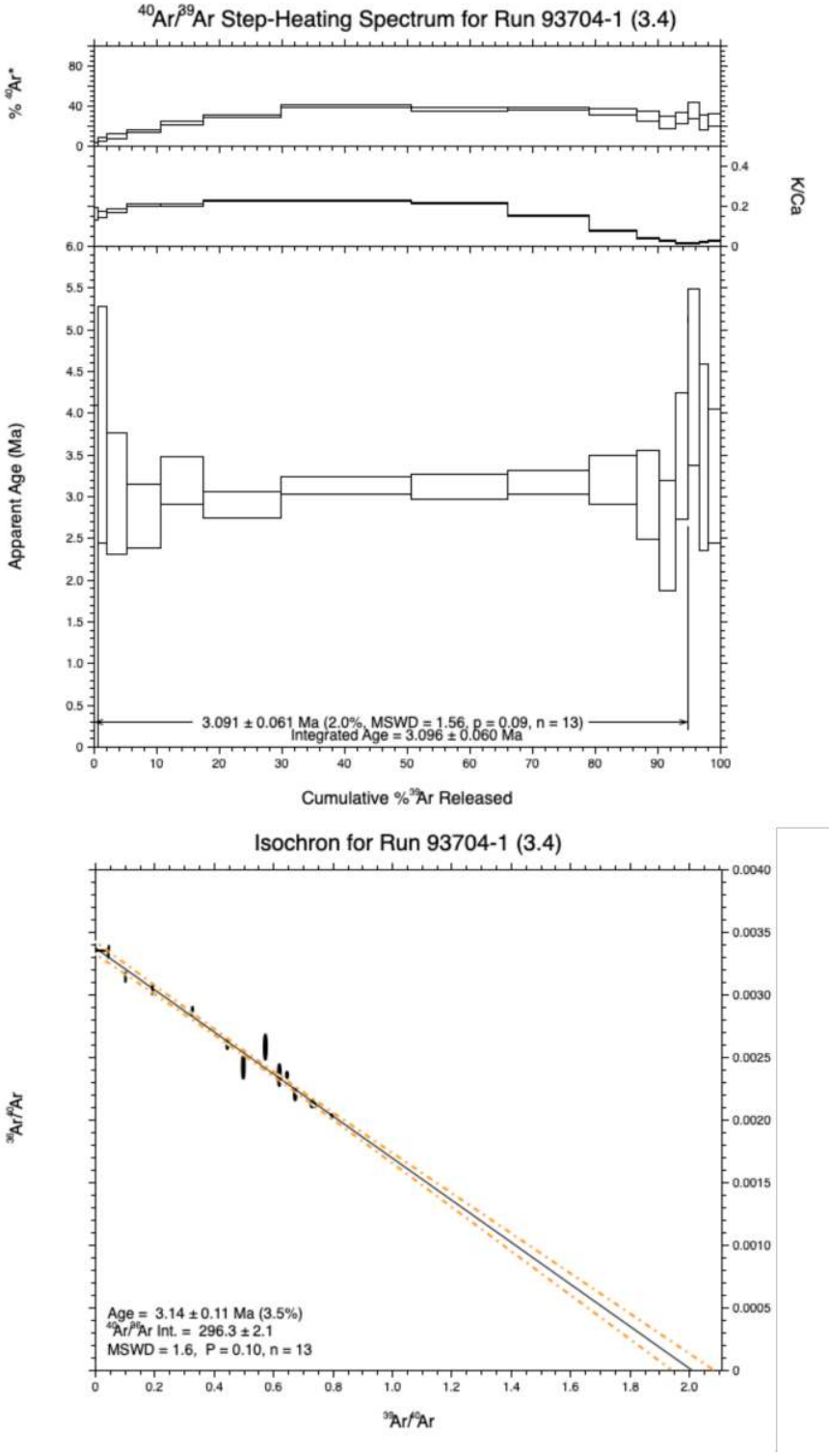

Figure 7: $^{40}Ar/^{39}Ar$ incremental heating analyses of Harrat Rahat sample 3.4.

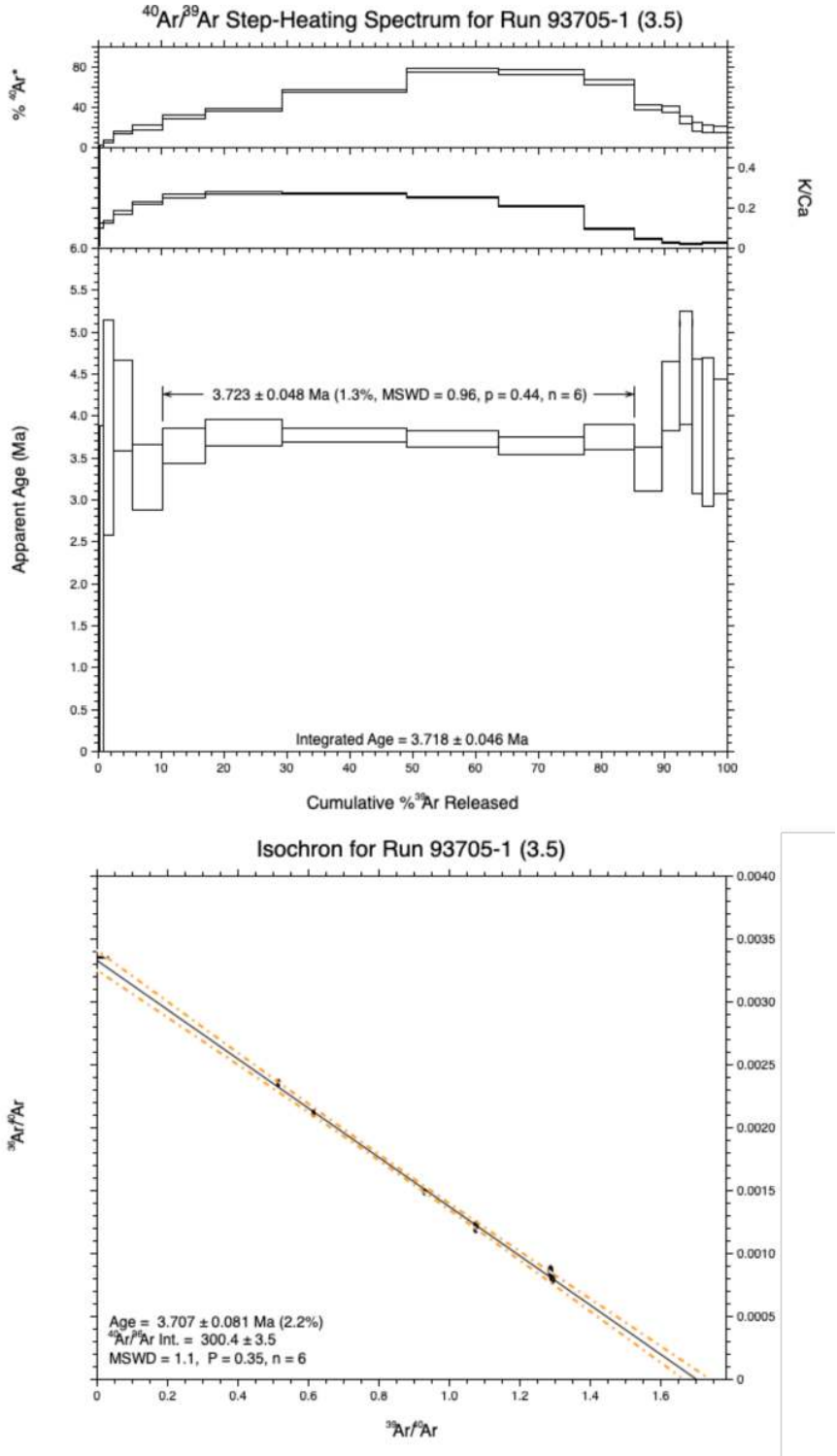

Figure 8: $^{40}Ar/^{39}Ar$ incremental heating analyses of Harrat Rahat sample 3.5.

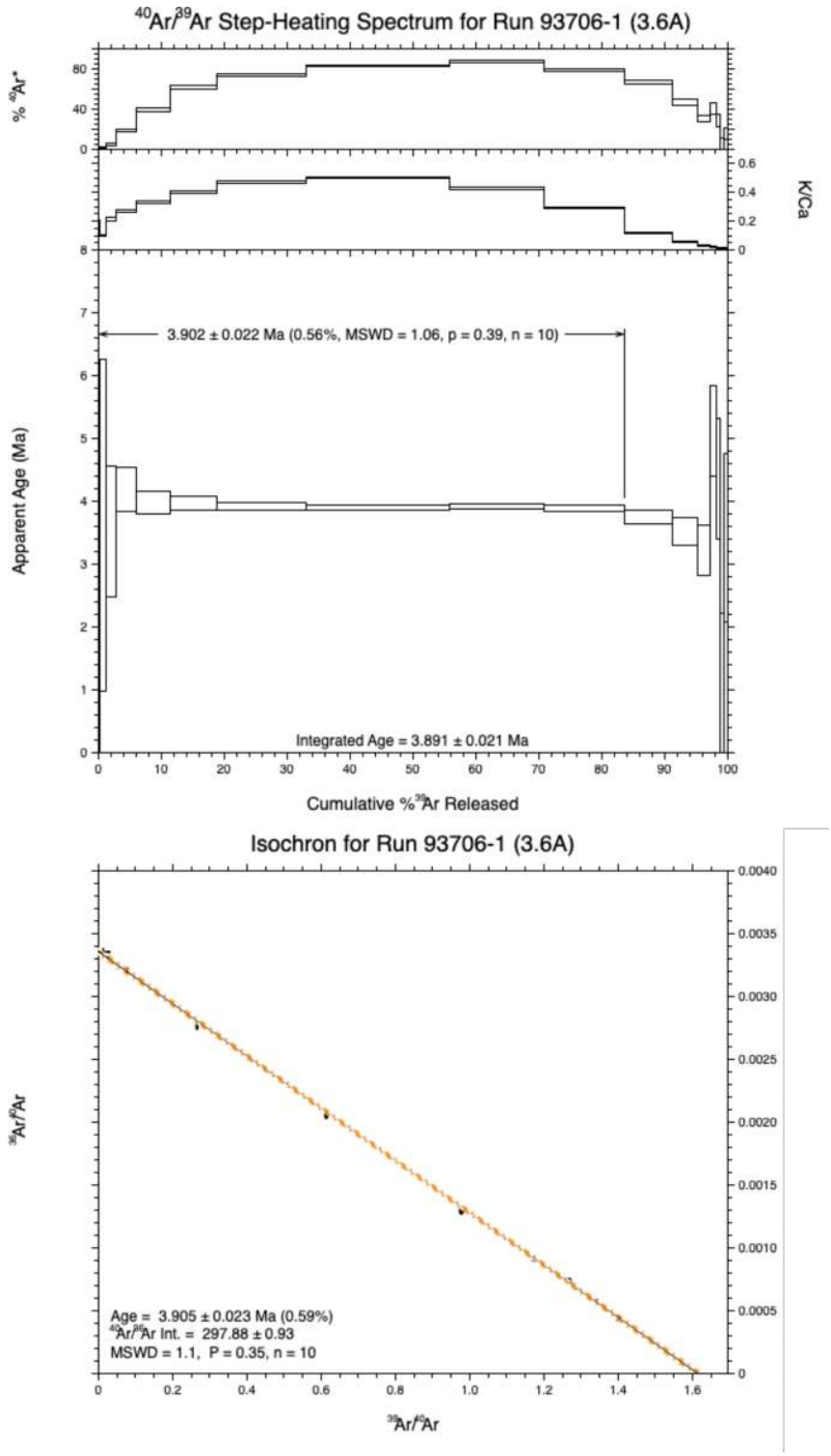

Figure 9: $^{40}Ar/^{39}Ar$ incremental heating analyses of Harrat Rahat sample 3.6A.

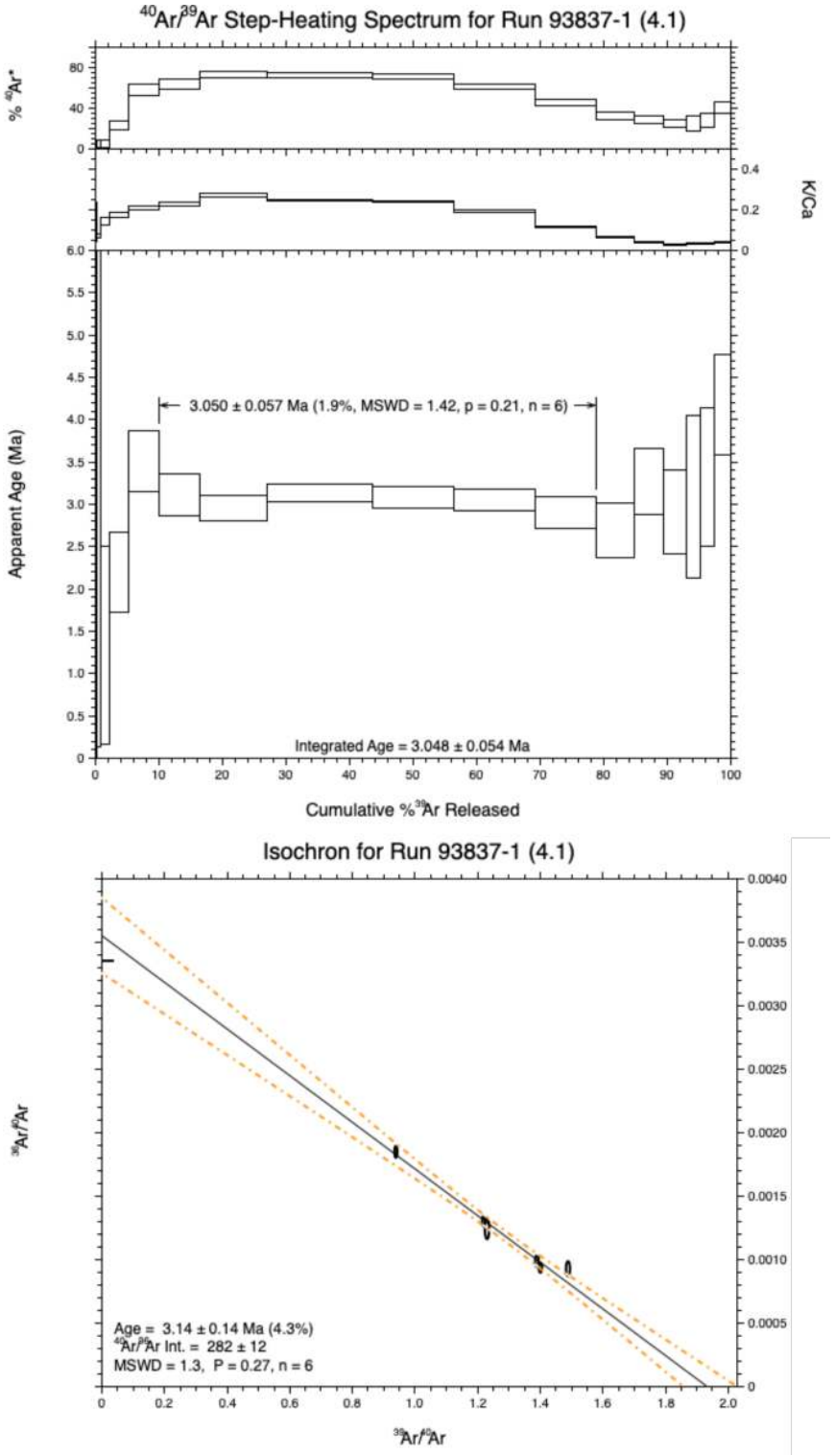

Figure 10: $^{40}Ar/^{39}Ar$ incremental heating analyses of Harrat Rahat sample 4.1.

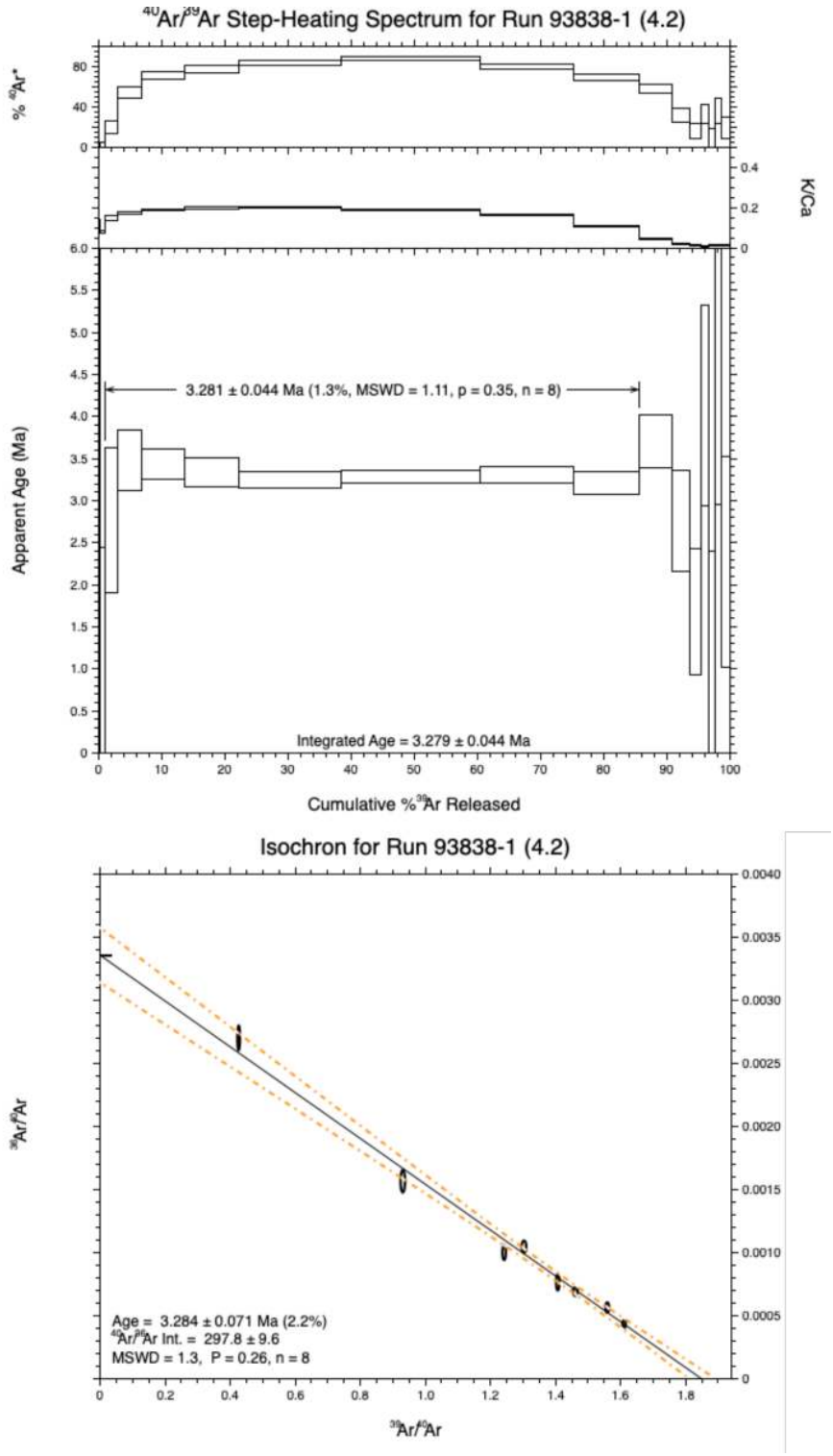

Figure 11: $^{40}Ar/^{39}Ar$ incremental heating analyses of Harrat Rahat sample 4.2.

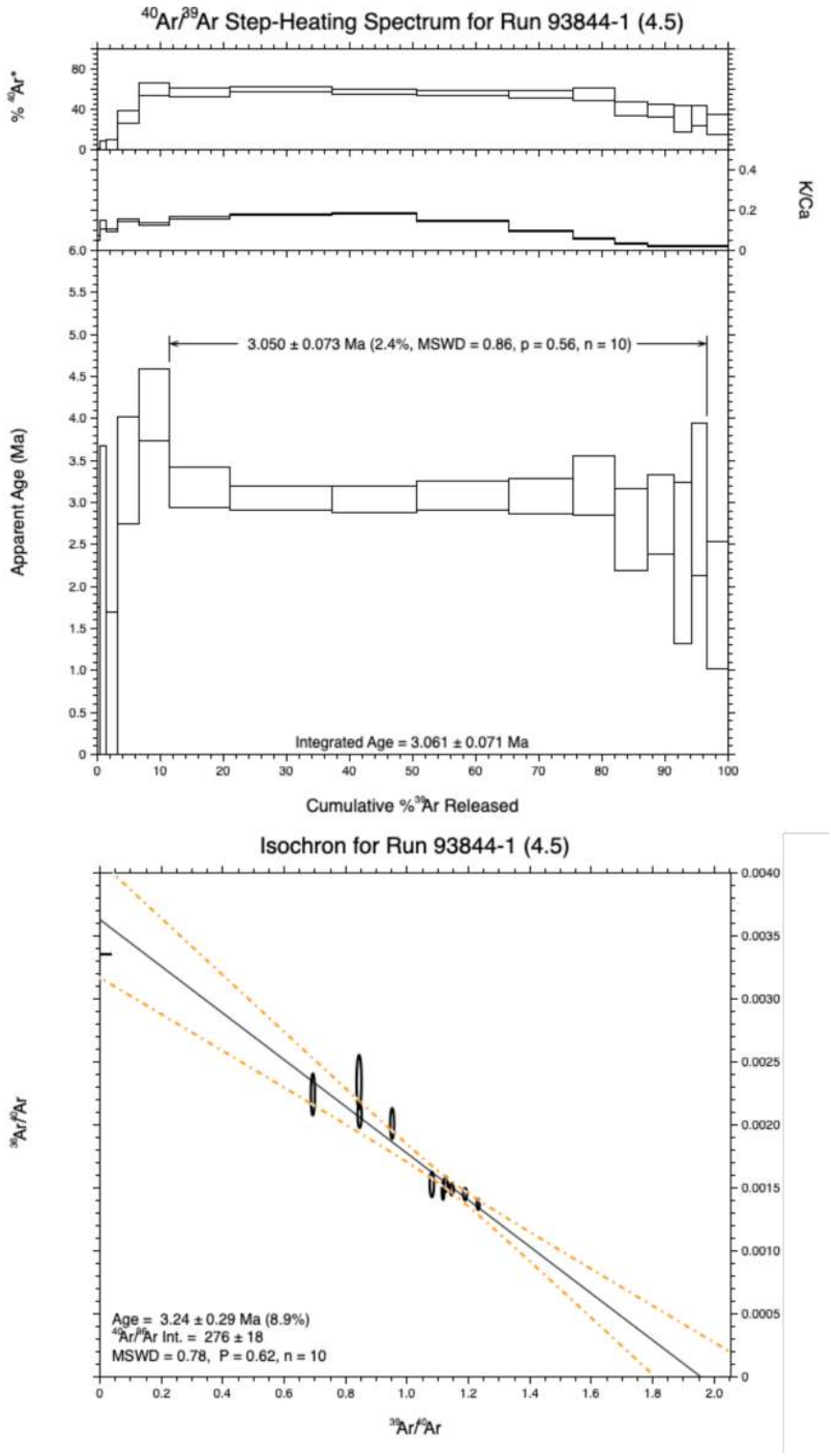

Figure 12: $^{40}Ar/^{39}Ar$ incremental heating analyses of Harrat Rahat sample 4.5.

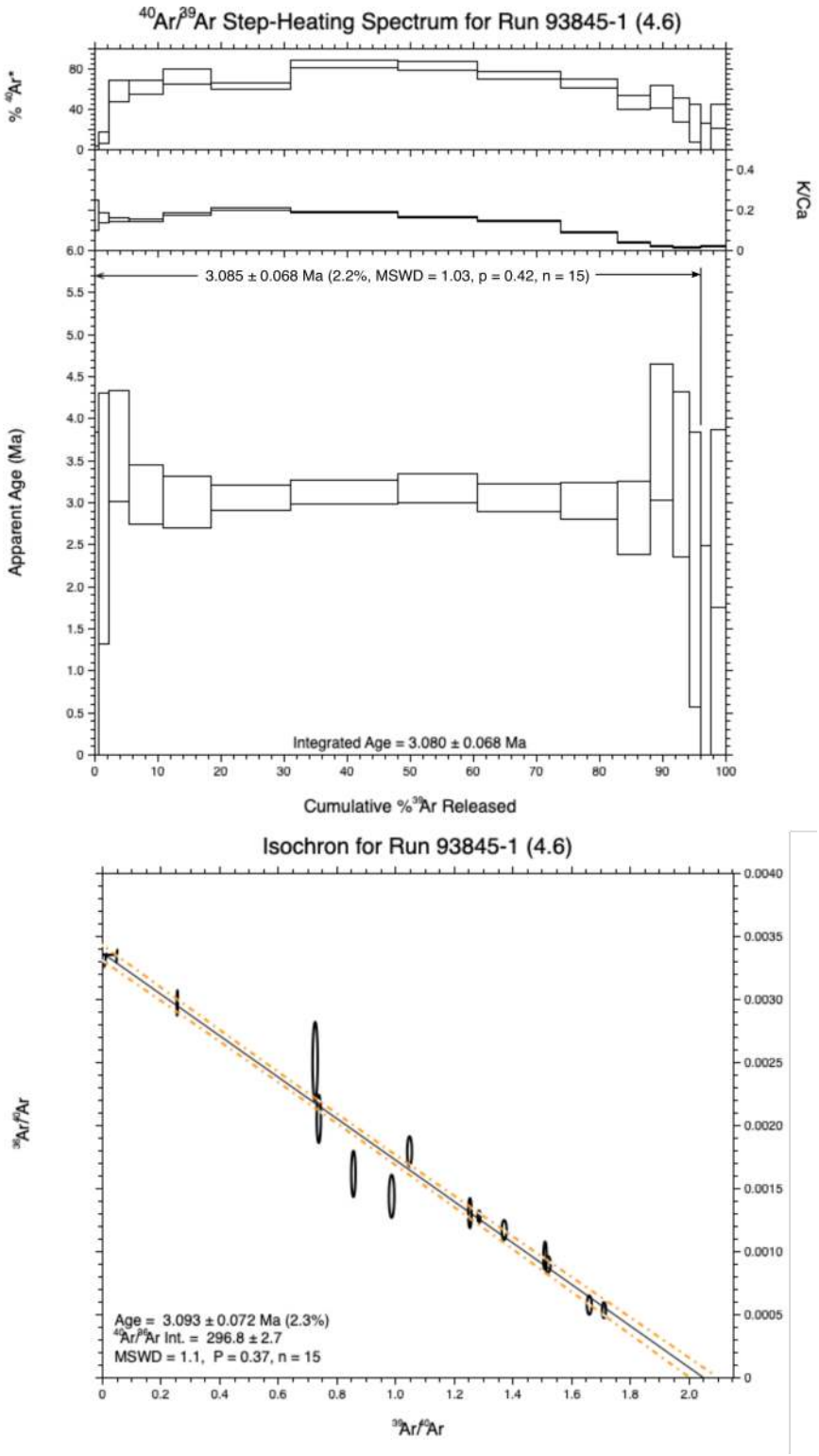

Figure 13: $^{40}Ar/^{39}Ar$ incremental heating analyses of Harrat Rahat sample 4.6.

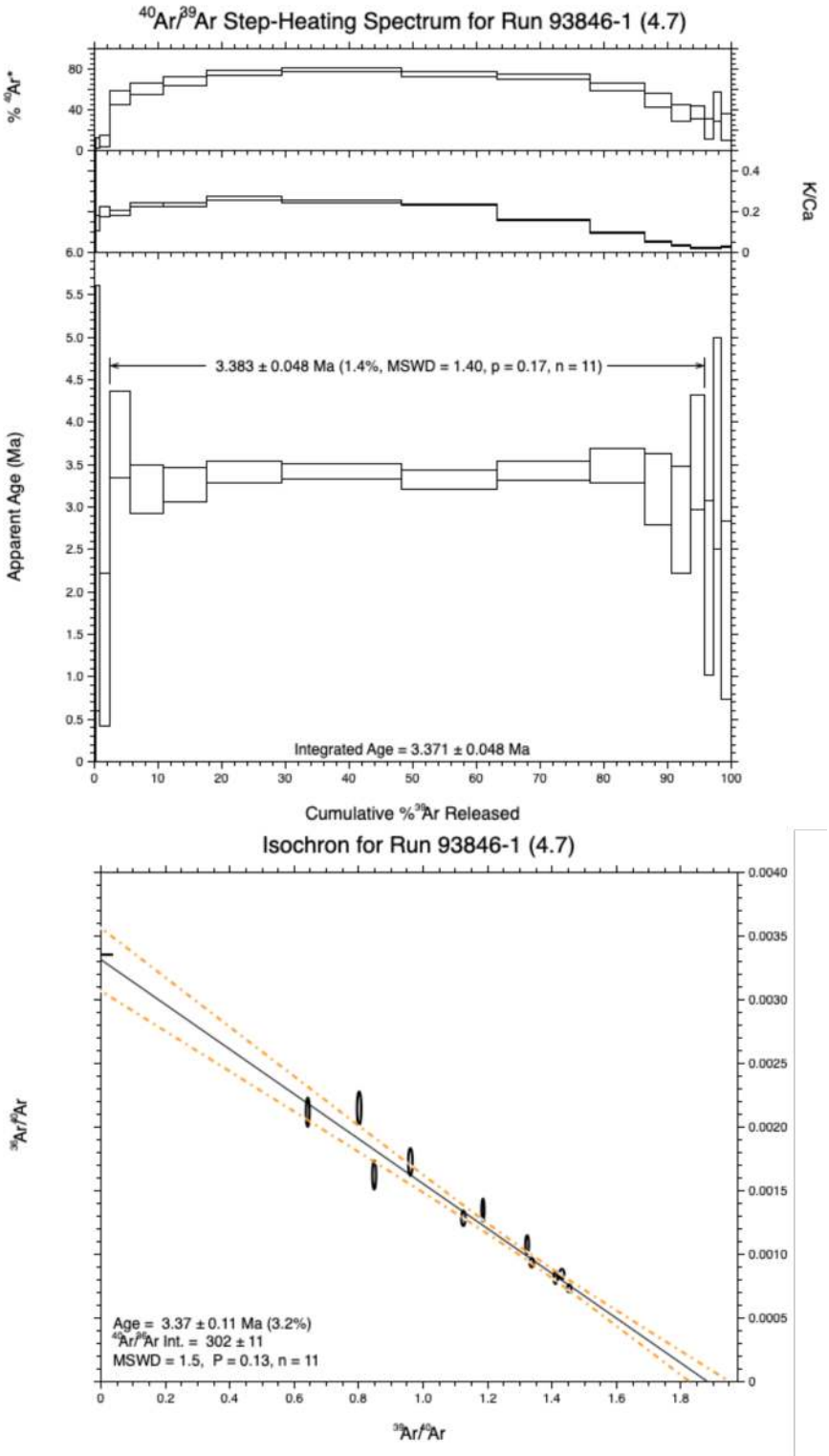

Figure 14: $^{40}Ar/^{39}Ar$ incremental heating analyses of Harrat Rahat sample 4.7.

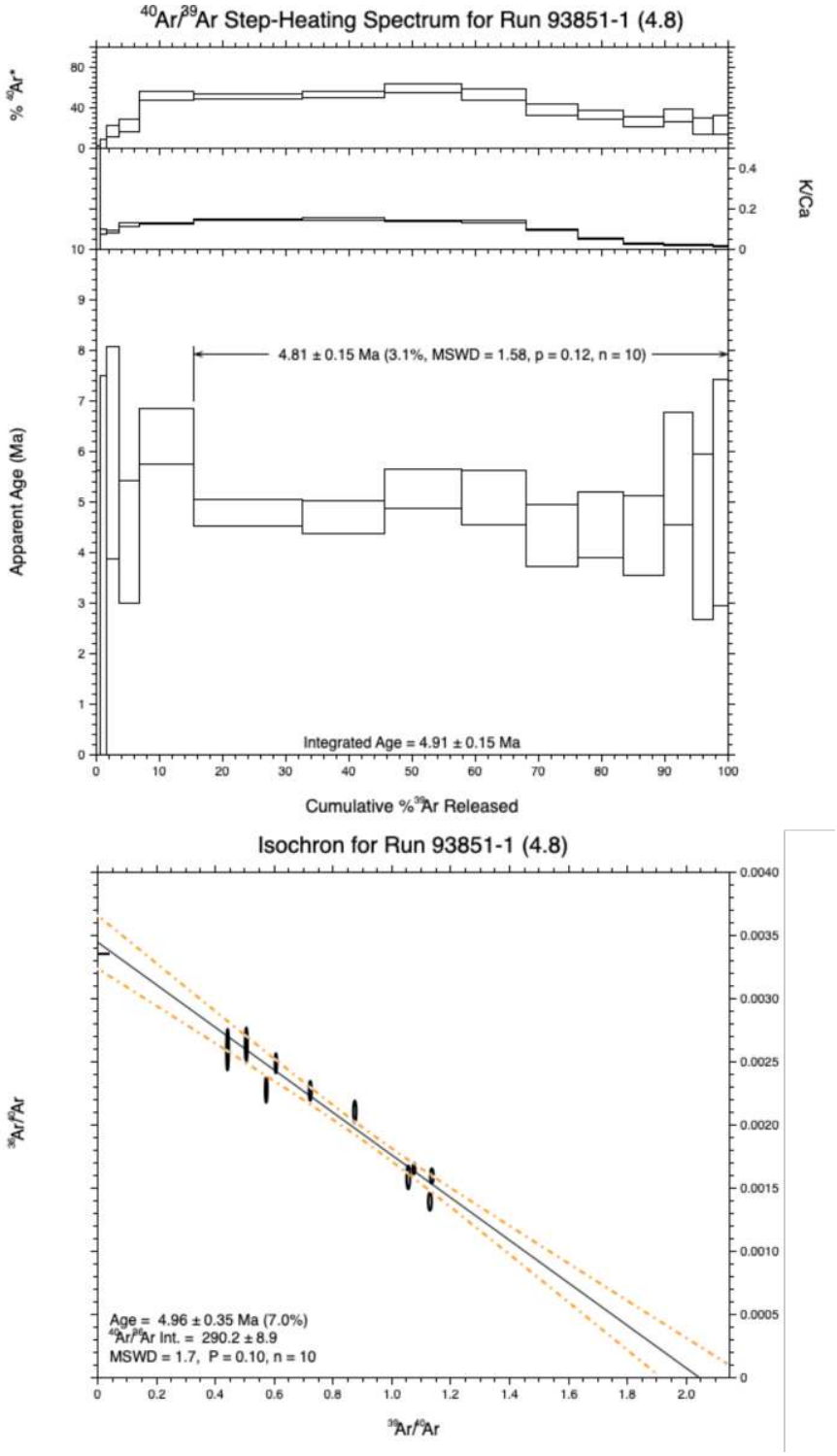

Figure 15: $^{40}Ar/^{39}Ar$ incremental heating analyses of Harrat Rahat sample 4.8.

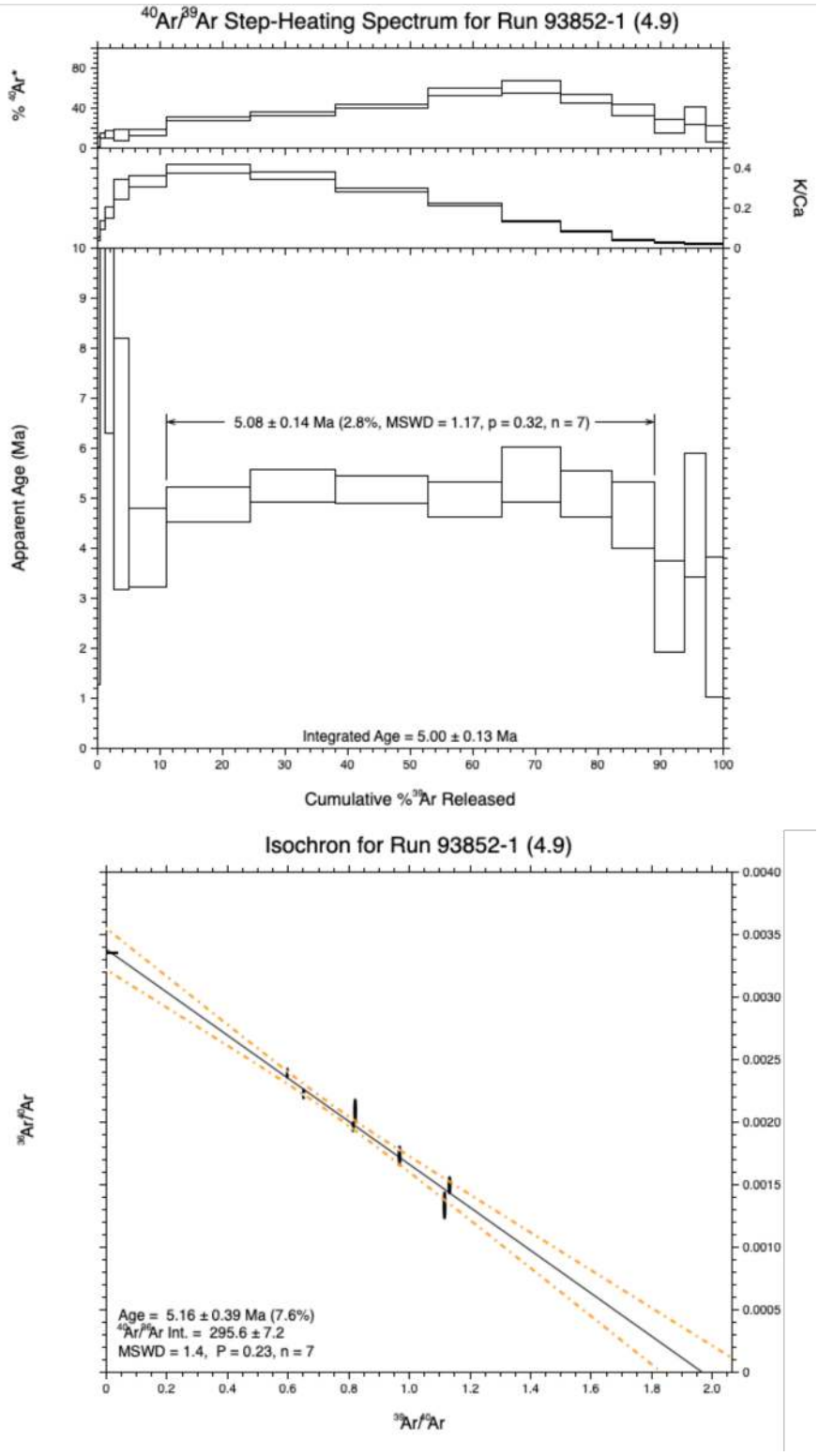

Figure 16: $^{40}Ar/^{39}Ar$ incremental heating analyses of Harrat Rahat sample 4.9.

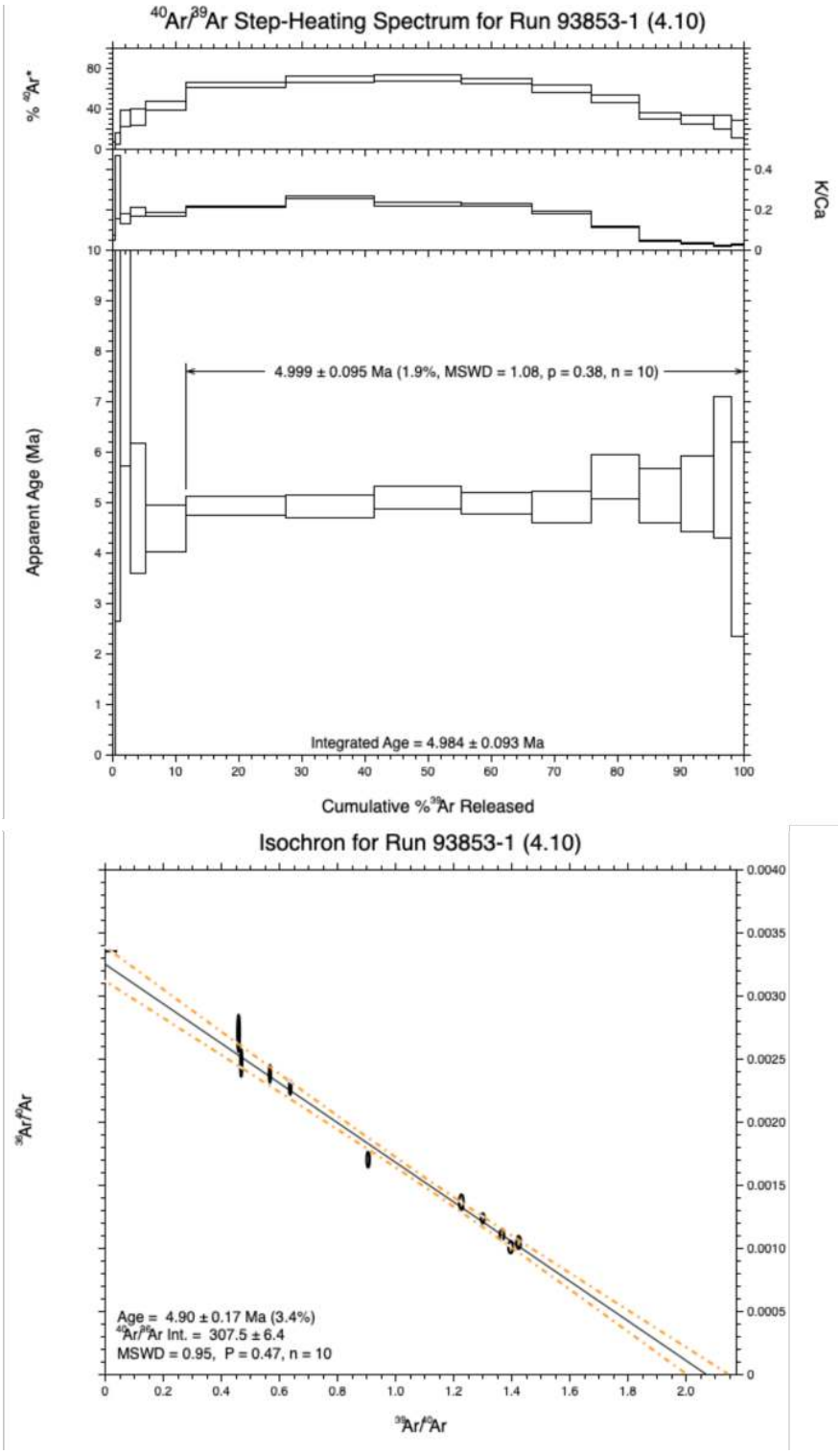

Figure 17: $^{40}Ar/^{39}Ar$ incremental heating analyses of Harrat Rahat sample 4.10.

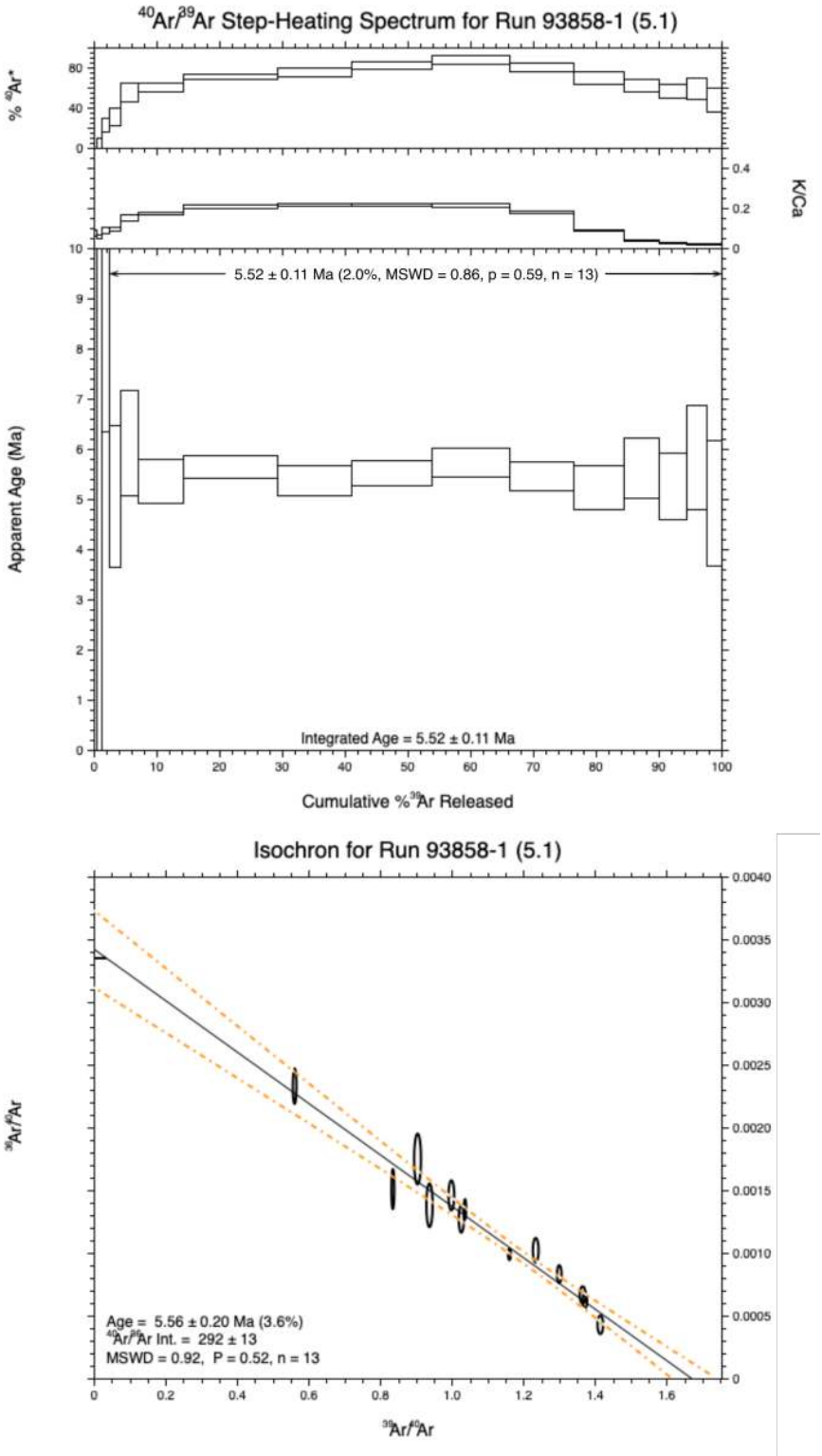

Figure 18: $^{40}Ar/^{39}Ar$ incremental heating analyses of Harrat Rahat sample 5.1.

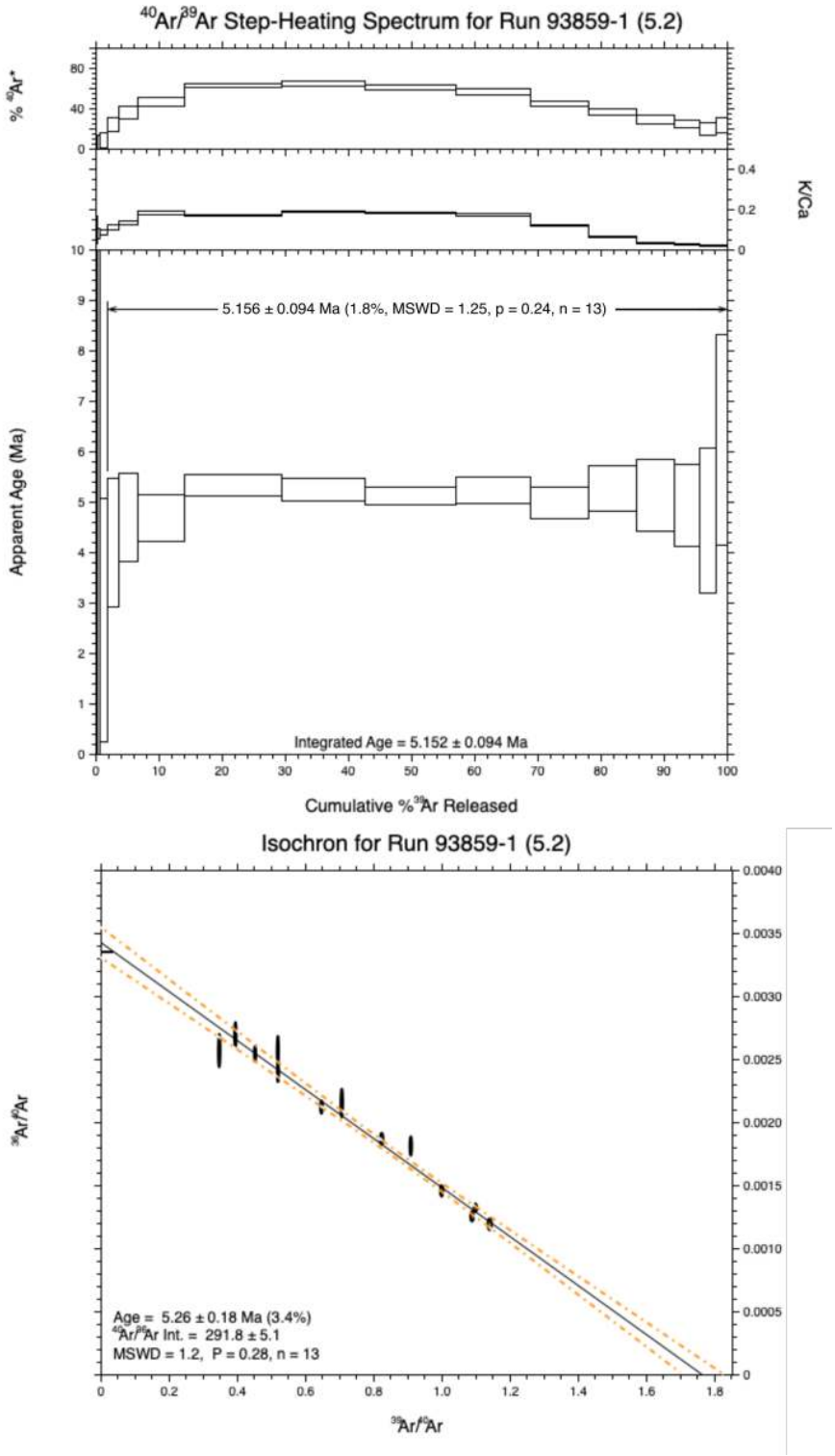

Figure 19: $^{40}Ar/^{39}Ar$ incremental heating analyses of Harrat Rahat sample 5.2.

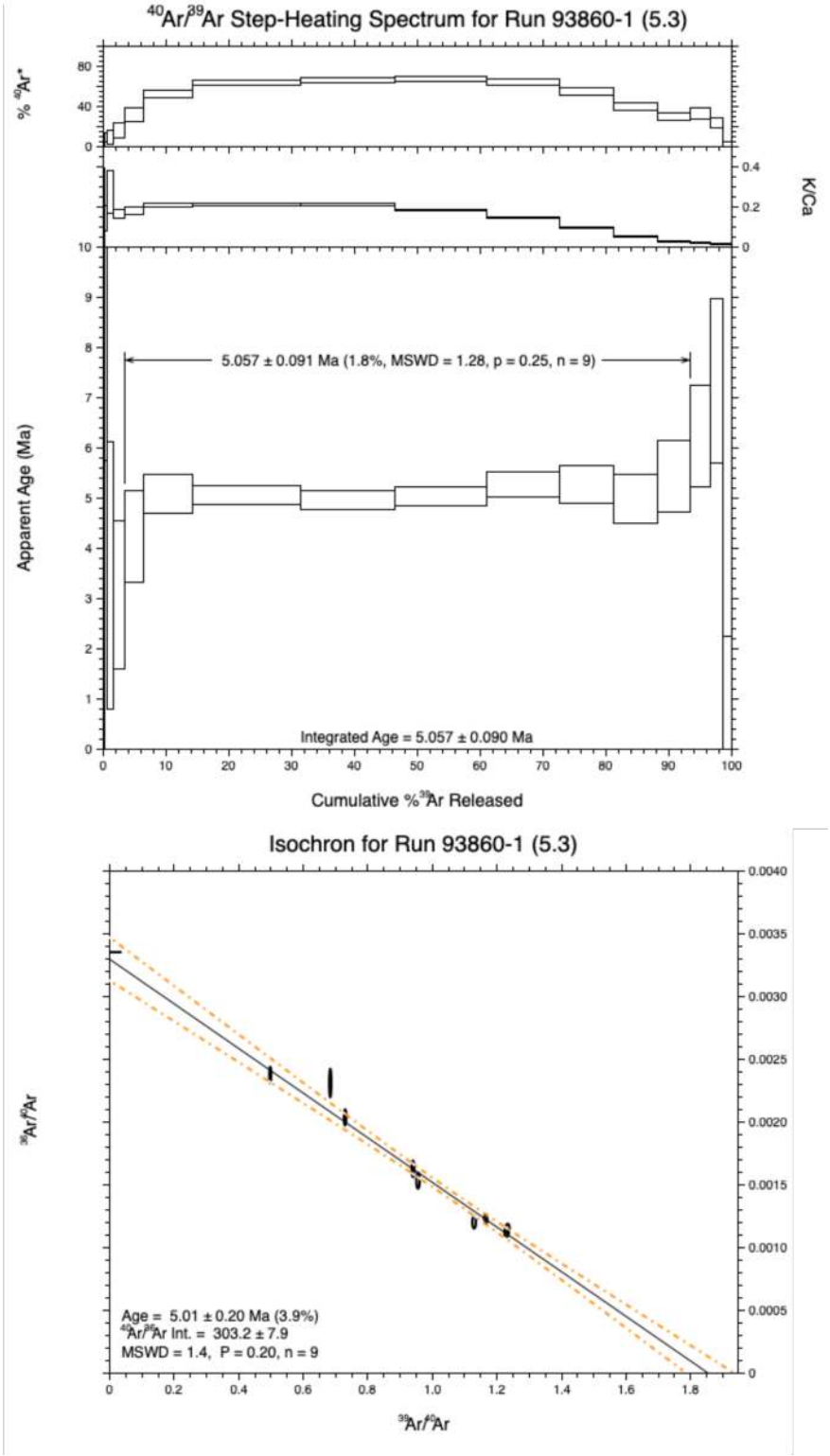

Figure 20: $^{40}Ar/^{39}Ar$ incremental heating analyses of Harrat Rahat sample 5.3.

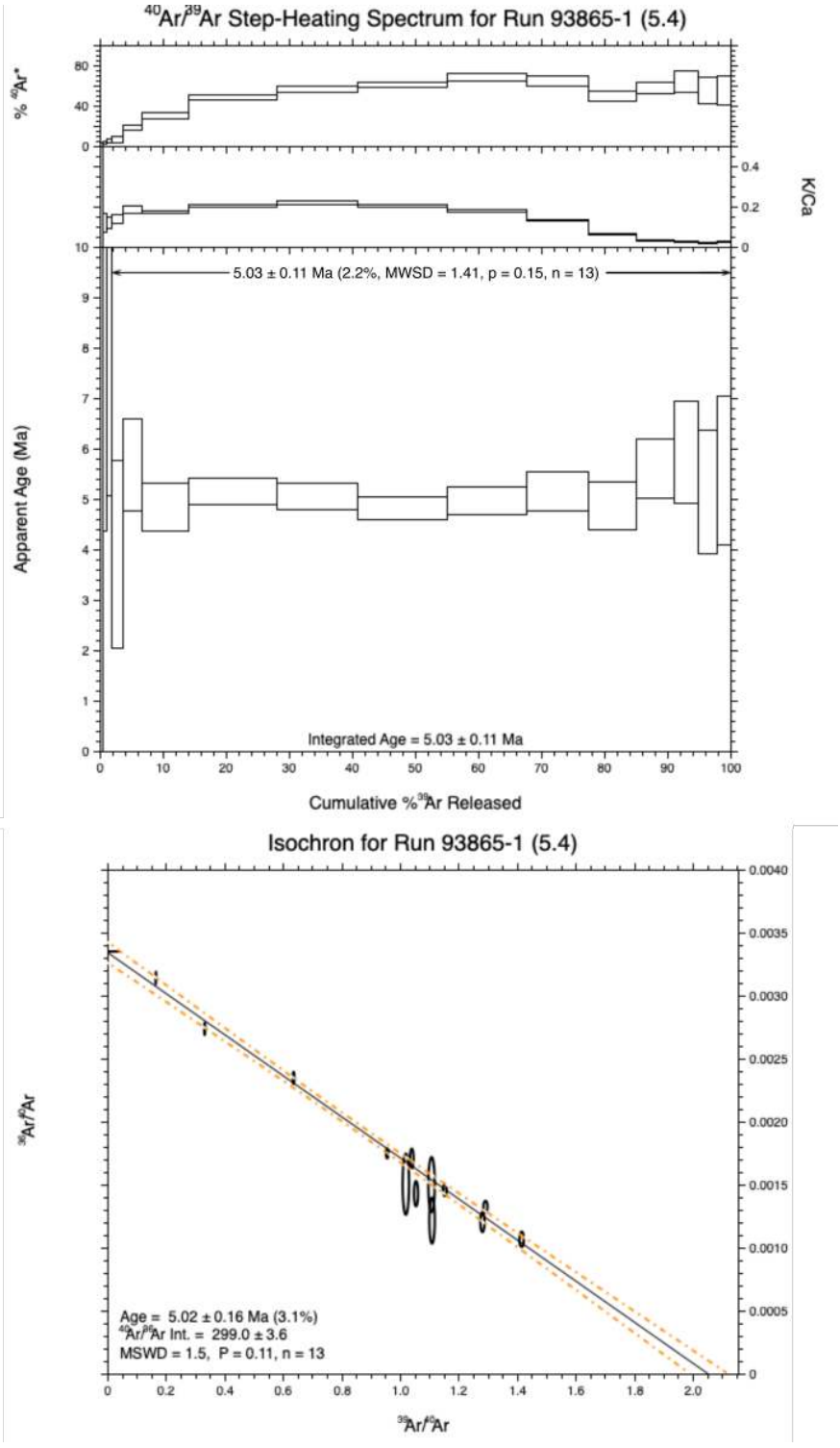

Figure 21: $^{40}Ar/^{39}Ar$ incremental heating analyses of Harrat Rahat sample 5.4.

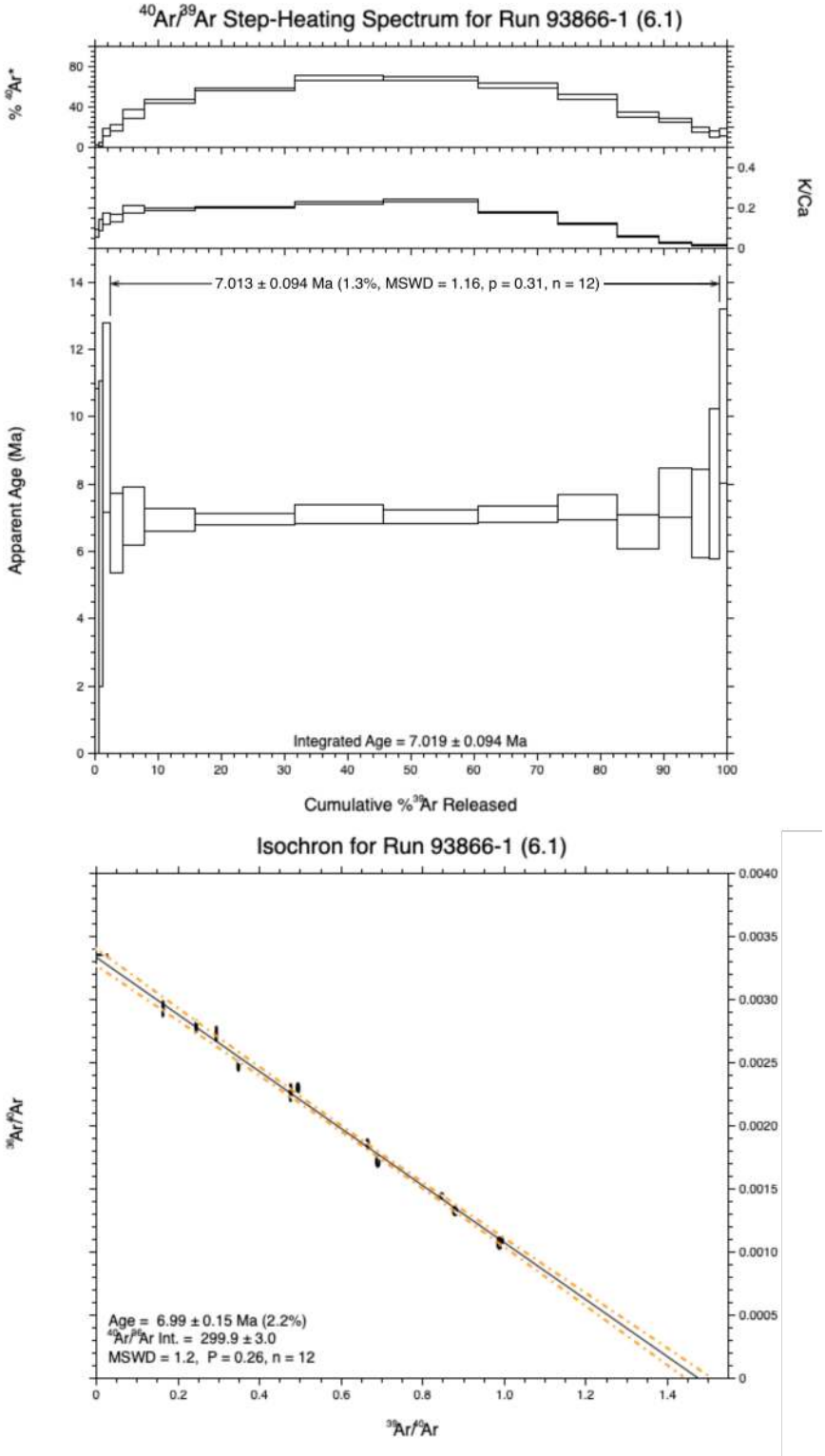

Figure 22: $^{40}Ar/^{39}Ar$ incremental heating analyses of Harrat Rahat sample 6.1.

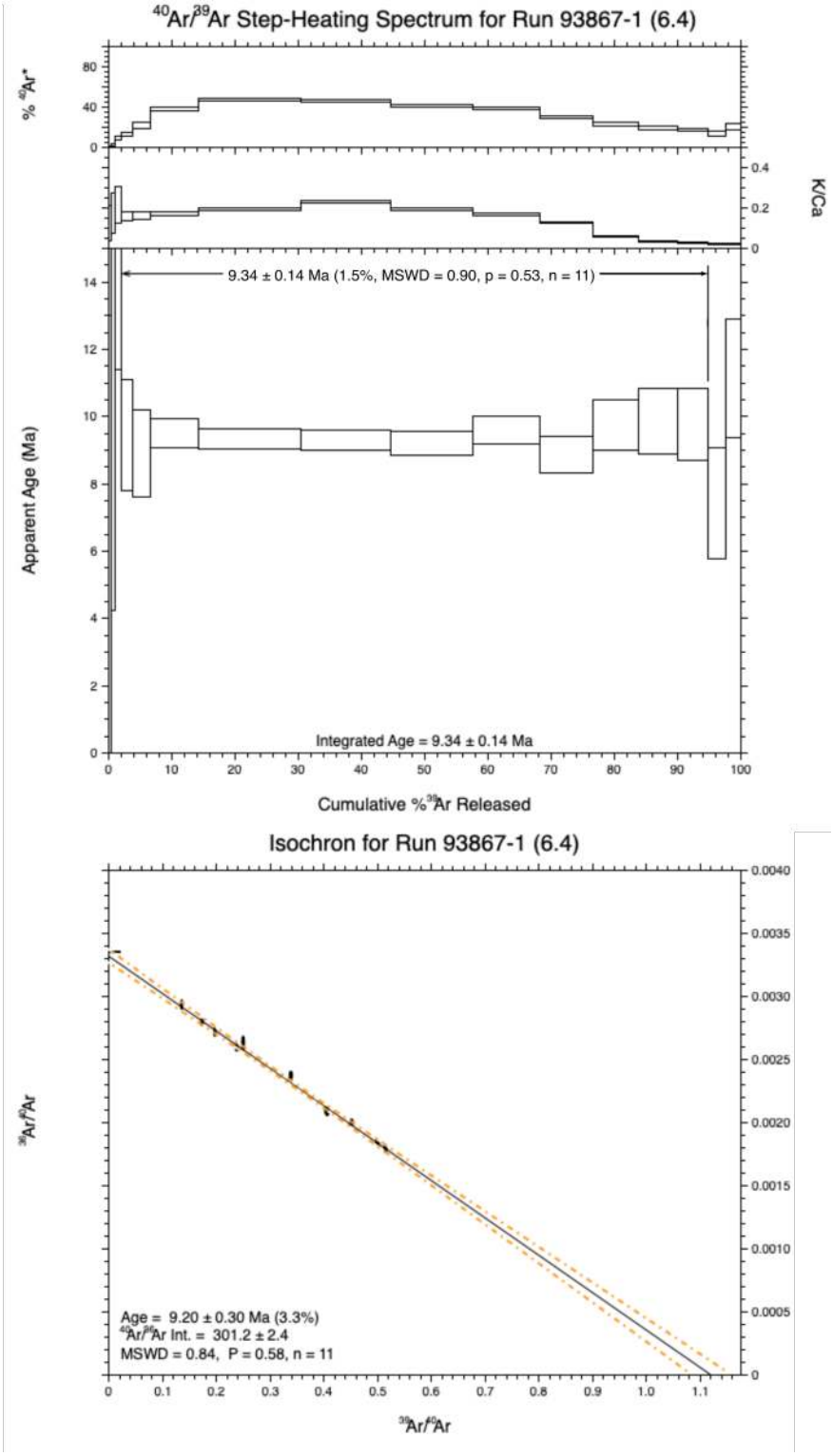

Figure 23: $^{40}Ar/^{39}Ar$ incremental heating analyses of Harrat Rahat sample 6.4.

3. Geochemical Analysis

These samples were analyzed alongside samples described in, and the method description is taken from, Ball et al. (2021).

3.1. Sample Preparation

Rock samples were cut up into small chunks and weathered surfaces removed with a diamond-tipped circular rock saw. Each piece of sample was washed with Millipore water and left to dry. A small stub was set aside from each sample to make thin-sections. A subsection of sample weighing ∼50–80 g was passed through a jaw crusher followed by an agate planetary ball mill (at 220 rpm for 12 minutes) to produce a talc-like powder. Both machines were thoroughly cleaned between each run.

3.2. X-ray Fluorescence (XRF) Analysis

Powdered samples were prepared for XRF analysis using the methodology outlined in Fitton et al. (1998). The samples were prepared and analysed in the University of Edinburgh in January 2017.

Samples were dried overnight in an oven at 110 °C before 1 g of each sample was placed in an oven at 1100 °C for one hour. Loss on ignition (LOI) is the mass difference in the powder before and after this process. Negative LOI values are commonly caused by oxidation of Fe while positive values are caused by the loss of volatiles. This ignited powder is then mixed with lithium tetraborate flux powder, heated to 1100 °C again and cast into glass discs. These glass discs are used to determine major and minor element abundances. Trace element concentrations are measured from press powder pellets. Pellets are formed from 6 g of sample and 5 drops of 2 % aqueous solution of polyvinyl alcohol. Elemental abundances were produced using a Philips PW 1480 automatic XRF spectrometer with a Rh-anode X-ray tube at the University of Edinburgh.

In each set of XRF analyses conducted at the University of Edinburgh, element accuracy and precision estimates were determined by analysis of standardised materials (Table 1) and repeat runs of individual samples (Table 2). The spectrometer was calibrated with BHVO-2, BIR-1, BCR-2 and BE-N standards using the values given by Govindaraju (1994). Major element standards are replicated to < 2.5 % with the exception of Na_2O and P_2O_5 (Table 1). Throughout this study the elemental abundances for Cr, Ni, Sc, Sr, V, Y, Zn and Zr are taken from XRF analysis. For these elements, the majority of standards are replicated to within $< 5\%$ of the literature value. Elements that vary from literature values by > 10 % are present in far lower quantities within the standard than within the analysed samples (e.g. Ni and Cr in BCR-2). Rocks from the same sample site were processed and analysed separately to assess the elemental variability associated with both the heterogeneity of samples and analytical error. Duplicate analyses have a variance, V, of $< 1\%$ in most cases (Table 2). Variance is defined as,

$$V = (\sigma/\bar{x}) \times 100, \tag{1}$$

where $\bar{x}$ and σ are the average and standard deviation of the data, respectively. Major and trace element abundances and LOI are shown in Table 1 of main text.

3.3. Inductively Coupled Plasma Mass Spectrometry (ICP-MS) Trace Element Analysis

Trace element abundances were produced using ICP-MS analysis. The samples were prepared for ICP-MS analysis at the Department of Earth Sciences, University of Cambridge. Approximately 1 g of each sample was dried in an oven to remove excess water and then left to cool in a desiccator. 0.1 ± 0.01 g of each sample was weighed out into individual clean Teflon vials. 1 ml of HNO_3 and 4 ml of HF was added to each sample, the vials were closed and then placed on a hotplate at 125 °C for 24 hours. The vials were then removed from the hotplate and screwed into Teflon Evapoclean elbows, put back into the hotplate and left until most of the acid had evaporated. 1 ml of HNO_3 was added to each sample and the evaporation process was repeated, this process was reproduced a second time. After this third period of evaporation, 2.5 ml of HNO_3 and 10 ml of Millipore water were added to each sample. The samples were removed from the

Evapoclean elbows and the Teflon vials were covered by lids before they were put back onto the hotplate for 24 hours at 125 °C. The samples were then poured into 60 ml LDPE bottles and diluted with Millipore water until each sample was 50 ml in volume (3.5 % HNO_3). The solutions were kept in a dark drawer until they were analysed, in each case less than a month later.

Samples were analysed on a PerkinElmer Nexion 350D ICP-MS in the Department of Earth Sciences, University of Cambridge in January 2018. The analytical method employed is an adaptation of Eggins et al. (1997). The diluted samples were analysed with a Micromist nebuliser (FM05, Glass Expansion, Australia) and a quartz cyclonic baffled spray chamber with platinum sampler and skimmer cones. In this configuration, ICP-MS sensitivity was 5×104 cps/ppb In with CeO/Ce ratios of 2%. Corrections from oxide to metal abundances were calculated by measuring pure single element standards (GeoReM database v9; `http:\georem.mpch-mainz.gwdg.de/`). Instrumental drift on the internal standards (10 ppb Rb, In and Re diluted 5×10^4 for analyses in 1% HNO_3) was $< 5\%$ measured for the internal standard intensity during the run with more than 40 solutions per batch. For each set of analyses conducted, internationally recognised USGS standards: BHVO-2, BCR-2, BIR-1 and BOB-1 (Table 1) were analysed as a form of quality control. Each of these samples was prepared in the same manner described above. Additionally, a sample containing 10 ppb Rh, In and Re in a 1 % HNO_3 solution was analysed between each run of 10 samples as a drift monitor. Raw intensities calculated during analysis are converted into elemental concentrations through blank subtraction, internal standard normalisation and rare earth oxide correction.

Standards are replicated to < 5 % in most cases with the exception of Be, Ga, Li, Rb, Sn (Table 1). Therefore, use of these elements should be treated with caution. Repeat analyses show a good agreement between samples with the majority of elements varying by $< 5\%$ (Table 4).

References

Altherr, R., Henjes-Kunst, F., Baumann, A., 1990. Asthenosphere versus lithosphere as possible sources for basaltic magmas erupted during formation of the Red Sea: constraints from Sr, Pb and Nd isotopes. Earth and Planetary Science Letters 96, 269–286.

Ball, P., Czarnota, K., White, N., Klöcking, M., Davies, D., 2021. Thermal structure of eastern Australia's upper mantle and its relationship to Cenozoic volcanic activity and dynamic topography. Geochemistry, Geophysics, Geosystems 22, e2021GC009717.

Bertrand, H., Chazot, G., Blichert-Toft, J., Thoral, S., 2003. Implications of widespread high-μ volcanism on the Arabian Plate for Afar mantle plume and lithosphere composition. Chemical Geology 198, 47–61.

Brown, G.E., Schmidt, D.L., Huffman Jr, A.C., 1989. Geology of the Arabian Peninsula; shield area of western Saudi Arabia. U.S – Geological Survey Professional Paper No. 560-A. United States Government Printing Office, Washington, U.S.A.

Camp, V.E., Roobol, M.J., 1989. The Arabian continental alkali basalt province: Part I. Evolution of Harrat Rahat, Kingdom of Saudi Arabia. Geological Society of America Bulletin 101, 71–95.

Downs, D., 2019. Major-and trace-element chemical analyses of rocks from the northern Harrat Rahat volcanic field and surrounding area, Kingdom of Saudi Arabia. US Geological Survey data release .

Downs, D.T., Stelten, M.E., Champion, D.E., Dietterich, H.R., Nawab, Z., Zahran, H., Hassan, K., Shawali, J., 2018. Volcanic history of the northernmost part of the Harrat Rahat volcanic field, Saudi Arabia. Geosphere 14, 1253–1282. doi:`10.1130/GES01625.1`.

Eggins, S., Woodhead, J., Kinsley, L., Mortimer, G., Sylvester, P., McCulloch, M., Hergt, J., Handler, M., 1997. A simple method for the precise determination of ≤ 40 trace elements in geological samples by ICPMS using enriched isotope internal standardisation. Chemical Geology 134, 311–326.

Fitton, J., Saunders, A., Larsen, L., Hardarson, B., Norry, M., 1998. Volcanic rocks from the southeast Greenland margin at 63°N: composition, petrogenesis and mantle sources. Proceedings of the Ocean Drilling Program, Scientific Results 152, 197–208.

Moufti, M.R., Moghazi, A.M., Ali, K.A., 2012. Geochemistry and Sr–Nd–Pb isotopic composition of the Harrat Al-Madinah Volcanic Field , Saudi Arabia. Gondwana Research 21, 670–689. URL: `http://dx.doi.org/10.1016/j.gr.2011.06.003`, doi:`10.1016/j.gr.2011.06.003`.

Moufti, M.R., Moghazi, A.M., Ali, K.A., 2013. $^{40}Ar/^{39}Ar$ geochronology of the Neogene-Quaternary Harrat Al-Madinah intercontinental volcanic field, Saudi Arabia: Implications for duration and migration of volcanic activity. Journal of Asian Earth Sciences 62, 253–268. URL: `http://dx.doi.org/10.1016/j.jseaes.2012.09.027`, doi:`10.1016/j.jseaes.2012.09.027`.

Murcia, H., Lindsay, J.M., Németh, K., Smith, I.E.M., Cronin, S.J., Moufti, M.R.H., El-Masry, N.N., Niedermann, S., 2017. Geology and geochemistry of Late Quaternary volcanism in northern Harrat Rahat, Kingdom of Saudi Arabia: implications

for eruption dynamics, regional stratigraphy and magma evolution, in: Monogenetic Volcanism. The Geological Society of London, pp. 173–204. URL: https://doi.org/10.1144/SP446.2, doi:10.1144/SP446.2.

Murcia, H., Németh, K., El-Masry, N., Lindsay, J., Moufti, M., Wameyo, P., Cronin, S., Smith, I., Kereszturi, G., 2015. The Al-Du'aythah volcanic cones, Al-Madinah City: implications for volcanic hazards in northern Harrat Rahat, Kingdom of Saudi Arabia. Bulletin of Volcanology 77, 54.

Stelten, M.E., Downs, D.T., Dietterich, H.R., Mahood, G.A., Calvert, A.T., Sisson, T.W., Zahran, H., Shawali, J., 2018. Timescales of magmatic differentiation from alkali basalt to trachyte within the Harrat Rahat volcanic field, Kingdom of Saudi Arabia. Contributions to Mineralogy and Petrology 173, 1–17.

4. Data Tables

Table 1: XRF Standards Analysed. $\bar{x}$ = average of n number of runs; σ = standard deviation; accuracy, $S = (\bar{x}/E) \times 100$ where E = reference value.

Element (wt%)	SiO_2	TiO_2	Al_2O_3	Fe_2O_3	MnO	MgO	CaO	Na_2O	K_2O	P_2O_5
BHVO-1	49.94	2.710	13.80	12.23	0.168	7.23	11.40	2.26	0.520	0.273
Average (n=3)	49.61	2.724	13.50	12.25	0.168	7.14	11.36	2.07	0.512	0.266
σ	0.1	0.002	0.03	0.00	0.002	0.03	0.00	0.03	0.002	0.002
S	99.34	100.50	97.80	100.19	100.20	98.80	99.65	91.59	98.46	97.56
BIR-1	47.77	0.96	15.35	11.26	0.171	9.68	13.24	1.75	0.027	0.046
Average (n=3)	47.72	0.951	15.48	11.46	0.173	9.61	13.37	1.45	0.024	0.033
σ	0.04	0.003	0.04	0.02	0.003	0.04	0.01	0.11	0.001	0.000
S	99.89	99.06	100.83	101.78	101.36	99.28	100.98	82.86	90.12	71.01

Element (ppm)	Sr	U	Rb	Th	Pb	Nb	Zr	Y
BCR	330.0	1.8	47.2	6.0	13.6	14.0	190.0	38.0
Average (n=3)	328.1	1.7	47.5	6.0	14.3	12.7	192.9	37.9
σ	1.0	0.4	0.3	0.1	0.2	0.0	0.7	0.1
S	99.42	97.14	100.64	100.33	104.90	90.71	101.53	99.65
BEN	1370.0	2.4	47.0	10.4	4.0	105.0	260.0	30.0
Average (n=3)	1389.0	2.3	47.9	10.7	3.5	116.6	267.8	29.7
σ	2.0	0.0	0.2	0.3	0.2	0.1	0.6	0.1
S	101.39	95.83	101.84	103.21	86.67	111.05	103.00	99.00
BHVO	403.0	0.4	11.0	1.1	2.6	19.0	179.0	27.6
Average (n=3)	384.4	0.3	9.9	0.9	2.3	19.3	175.3	27.0
σ	0.4	0.2	0.1	0.0	0.1	0.1	0.5	0.0
S	95.38	63.49	89.70	86.42	89.74	101.75	97.95	97.95
BIR	108.0	0.0	0.3	-	3.0	0.6	15.5	16.0
Average (n=3)	107.3	0.1	0.3	-	2.5	0.9	16.3	16.5
σ	0.3	0.2	0.3	-	0.2	0.1	0.2	0.1
S	99.35	666.67	120.00	-	83.33	150.00	105.38	103.13

	Zn	Cu	Ni	Cr	V	Ba	Sc	La	Ce	Nd
BCR	129.5	19.0	13.0	16.0	407.0	681.0	32.6	24.9	53.7	28.8
Average (n=3)	124.5	17.8	11.0	6.7	399.2	698.9	31.6	23.1	52.6	28.1
σ	0.1	0.7	0.7	0.9	4.0	3.3	0.8	0.5	0.4	0.1
S	96.11	93.51	84.62	41.67	98.08	102.62	96.93	92.64	98.01	97.45
BEN	120.0	72.0	267.0	360.0	235.0	1025.0	22.0	82.0	152.0	67.0
Average (n=3)	125.8	71.0	271.6	377.6	246.7	1059.8	24.1	88.6	156.2	69.3
σ	1.1	0.3	1.2	0.8	1.7	6.9	0.7	0.3	2.1	1.8
S	104.81	98.56	101.71	104.88	104.96	103.40	109.39	108.09	102.79	103.38
BHVO	105.0	136.0	121.0	289.0	317.0	139.0	31.8	15.8	39.0	25.2
Average (n=3)	104.6	132.8	112.9	284.1	313.0	134.2	32.7	10.3	38.1	26.0
σ	0.8	1.9	1.4	9.5	3.0	5.5	0.5	0.5	0.5	0.8
S	99.62	97.65	93.28	98.32	98.75	96.57	102.73	64.98	97.78	103.17
BIR	71.0	126.0	166.0	382.0	313.0	7.0	44.0	0.6	2.0	2.5
Average (n=3)	66.5	127.6	151.9	376.7	312.3	5.9	39.6	-	3.4	2.0
σ	1.1	0.4	0.7	10.3	1.9	0.7	0.6	-	1.3	0.8
S	93.66	101.24	91.49	98.60	99.79	84.29	90.00	-	176.07	78.67

Table 2: XRF repeats of Conducted alongside Arabian samples. Repeated samples from Ball et al. (2021). $\bar{x}$ = average of n runs; σ = standard deviation; variance, $V = (\sigma/\bar{x}) \times 100$.

Sample	SiO_2 (%)	Al_2O_3	Fe_2O_3	MgO	CaO	Na_2O	K_2O	TiO_2	MnO	P_2O_5
Q3.15 $\bar{x}$ (n=2)	45.05	14.86	12.16	7.74	7.81	5.74	3.19	2.02	0.18	1.25
σ	0.09	0.02	0.03	0.03	0.01	0.06	0.00	0.00	0.00	0.00
V	0.20	0.13	0.29	0.41	0.14	1.02	0.10	0.13	0.99	0.14
Q4.1 $\bar{x}$ (n=2)	44.55	14.45	12.81	8.23	8.40	5.11	2.74	2.31	0.18	1.22
σ	0.14	0.02	0.07	0.01	0.01	0.07	0.01	0.00	0.00	0.00
V	0.31	0.16	0.58	0.07	0.10	1.41	0.43	0.03	0.66	0.22
Q4.7 $\bar{x}$ (n=2)	48.12	14.86	11.34	8.87	8.18	3.80	2.01	2.09	0.15	0.57
σ	0.01	0.02	0.01	0.03	0.01	0.01	0.00	0.01	0.00	0.00
V	0.02	0.11	0.13	0.30	0.10	0.38	0.08	0.35	1.42	0.43

	Zn	Cu	Ni	Cr	V	Ba	Sc	La	Ce	Nd
Q7.9 $\bar{x}$ (n=3)	86.50	47.17	160.33	197.17	137.77	165.63	17.87	10.03	27.57	15.00
σ	0.61	0.68	8.29	21.98	1.18	1.06	0.47	0.32	1.31	0.62
V	0.70	1.44	5.17	11.15	0.86	0.64	2.65	3.20	4.73	4.16

	U	Th	Pb	Nb	Zr	Y	Sr	Rb
Q7.9 $\bar{x}$ (n=3)	0.47	1.73	2.10	20.20	119.93	20.00	496.43	14.47
σ	0.23	0.31	0.17	0.10	0.60	0.20	0.45	0.21
V	49.49	17.63	8.25	0.50	0.50	1.00	0.09	1.44

Table 3: ICP-MS standards analysed alongside samples. $\bar{x}$ = average of n number of runs; σ = standard deviation; accuracy, $S = (\bar{x}/E) \times 100$ where E = reference value.

	Li	Be	P	K	Sc	Ti	V	Cr	Mn	Co	Ni	Cu
BHVO-2	4.8	1	1178	4280	32	16367	317	280	1290	45	119	127
$\bar{x}$ (n=3)	4.82	0.97	1185.70	4428.88	38.35	16595.77	320.28	262.16	1246.40	40.52	110.29	128.03
σ	0.25	0.07	93.68	378.20	1.61	967.54	19.58	9.36	78.70	2.27	4.12	3.64
S	100.38	97.11	100.65	103.48	119.84	101.40	101.03	93.63	96.62	90.04	92.68	100.81
BCR-2	9	1.75	1527	14860	33	13549	416	18	1520	37	17.7	21
$\bar{x}$ (n=2)	9.55	2.09	1495.64	14144.44	41.43	13633.84	409.71	13.59	1447.11	33.29	11.22	25.58
σ	0.09	0.03	27.10	280.69	0.05	176.04	0.70	0.12	1.49	0.35	0.09	0.32
S	106.16	119.35	97.95	95.18	125.55	100.63	98.49	75.52	95.20	89.96	63.38	121.83
BIR-1	3.2	0.12	92	230	43	5755	313	382	1355	51	166	126
$\bar{x}$ (n=1)	3.44	0.10	48.05	205.36	53.00	5442.02	336.69	373.88	1356.06	50.16	151.75	116.97
S	93.04	124.42	191.46	112.00	81.13	105.75	92.96	102.17	99.92	101.67	109.39	107.72
BOB-1	7.9	0.6	850	3420	33.3	7488	229	264	1087	53	110	60
$\bar{x}$ (n=1)	9.50	0.55	733.87	3193.04	41.83	7990.85	245.99	244.50	1050.10	50.66	98.26	59.06
S	83.14	109.25	115.82	107.11	79.60	93.71	93.09	107.98	103.51	104.62	111.94	101.59

	Zn	Ga	Rb	Sr	Y	Zr	Nb	Sn	Cs	Ba	La	Ce
BHVO-2	103	21.7	9.08	396	26	172	18.1	1.7	0.09	131	15.2	37.5
$\bar{x}$ (n=3)	103.15	19.69	10.08	350.33	27.26	154.84	16.98	1.74	0.09	128.17	15.11	36.46
σ	5.36	1.28	0.58	21.98	2.34	15.66	1.11	0.13	0.01	6.18	0.99	2.25
S	100.15	90.73	110.98	88.47	104.84	90.02	93.79	102.29	102.16	97.84	99.42	97.22
BCR-2	127	20.6	46.9	340	37	188	12.6	2	1.07	677	24.9	52.9
$\bar{x}$ (n=2)	116.42	19.93	49.90	283.11	36.94	166.56	11.27	2.02	1.07	636.85	23.85	49.45
σ	3.25	0.27	0.94	2.71	0.05	1.30	0.04	0.13	0.04	33.64	1.10	2.42
S	91.67	96.73	106.40	83.27	99.85	88.60	89.44	100.92	100.29	94.07	95.79	93.48
BIR-1	71	16	0.24	110	16.5	14.5	0.55	0.6	0.007	7.14	0.615	1.92
$\bar{x}$ (n=1)	61.86	13.79	0.21	92.11	15.80	13.37	0.51	0.70	0.00	6.29	0.61	1.85
S	114.77	116.06	114.25	119.42	104.45	108.48	108.48	86.11	147.45	113.49	101.62	103.68
BOB-1	60	16	5.5	198	26	95	4.6	1	0.13	35.9	4.94	13.36
$\bar{x}$ (n=1)	58.37	14.34	5.99	175.35	28.44	94.15	4.28	0.90	0.13	34.07	4.90	13.09
S	102.80	111.61	91.78	112.92	91.42	100.90	107.35	110.71	98.65	105.37	100.84	102.07

	Pr	Nd	Sm	Eu	Gd	Tb	Dy	Ho	Er	Tm	Yb	Lu
BHVO-2	5.29	24.5	6.07	2.07	6.24	0.936	5.31	0.972	2.54	0.33	2	0.274
$\bar{x}$ (n=3)	5.24	24.48	6.11	2.08	6.36	0.95	5.42	1.00	2.56	0.35	2.01	0.28
σ	0.38	1.66	0.46	0.13	0.47	0.07	0.38	0.06	0.16	0.02	0.13	0.02
S	99.03	99.93	100.63	100.69	102.00	101.96	102.01	103.35	100.81	104.71	100.55	102.93
BCR-2	6.57	28.7	6.58	1.96	6.75	1.07	6.41	1.3	3.66	0.54	3.38	0.503
$\bar{x}$ (n=2)	6.41	27.45	6.39	1.86	6.51	1.05	6.35	1.27	3.55	0.52	3.29	0.49
σ	0.26	1.45	0.31	0.07	0.23	0.06	0.26	0.05	0.16	0.01	0.16	0.02
S	97.56	95.65	97.16	95.11	96.48	97.98	99.06	98.01	96.86	96.79	97.44	96.87
BIR-1	0.37	2.38	1.12	0.52	1.87	0.36	2.51	0.56	1.66	0.25	1.65	0.25
$\bar{x}$ (n=1)	0.37	2.35	1.09	0.53	1.91	0.38	2.66	0.59	1.74	0.26	1.69	0.26
S	99.51	101.22	102.66	97.49	97.68	95.35	94.20	95.15	95.41	94.39	97.51	96.18
BOB-1	2.05	10.46	3.12	1.17	4	0.69	4.5	0.96	2.7	0.4	2.55	0.38
$\bar{x}$ (n=1)	2.03	10.30	3.22	1.21	4.26	0.74	4.68	1.00	2.81	0.42	2.63	0.40
S	101.20	101.51	96.82	96.81	93.93	93.88	96.07	95.89	96.12	95.50	96.84	95.99

	Hf	Ta	Tl	Pb	Th	U
BHVO-2	4.36	1.14	0.022	1.6	1.22	0.39
$\bar{x}$ (n=3)	4.41	1.16	0.02	2.01	1.22	0.42
σ	0.30	0.08	0.00	0.71	0.07	0.03
S	101.15	101.92	86.27	125.44	99.61	107.80
BCR-2	4.9	0.74	0.26	11	5.7	1.69
$\bar{x}$ (n=2)	4.70	0.74	0.24	9.89	5.65	1.63
σ	0.21	0.03	0.01	0.50	0.27	0.08
S	95.96	99.33	93.32	89.92	99.05	96.50
BIR-1	0.582	0.0357	0.005	3.1	0.032	0.01
$\bar{x}$ (n=1)	0.59	0.04	0.00	3.07	0.07	0.01
S	97.93	84.87	395.81	100.92	46.18	97.21
BOB-1	2.34	0.47	0.054	0.84	0.36	0.13
$\bar{x}$ (n=1)	2.48	0.46	0.05	0.93	0.36	0.14
S	94.40	101.10	106.95	90.58	99.00	89.66

Table 4: ICP-MS repeat of Sample A3.1. $\bar{x}$ = average of 2 runs; σ = standard deviation; variance, $V = (\sigma/\bar{x}) \times 100$.

	Li	Be	P	K	Sc	Ti	V	Cr	Mn	Co	Ni	Cu
A3.1 $\bar{x}$	6.09	0.75	1051.51	4592.86	34.95	9454.23	250.23	341.38	1294.78	48.03	181.18	91.28
σ	0.10	0.02	124.60	76.28	1.86	677.32	19.02	9.81	84.35	1.53	2.40	2.06
V	1.64	2.37	11.85	1.66	5.33	7.16	7.60	2.87	6.51	3.19	1.32	2.25

	Zn	Ga	Rb	Sr	Y	Zr	Nb	Sn	Cs	Ba	La	Ce
A3.1 $\bar{x}$	87.82	17.02	6.41	348.98	24.34	102.15	14.18	1.01	0.04	174.74	10.35	23.07
σ	1.51	0.05	0.17	5.12	0.18	4.08	0.17	0.03	0.00	0.71	0.07	0.11
V	1.72	0.28	2.63	1.47	0.74	3.99	1.20	2.60	2.76	0.40	0.70	0.48

	Pr	Nd	Sm	Eu	Gd	Tb	Dy	Ho	Er	Tm	Yb	Lu
A3.1 $\bar{x}$	3.13	14.38	3.64	1.33	4.17	0.68	4.13	0.84	2.29	0.33	2.07	0.31
σ	0.01	0.05	0.01	0.02	0.09	0.00	0.03	0.01	0.01	0.00	0.01	0.00
V	0.29	0.34	0.33	1.21	2.08	0.66	0.63	0.99	0.35	0.00	0.54	0.28

	Hf	Ta	Tl	Pb	Th	U
A3.1 $\bar{x}$	2.64	0.91	0.01	1.01	0.88	0.25
σ	0.00	0.01	0.00	0.01	0.00	0.00
V	0.05	0.85	7.01	0.53	0.48	0.90